DEVELOPMENT AND ASSESSMENT OF ESTIMATE METHODS FOR INTERNAL DOSIMETRY USING PET/CT

Doctoral Dissertation

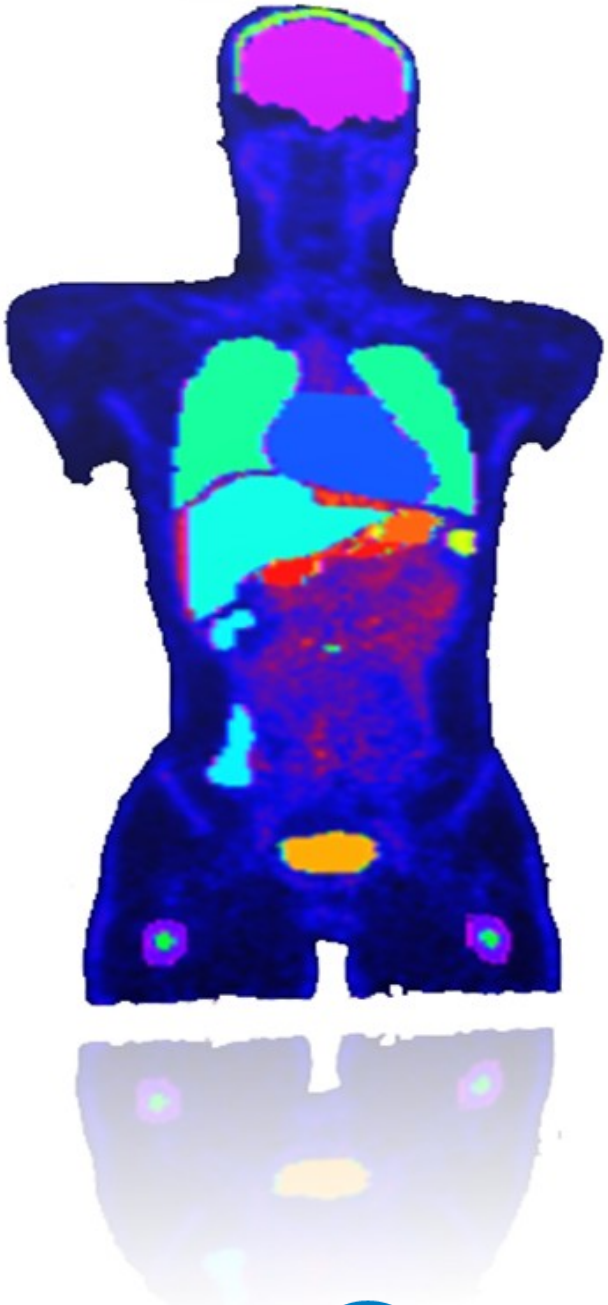

Natàlia López Vilanova

Supervisors:

Dr. Maria Amor Duch Guillén
Dr. Santiago Bullich Roig

December 2018

UNIVERSITAT POLITÈCNICA DE CATALUNYA
BARCELONATECH
Institut de Tècniques Energètiques

UNIVERSITAT POLITÈCNICA DE CATALUNYA BARCELONATECH

Development and assessment of estimate methods for internal dosimetry using PET/CT

Natàlia López Vilanova

UNIVERSITAT POLITÈCNICA DE CATALUNYA
BARCELONATECH
Institut de Tècniques Energètiques

Development and Assessment of Estimate Methods for Internal Dosimetry using PET/CT

Natàlia López Vilanova

Doctoral Dissertation

Supervised by

Dr. Maria Amor Duch Guillén
Dr. Santiago Bullich Roig

December 2018

Als meus pares, pel seu suport i afecte incondicional.

Al Jordi, l'Adrià i al Marcel per ser-hi, per completar-me, per fer camí junts.

Acknowledgements

En el moment d'iniciar aquest viatge no era del tot conscient del que suposaria dur a terme un repte com aquest. Certament he d'admetre que hi ha hagut moments de dubtes i adversitats. Però veient tot el que he pogut aprendre i viure en aquest període de temps, tinc clar que tornaria a recórrer aquest camí. Haver arribat fins aquí no hauria estat possible sense el suport i l'afecte de tota aquella gent que m'envolta o m'ha envoltat aquests darrers anys. En aquests moments sento una profunda i sincera gratitud envers tots ells i no puc deixar escapar l'ocasió de dedicar-los, de tot cor, unes paraules.

El meu primer i més càlid agraïment és pels meus directors de tesi, la Dra. Maria Amor Duch i el Dr. Santiago Bullich. Per la seva orientació i guia en aquest llarg camí, pel seu suport incondicional i per demanar i treure el millor de mi. La seva amistat, temps, paciència, dedicació i confiança dipositada han fet possible la realització d'aquesta tesi. L' immens coneixement, experiència, humilitat i treball transmès han esdevingut en una gran admiració personal. No hauria pogut tenir millors mestres a qui seguir, no tan sols a nivell científic sinó, i sobretot, a nivell personal.

També m'agradaria agrair al Dr. Javier Pavía i al Dr. Domènec Ros el brindar-me l'oportunitat d'iniciar aquesta tesi a través d'un contracte d'investigació del Centro de Investigación Biomédica en Red en Bioingeniería, Biomateriales y Nanomedicina (CIBER-BBN). Gràcies per la vostra amable acollida, ajuda, formació i suport rebuts.

Gràcies als companys i amics de l' Institut de Tècniques Energètiques (INTE), pels bons moments compartits durant aquests anys, que no en són pocs, per fer que la meva estada fos molt agradable i enriquidora. Especialment gràcies a la Maria, la Sonia i l'Antonia, pels riures a l'hora de dinar, pels cafès, per ajudar a renovar forces dins i fora de l'Institut, a totes vosaltres gràcies per ser-hi.

A nivell personal la llista és molt llarga, però vull agrair tots els ànims i energia rebuda per les noies: la Carol, l'Elena, la Tatiana, la Carmen i l'Adela.

Els meus últims agraïments van dirigits als meus pares, d'allà on vinc, gràcies pel vostre esforç i pel suport i amor rebuts. Al Jordi, amb qui faig camí, gràcies per estar sempre al meu costat, per fer l'esforç amb mi i compartir la vida. Als meus fills, cap allà on vaig, l'Adrià i el Marcel dos tresors nascuts al llarg d'aquest viatge.

Abstract

The aim of this thesis was to assess and develop internal dose calculations methods in diagnostic and therapeutic nuclear medicine procedures to patients undergone PET/CT explorations. Towards this objective, the accuracy and precision of different classical methods commonly used to estimate internal dosimetry were investigated. Biodistribution studies were used in order to compare these methods. The main study aspects included region-of-interest (ROI) delineation methods, reconstruction algorithms, scatter correction and radiopharmaceutical's biokinetic. Optimization of internal dosimetry in this thesis was completed with the development of a Monte Carlo (MC) technique for estimating the patient-specific PET/CT dosimetry.

The development of a mathematical model using MC techniques allowed us to have a gold standard to which compare classical techniques and study the aspects discussed previously. It was observed that effective dose (ED) estimations were sensitive to whichever delineation ROI method was applied. Furthermore, it was perceived that the biokinetics of the radioligand also influences in the ED estimation. On the other hand, similar quantitative accuracy was found regarding image reconstruction (FBP and OSEM) and scatter correction methods studied (FSC and SSC). Analysis of the impact of inter- and intra-operator variability in dose estimations revealed higher reproducibility in 3D methods in comparison with 2D planar method. The last one, showed the highest inter-operator variability, which implies an overestimation of the ED.

In this dissertation, specific routines were developed to be applied with the MC code PENELOPE/penEasy to perform individualized internal dosimetry estimations. Voxel-level absorbed dose maps which include self- and cross-irradiation doses were generated from the morphological and functional patient images. Further parameters such as cumulative organ dose, maximum and minimum voxel organ values, volume of the organ and dose-volume histograms of interest were reported. The model implemented was applied to a theoretical study using simulated PET images of a voxelized Zubal phantom. The results were benchmarked with the ones obtained using the OLINDA/EXM software. The comparison was in good agreement for those organs were both phantoms considered (Zubal and the reference one in OLINDA/EXM) were close.

Undoubtedly, the implementation of a patient-specific internal dosimetry method not only leads to an improvement in diagnostic examinations where the risk could be

quantified, but also NM therapy could become more effective in terms that patients receiving an optimal care.

Contents

List of Figures

List of Tables

List of Abbreviations

Abbreviation	*Definition*
2D	Two-Dimensional
3D	Three-Dimensional
ANOVA	Analysis Of Variance
AP	Antero-Posterior
APDs	Avalanche Photodiodes
BGO	Bismuth Germanium Oxide
BMI	Body Mass Index
CT	Computed Tomography
DF	Dose Factor
ED	Effective Dose
FBP	Filtered Back Projection
FDG	Fludesoxiglucosa
FOV	Field Of View
FSC	Full Scattered Correction
FWHM	Full Width at Half Maximum
GSO	Gadolinium Oxyorthosilicate
HCT	Helical Computed Tomography
HU	Hounsfield Unit
ICRP	International Commission on Radiological Protection
ISC	Ideal Scatter Correction
keV	kiloelectronvolt
LOR	Line of Response
LSO	Lutetium Oxyorthosilicate
MC	Monte Carlo

MeV	Megaelectronvolt
min	minutes
MIRD	Medical Internal Radiation Dose
MLEM	Maximum Likelihood Expectation Maximization
MRI	Magnetic Resonance Imaging
mSv	miliSievert
NEA	Nuclear Energy Agency
NMI	Nuclear Medicine Imaging
OLINDA/EXM	Organ Level Internal Dose Assessment/ Exponential Modeling
OSEM	Ordered Subsets Expectation Maximization
PDF	Probability Density Function
PENELOPE	Penetration and Energy Loss of Positrons and Electrons
PET	Positron Emission Tomography
PET/CT	Positron Emission Tomography/Computed Tomography
PHG	Photon History Generator
PMTs	Photomultiplier Tubes
PVE	Partial Volume Effect
RADAR	Radiation Dose Assessment Resource
RAI	Radioactive Iodine
ROI	Region-of-interest
S	Subsample
SimSET	Simulation System for Emission Tomography
SiPMs	Silicon Photomultipliers
SPECT	Single Photon Emission Computed Tomography
SSC	Single Scattered Correction
STIR	Software for Tomographic Image Recosntruction
TACs	Time Activity Curves
TRT	Targeted Radionuclide Therapy
W	Whole Organ

Chapter 1

Introduction

1.1 Nuclear Medicine

Nuclear Medicine (NM) is a medical speciality that uses the particular ability of radio labelled molecules (called radiopharmaceuticals) to integrate themselves in the biological mechanism of a cell, tissue or organ in order to make diagnostic evaluations or to provide therapy in various major areas such as oncology, cardiology and neurology. Particularly, nuclear medicine imaging contributes significantly to diagnosis, treatment planning and the assessment of response to treatment in patients with cancer disease. Every year in Europe over 6 million patients benefit from a nuclear medicine procedure, 95% of which are diagnostic and 5% therapeutic [6]. The number of procedures has experienced an increase in the past decade when new technologies, such as computed tomography (CT) and positron emission tomography (PET) have become widespread. And it will continue increasing in the coming years, in particular with the growing number of installed PET/CT systems and the introduction of new molecules and radiopharmaceuticals for diagnostics and also therapy. In therapy treatments these agents would provide new treatment options for many cancers, particularly following unsuccessful treatments with conventional chemotherapeutics or relapse.

Diagnostic examinations such as medical x-ray (including CT) or nuclear imaging provide great benefits to patients; however they have led to significant increase of individual patient doses. Effective dose to patients from radiodiagnostic procedures in Europe is estimated to be 1.10 mSv (1.05 mSv from x-ray, 0.05 mSv from NM procedures) per caput with an uncertainty below 10% [1]. The value of the effective dose per caput in Spain is estimated to 1.15 mSv [7], for medical procedures of nuclear medicine is 0.07 mSv. It can be seen that the contribution of NM is much less than that due to

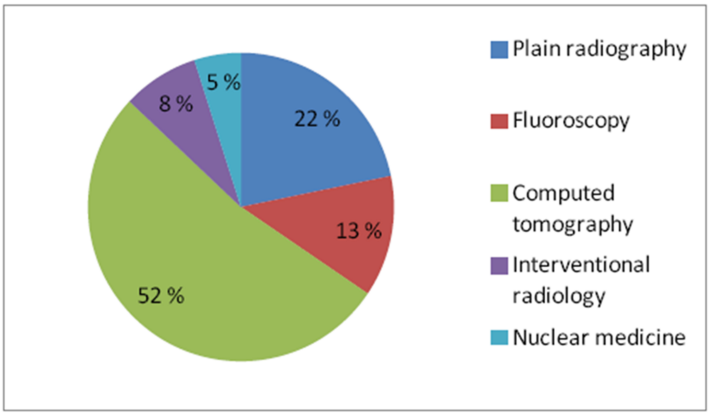

FIGURE 1.1: Relative contributions of the diagnostic procedures to the overall collective ED in Europe. From European Commission, Radiation Protection Nº180, 2014 [1].

diagnostic procedures. However, it is slightly higher than the collective effective dose of the rest of European countries.

The most common medical diagnostic procedures in Europe are CT, plain radiography, fluoroscopy, interventional radiology and NM procedures. Their contribution to the total population doses is respectively about 52%, 22%, 13%, 8% and 5% (figure 1.1). In those countries where PET is implanted, it is observed that oncological studies using PET are among the most significant, as is also the case in Spain. More than half European countries use PET/CT for oncological imaging; figure 1.2 shows annual frequencies of NM examinations per 1000 of population for tumor imaging with PET and PET/CT hybrid system.

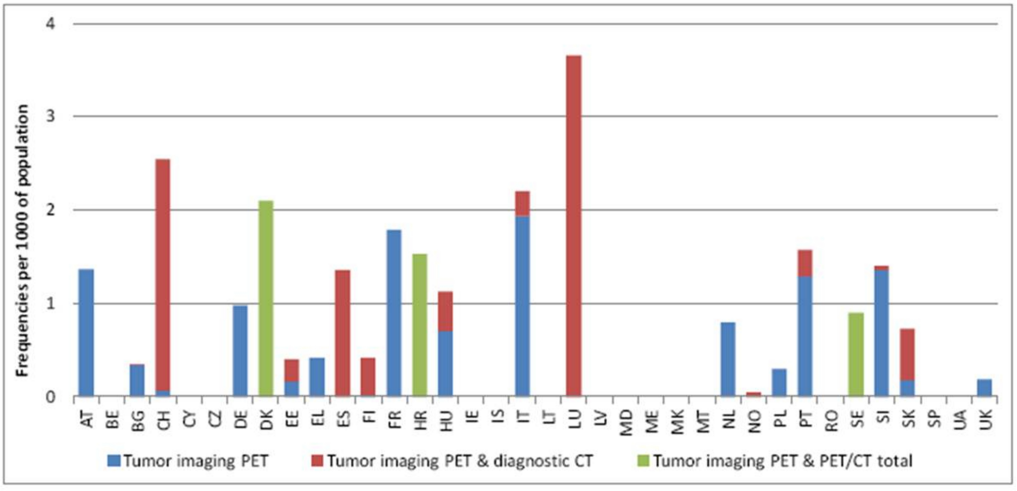

FIGURE 1.2: Annual frecuencies of NM examinations per 1000 of population, for tumor imaging with PET and PET associated with a diagnostic CT. From European Commission, Radiation Protection Nº180, 2014 [1].

.

Therapeutic nuclear medicine is developing rapidly as an alternative choice of treatment in oncology, with non-sealed sources of radioactivity. Replacing the gamma emitting isotope in a radiopharmaceutical by an alpha or beta emitter can transform a diagnostic tool into a very efficient and selective therapeutic tool. The administration of radionuclides is minimally invasive and the duration of treatment is shorter than chemotherapy, thus targeted radionuclide therapy has become one of the most preferred types of cancer therapy. The use of new radiopharmaceuticals requires individualized treatments involving the calculation of absorbed doses to the tumor and healthy tissues. It has been stated a correlation between the absorbed doses delivered and the response and toxicity, indicating the benefit of dosimetry-based personalized treatments [8, 9].

Theranostics is an emerging field of nuclear medicine which couples diagnostic imaging and therapy with the same molecule, but differently radiolabelled [10]. The detection of potential targets can help to predict if a patient would benefit from a particular treatment or not. The theranostics model involves also a personalized and precision methodology.

1.2 Molecular Imaging Techniques

As described above, Nuclear Medicine Imaging (NMI) is an approach for noninvasive detection of variety of human disease. The two basic components of these imaging procedures are: a) the use of specific radiopharmaceuticals and b) the use of a proper imaging system for the detection of the emitted photons.

The main two techniques in emission tomography are SPECT and PET scans, which use radioactive materials to image properties of the body's physiology. Thus, nuclear medicine procedures in general and PET procedures in particular are capable of providing information concerning how the body is functioning at a physiologic or biochemical level, whereas x-ray procedures such as computed tomography (CT) primarily depict human anatomy. Figure 1.3 shows a general overview of a PET imaging procedure.

In the context of this thesis PET molecular imaging technique is applied. The remainder of this chapter summarizes the fundamental principles that are needed to understand how nuclear medicine images are obtained and how diagnostic and therapeutic radiation doses are estimated for radiopharmaceuticals. This overview begins with a description of radiation transport of photons and particles produced by radioactive decay. Next, PET radioisotope production is outlined, as well as the description of the PET system and the image reconstruction techniques used to estimate the 3D distribution of

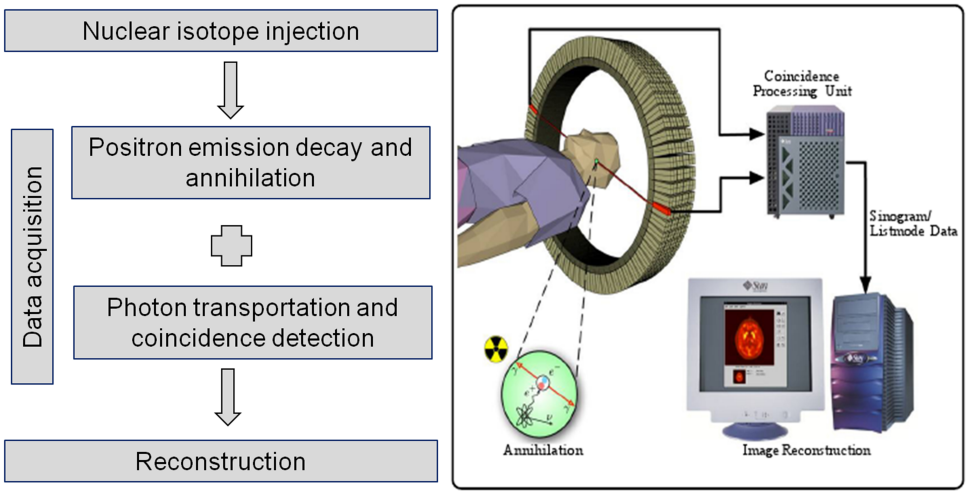

FIGURE 1.3: General overview of NMI procedure from the injection of radiopharmaceutical to the acquisition images.

radioactivity in a patient. Finally, the focus is on the steps to estimate absorbed doses to this patient.

1.3 PET Radiopharmaceuticals

Radiopharmaceuticals are drugs that contain radioactive substances called radioisotopes. Radioisotopes are nuclei that emit radiation as gamma rays or particles. In some cases, radiopharmaceuticals use radioisotopes that emit a combination of these types of radiation. The radioisotopes used in radiopharmaceuticals can be produced by irradiating a specific target inside of a nuclear research reactor or in particle accelerators, such as cyclotrons. Once produced, the radioisotopes are tagged on to certain molecules selected by its biological characteristics, which then results in radiopharmaceuticals.

One of the greatest advantages of PET imaging is the large number of low atomic number elements for which positron emitters exist (Table 1.1). This permits incorporation of positron emitters into many biologically active compounds, including isotopic forms of oxygen, carbon, nitrogen and fluorine.

The most common used diagnostic radiopharmaceutical is 2[18F]fluoro-2-deoxy-D-glucose, which is a glucose analog which enable the measurement of glucose consumption. ^{18}F-FDG is more widely used in oncology, so that the whole-body studies with ^{18}F-FDG have become the most frequently used mode in PET imaging. However, FDG is a nonspecific tracer and uptake of FDG is also noted in various benign conditions, such as different infective/inflammatory processes. So inquest for searching specific markers over the last decade a variety of new PET radiopharmaceuticals are entering the picture.

TABLE 1.1: Common Positron-Emitting Nuclides Update.

Nuclide	Half-Life (min)	Positron Yield (%)	Maximum Energy (MeV)	Method of Production
^{18}F	110.00	97.0	0.635	Cyclotron
^{11}C	20.4	99.0	0.960	Cyclotron
^{13}N	9.96	100.0	1.190	Cyclotron
^{15}O	2.04	99.9	1.720	Cyclotron
^{68}Ga	68.1	90.0	1.900	Generator
^{62}Cu	9.8	98.0	2.930	Generator
^{82}Rb	1.27	96.0	3.350	Generator

By using different tracers, molecular imaging using PET enables the visualization of various molecular pathways in tumour biology including metabolism, proliferation, oxygen delivery and protein synthesis as well as receptor and gene expression. PET with these radiopharmaceuticals can be used for tumour staging, for prediction of response to therapy, detection of early recurrence, and evaluation of modifications in organ function after treatment [11]. For instance, newer radiopharmaceuticals which improve radiation treatment planning are ^{11}C-methionine which is currently one of the best available PET tracers for delineating brain tumour contours [12]. For imaging prostate cancer ^{11}C- and ^{18}F- labelled choline derivatives are promising tracers [13].

Therapeutic radiopharmaceuticals for managing and treating diseases relies on how effectively the radiopharmaceutical can localize in the tissue or organ to be treated, which in turn depends on how the body interacts with the radiopharmaceutical. Once selected, radiopharmaceuticals are administered in large doses in order to deliver targeted doses of radiation to problematic areas within the body.

The most commonly used therapeutic radionuclide today is iodine-131 labelled with sodium iodide (^{131}I-NaI) in capsule or liquid form. The treatment is widely known as radioactive iodine (RAI) therapy, which uses ^{131}I to treat thyroid-related diseases [14]. Table 1.2 shows the commonly used radiopharmaceuticals for targeted radionuclide therapy (TRT).

At present, the most successful groups of isotopes for theranostics are $^{123}I/^{124}I/^{131}I$ [15], $^{68}Ga/^{177}Lu$ and $^{111}In/^{86}Y/^{90}Y$ [4, 16]. One of the classic examples of theranostics is the use of ^{68}Ga-labelled tracers, in which the diagnosis using ^{68}Ga can be effectively followed by therapy using therapeutic radionuclides such as ^{90}Y and ^{177}Lu labelled with the same tracer for personalized radionuclide therapy [8].

TABLE 1.2: Commonly used radiopharmaceuticals for targeted radionuclide therapy [4].

Radiopharmaceutical	Targeting mechanism	Indication
^{131}I-iodide	Thyroid hormone synthesis	Differentiated thyroid cancer, Graves' disease, hyperfunctioning nodules
^{90}Y-microspheres	Intravascular trapping	Liver metastasis, hepatocellular carcinoma
^{89}Sr-chloride	Calcium analogue	Bone pain palliation
^{153}Sm-EDTMP	Chemo-adsorption	Bone pain palliation
^{90}Y-octreotide	Somatostatin receptor binding	Neuroendocrine tumours
^{131}I-MIBG	Active transport into neuroendocrine cells and intracellular storage	Neuroblastoma, pheochromacytoma, carcinoid, paraganglioma, medullary thyroid carcinoma

1.4 Positron Emission Tomography

Positron emission tomography (PET) is a non-invasive functional imaging technology for quantitatively measuring physiological and biochemical processes in vivo. The amounts of radiolabelled material administered are extremely small and have essentially no pharmacologic effects. In this regard, PET has the unique ability to assess molecular alterations associated with disease without perturbing or altering the fundamental underlying molecular and biochemical processes [17, 18]. Radioactive compounds used in PET are labeled with short-lived positron-emitting radionuclides such as ^{18}F, ^{11}C, ^{13}N, ^{82}Rb and ^{15}O (see section 1.3). The labeled compound is introduced into the body, usually by intravenous injection and is distributed in tissues in a manner determined by its biochemical properties. This results in a 3D image volume of the concentration of the radioisotope. Then, the tissue concentration of the radiotracer over time can be measured enabling the application of pharmacokinetic models to measure the rate of a specific biological process without disturbing it.

1.4.1 Positron Decay and Annihilation

PET imaging relies on the nature of the positron and positron decay. The positron is the antimatter counterpart to the electron (it has the same mass and opposite charge than the particle). When a nucleus undergoes positron decay [19], the result is a new nuclide with one less proton and one more neutron, as well as the emission of a positron and a neutrino. This process is called positive beta-plus decay or β^+ and is summarized in the equation:

$$ {}^{A}_{Z}X_N \longrightarrow {}^{A}_{Z-1}Y_{N+1} + e^+ + \nu \tag{1.1} $$

When a radiotracer is injected to a patient, positron emitted by the radioisotope travel through human tissue, they give up their kinetic energy mainly by Coulomb interactions with atomic. Thus, when the positrons reach very low energies they interact with electrons by a positron-electron annihilation. The result of the annihilation must be two 511 keV photons travelling in opposite directions.

1.4.2 Positron Range and Non-Colinearity

In PET imaging there are two effects that may lead to errors in determining the line along the annihilation took place (figure 1.4). These effects place some finite limits on the spatial resolution in PET and manifest themselves as a blurring of the reconstructed images. In the first effect, positrons undergo multiple direction-changing interactions prior to annihilation, following a path in the tissue. This total path length is considerably longer than the *positron range* which is defined as the distance between the emission and the annihilation point. From PET imaging perspective it is the average distance from the emitting nucleus to the end of the positron range, measured perpendicular to a line defined by the direction of the annihilation photons. Some radionuclides emit, on average, higher energy positrons than others, making the positron range effect radionuclide-dependent [20].

In addition to the positron range, the variation in the momentum of the positron also leads to a limitation of the spatial resolution of PET imaging. Due to the fact that the positrons can be annihilated when they still have a small part of the kinetic energy (initial linear momentum is not equal to zero), a slight deviation from collinearity can occur (the gamma rays are not exactly at 180 degrees) so that the linear momentum is conserved. This effect is called *non-collinearity* and it can reach maximum deviations of 0.25 degrees [21]. The distribution of emitted angles is roughly Gaussian in shape, with a Full Width at Half Maximum (FWHM) of 0.5 degrees [22].

1.5 Imaging Technology for PET

1.5.1 Detection System

The opposing detectors of a PET system (figure 1.5) register the arrival of the annihilation photons as an event if they are detected within a narrow time frame, called *timing window of the coincidence circuit* (typically 3 to 15 ns); all other signals are disregarded as noise. This requirement of detecting both photons within a time window is the basis of coincidence detection . It is assumed that the originating decay event must have taken

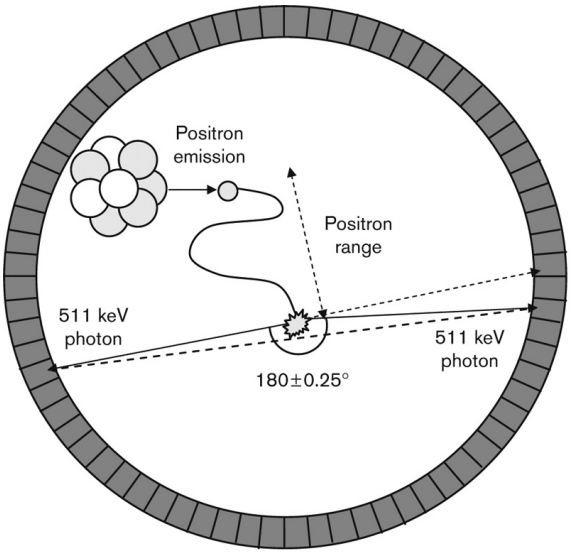

FIGURE 1.4: Positron range and non-colinearity. From A. Rahmim, 2008 [2].

place somewhere along the line segment connecting the two participating detectors, this line is referred to as the *line-of-response* or else *LOR*.

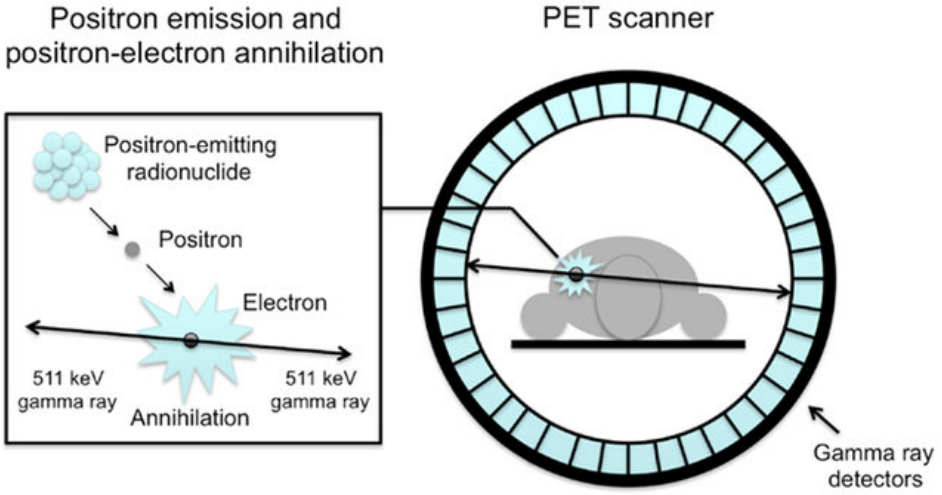

FIGURE 1.5: Schematic illustration of an annihilation reaction and the subsequent coincidence detection. Positrons released from the nucleus of the radionuclide annihilate with electrons in tissue, releasing two coincidence photons of 511 keV, which are detected by scintillation crystals (blue rectangles). Coincidence detection of annihilated photons identifies a line-of-response and makes it possible to localize the source of the annihilation. From Van der Veldt et.al, 2013 [3].

After the annihilation and emission processes, the photons can be detected by means of a scintillator material. The interactions of the photons within the scintillator material are used to compute the spatial location and total energy deposited. This energy deposited by the 511 keV photons is converted into visible light by a light sensors such as photomultiplier tubes (PMTs) or solid state detectors like avalanche photodiodes (APDs) or silicon photomultipliers (SiPMs). As was mentioned above, photons are

emitted simultaneously and in opposite directions and, therefore, if photons pairs are detected in coincidence, physical collimation can be removed. Short timing window must be employed ($\sim 10\ ns$) in order to detect photons from the same annihilation.

Scintillation detectors are the most common and successful mode for detection of photons in PET imaging. They emit light when they are excited by radiation of higher energy. The intensity of the scintillation light is important for an accurate determination of the energy of the absorbed radiation. The scintillation crystals used in clinical PET imaging are either bismuth germanium oxide (BGO), gadolinium oxyorthosilicate (GSO) or lutetium oxyorthosilicate (LSO). It is also very important to have an accurate assessment of exactly when a photon interacts in a detector. The accuracy of timing is determined by the decay time and its brightness [20, 23].

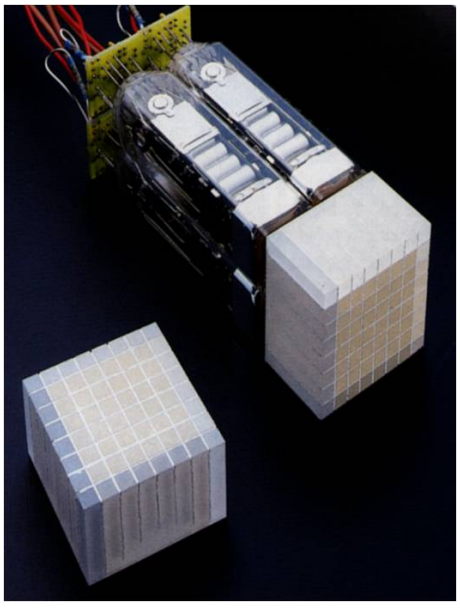

FIGURE 1.6: Block detector consisting of four PMTs coupled to an array of 8×8 crystal segments.

In general, a PET scanner consists of a bed and a gantry supporting the tomography detectors. The gantry defines a tunnel through which the patient travels after being injected with a radiopharmaceutical (figure 4.1). The common PET detector consists of rings of block detectors. Each block detector is organized into 2D arrays and contains one or more segmented crystals or a collection of small crystals. Figure 1.6 shows a photograph of a typical block detector, consisting of four PMTs coupled to one common scintillator block.

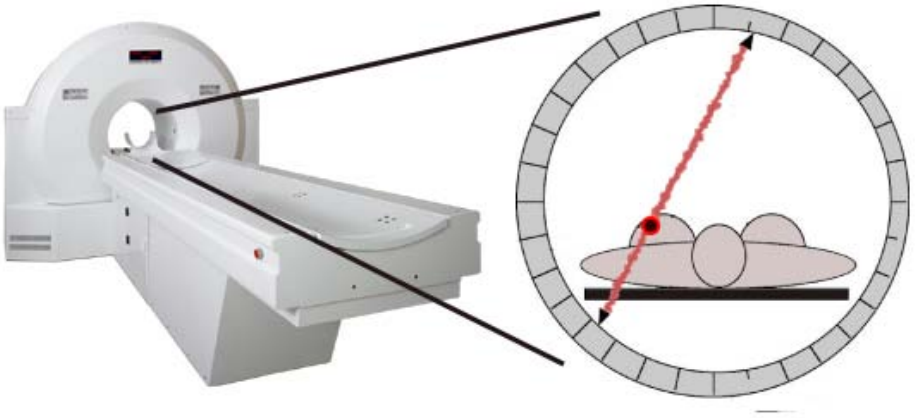

FIGURE 1.7: Positron emission camera and detection process.

1.5.2 Data Organization

Each coincidence event is assigned to a LOR and it is determined by the projection angle, the distance along the detector array in the transaxial plane and two spatial coordinates in the axial direction. These information is stored as a set of two-dimensional images called *sinograms* (figure 1.8).

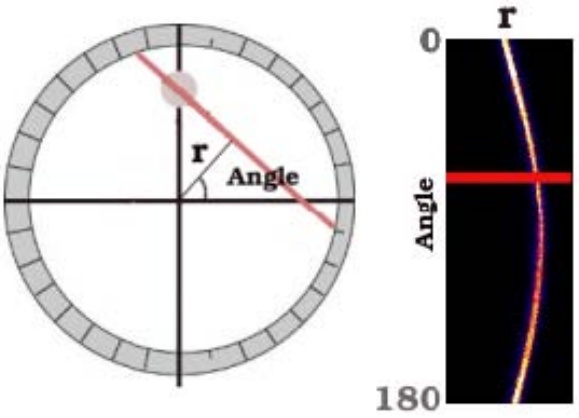

FIGURE 1.8: Line of response (LOR) and sinograms.

1.6 Data Acquisition

1.6.1 Types of Events

In the majority of total events detected by the PET system, only one of the two annihilation photons is registered. The other photon may be not on a trajectory that would intersect a detector, or may not deposit enough energy in the detectors to be registered. Normally these *single events* are rejected by the system.

Each detected photons is defined by its detection time and deposited energy in the detectors. Both informations are used to specify the LOR and therefore the pair of detectors in which the annihilation event was detected within a certain time coincidence windows. If the two photons are emitted at an exact angle of 180^{o} then the annihilation must have taken place in the volume covered by the two detectors which is usually addressed as LOR. Whereas, the detection of the two annihilating photon are called *coincidence events*. In a real experiment not all coincidences are emitted at an angle of 180^{o} and several other scenarios as indicated in figure 1.9 are possible [19, 22]:

- *True coincidences*: Two photons are emitted in an angle of 180^{o}. On their flight trajectory they are not scattered by the media they travel trough. For those events the correct LOR can be addressed.
- *Scattered coincidences*: True coincidences, but leading to the wrong LOR due to non-linearity or due to scattering. Two photons are generated but one is scattered into a different direction.
- *Random coincidences*: Two photons originate from different annihilations events but are detected by one detector pair.
- *Multiple coincidences* are similar to random events, except that more than two events from more than two annihilations are detected within the coincidence timing window. The event is disregarded due to the ambiguity in deciding which pair of events arises from the same annihilation.

Prompt events are the sum of true, scatter and random coincidences and only the true coincidences carry spatial information about the distribution of the radiotracer. Moreover, scatter and random events are undesirable because they contribute to an increase in image background counts and consequently cause a reduction in image contrast.

1.6.2 2D and 3D acquisitions

In most of the first generation multiring PET systems, axial collimators or septa were placed in between adjacent rings of detectors. *Septa rings* can be used to improve resolution by reducing the amount of scatter from photons originating outside the plane of one ring of crystals. The sensitivity of the scanner is reduced, because a significant fraction of true coincidence events are rejected [24].

Newer PET systems remove septa in between adjacent rings, and the data is collected from all possible LORs. Because the coincidence planes are not only transaxial planes, this acquisition mode is referred as three-dimensional acquisition.

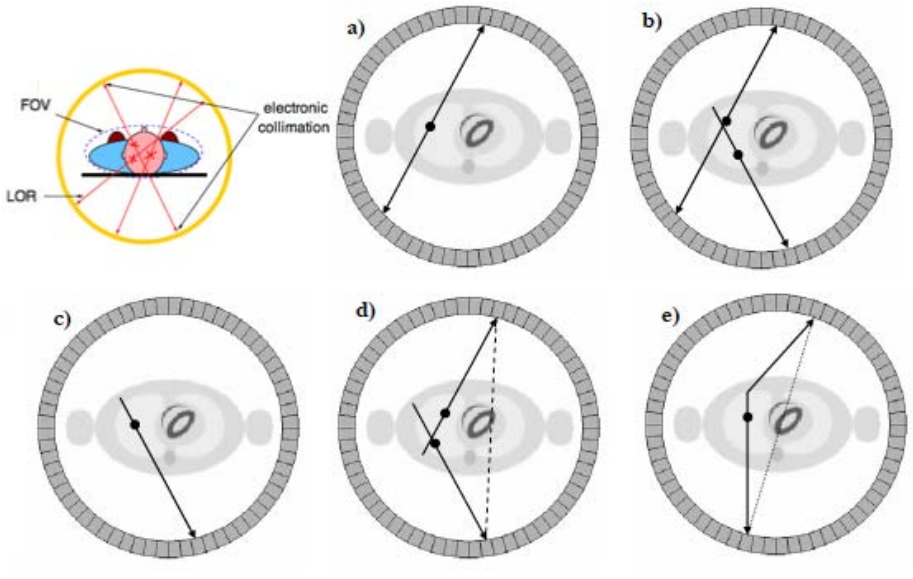

FIGURE 1.9: Illustration of the main coincidence event types: a) true; b) multiple; c) single; d) random and e) scattered.

So, scans obtained with the septa in place are called *2D scans*; without septa the scans are called *3D scans*. In the 2D scans the septa block out-of-plane photons, allowing only within-plane coincidence events to be recorded. The 3D configuration permits coincident registration of cross-plane events, those in which the two 511 keV photons are detected in different rings. Septa reduce the number of random coincidence events.

1.6.3 Image Degradations

Both the interaction of radiation with matter and other effects associated with PET instrumentation can become important degradation factors of the image. In section 1.4.2 have been described the main factors which affect resolution in PET imaging: positron range in tissue and photon emissions occurring at other than 180^{o}. In this section are discussed the factors which affect the reconstruction and post-reconstruction processing.

1.6.3.1 Normalization

In PET scanners there are variations in the response of each crystal detector, resulting in a variation of the detection sensitivity that leads to non-uniform count rates. The process to correct these effects is called normalization [25].

The most straightforward method of determining the normalization coefficients (NCs) in order to compensate the non-uniformities of the detectors is to perform a scan of an

uniform activity plane source, positioned at a number of equally spaced projection angles. This process will directly give a complete set of relative variation in coincidence detection efficiencies between all the LORs in the system. However, this process it takes quite large amount of time to acquire sufficient counts per LOR for good statistical estimation (tens of hours).

The time consuming problem can be solved by using a component-based variance reduction method [25], in which the coincidence detection efficiency between a pair of detectors of interest is assumed to be the product of the detector efficiencies and geometric factor.

1.6.3.2 Attenuation Effect

Attenuation correction is one of the most important corrections in PET data as it produces a change in the quantitative values. One or both annihilation photons could have undergone Compton scatter interaction before escaping from the object material, and this results in the removal or attenuation of primary photons of the LOR and the potential detection of scattered photons in different LORs.

Consider a point source located at depth x inside an object material of thickness L along the LOR with linear attenuation coefficient μ, the probability of both [26]:

$$p = e^{-\mu x} \cdot e^{-\mu(L-x)} = e^{-\mu L} \tag{1.2}$$

The probability is independent of the location of point source and only depends on the object thickness along the LOR. According to equation 1.2, the attenuation factor for a given LOR depends on the total distance travelled by both annihilation photons. So, the attenuation effect only requires a simple premultiplication of the emission sinograms by the attenuation correction factors. These factors are applied using an attenuation map, which can be derived through an external transmission source or a CT image integrated into the PET scanner.

First, the reference blank scan is measured with no object in the scanner, in which the blank data will be collected. Just before the injection of radioactive tracer, a transmission scan is acquired for the measured activity with the object inside the scanner. The attenuation factors along each LOR [27] are given by taking the ratio between the transmission scan and blank scan.

1.6.3.3 Scatter Coincidences

As discussed in section 1.6.1, the Compton scatter interaction is responsible not only for the attenuation effect but also for the scattered photons. This fraction of scatter coincidences leads to many mispositioned events which can cause significant loss of contrast in the reconstructed images and bias in activity quantification. Although in 2D PET the scatter fraction is less than 10% and it seems that could be ignored, in 3D PET the fraction of scatter in the signal can become extremely large [28, 29].

1.6.3.4 Random Coincidences

Random coincidence creates an approximately uniform background across the field-of-view (FOV) of system, reduces the image contrast and can cause significant artefacts; thus it is necessary to remove random coincidence from the prompt coincidence to obtain quantitative PET image data.

The average random coincidences rate can be calculated for each LOR as:

$$R_{ij} = 2tr_i r_j \tag{1.3}$$

where R_{ij} is the random coincidence rate on the LOR defined between the detector crystals i and j, r_i is the singles rate on the detector crystal i, r_j is the singles rate on the detector crystal j and t the width of the timing window. Thus, the random coincidences rate can be measured and substracted from the emission sinograms. Other method for estimating the randoms coincidence rate is the delayed window method. The counts that are in the standard time window include randoms and trues, whereas the delayed time window includes only randoms [20].

1.6.3.5 Dead-Time

The detector crystals have a time after each photon detected during which the system is not able to detect another new photon. This time is called dead-time of the detector and it is due to the time required to process individual events. The dead-time depend on the decay time of light in the crystal as well as entire read-out circuitry. It is considered to be the dominant effect which limits the injection dose [22].

1.6.3.6 Partial Volume Effect (PVE)

Partial volume effects (PVE) are a consequence of the limited spatial resolution of PET scanners (about 5-6 mm FWHM). "Hot" spots (structures) relative to a "cold" background that are smaller than twice the resolution of the scanner show partial loss of intensity and the activity around the structure appears to be smeared over a larger area than it occupies in the reconstructed image. While the total counts are preserved, the object appears to be larger and to have a lower activity concentration than it actually has. Similarly, a cold spot relative to a hot background would appear smaller with high activity concentration. Such underestimation and overestimation of activities around smaller structures in the reconstructed images is called the partial volume effect. Several techniques have been reported in the literature for PVE compensation in emission tomography [30, 31].

1.6.4 Image Reconstruction

The purpose of tomographic image reconstruction is to provide a cross-sectional image of the distribution of radiotracer activity from the acquired data by the scanner. The collection of projection p profiles forms the sinogram, which is used to reconstruct the image through different methods for tomographic reconstruction that can be divided into analytic and iterative approaches. Analytic reconstruction methods offer a fast and direct mathematical solution for the image with no attempt to model the statistical nature of the gamma-ray counting process. Statistical, iterative methods are based on a more accurate description of the imaging process resulting in a more complicated mathematical solution requiring multiple steps to get the final image.

1.6.4.1 Analytical Reconstruction

Analytical methods where the first used. By reducing the problem to two dimensions, a three-dimensional distribution of the drug administered can be obtained.

Analytical methods are based on the backprojection of projection profiles, which is the principle employed to reconstruct the images from acquired LORs. When a reconstruction matrix of a chosen size is selected, the counts along a LOR are projected back along the line from which they originated. This is repeated for all LORs until a reconstructed image from all backprojected data is formed.

The backprojection gives a blurred image of the actual object. This effect can be minimized by applying a filter (*ramp filter*) to the acquisition data. The meaning of the

ramp filter is to recovery high frequencies which have been attenuated in the backprojection process.

2D Filtered back-projection

It is the most common analytical algorithm used. FBP algorithm can be implemented with the following steps:

1. To take the 1D Fourier transform of the projections (sinograms).
2. To filter the obtained projections with the ramp filter.
3. To take the inverse Fourier transform of the filtered projections.
4. To backproject the obtained projections.

The problem with this method is that the filter that powers the high frequencies also amplifies the noise and therefore the reconstructed image is usually very noisy.

Other filters can be employed in order to eliminate or attenuate frequencies above a predetermined cut-off frequency. These filters provide less noisy images, but the problem is that when the high frequencies are eliminated then the spatial resolution decreases.

3D Filtered back-projection

It is not obvious the 3D reconstruction methods due to truncated projections. These truncated projections arise from the fact that more coincidences are detected in the centre than at the axial end of the scanner. Thus, only those projections perpendicular to the detector will be complete projections, whereas all oblique projections could be truncated depending on the axial size of the object. A 3D-FBP was developed [32] for no truncated projections. The essential difference with respect to 2D lies in apply 2D Fourier transform instead of 1D and the form of the filter, in this case is used the Colsher filter [32] .

1.6.4.2 Iterative Reconstruction

Iterative reconstruction models are based on an initial estimation of the image and the projections which are computed from the image and compared with the measured projections. Differences between estimated and measured projections are used to improve the estimation and the process is iterated, until a good agreement between the two sets

of projections is reached. One advantage of these methods is that corrections of the physical aspects of the imaging system can be incorporated in the process of reconstruction.

The principal trade-off between iterative techniques and FBP is accuracy versus efficiency. All iterative methods require a certain number of repeated calculations of projection and backprojection operations. Thus, they need a substantially longer computation time than FBP. Advances in computation speed and faster algorithms have helped to overcome the computational burden of iterative methods allowing them to receive growing clinical acceptance.

MLEM and OSEM

The most widely used iterative algorithms used in PET are the maximum likelihood expectation maximization (MLEM) algorithm [33] and the ordered subset expectation maximization (OSEM) algorithm [34]. The MLEM algorithm uses many iterations to achieve an acceptable agreement between estimated and measured projections and a long computational time. The OSEM is a modification of the MLEM where projections are grouped into subsets around the object to be imaged separated by a fixed angle.

1.7 PET/CT Scanner

PET/CT scanner combine technology from two imaging modalities: positron emission tomography (PET) and computed tomography (CT). This combination makes it possible to fuse anatomic information from the CT scan with molecular imaging information provided by PET imaging. With this technology, not only can abnormal cell function be detected, it can be anatomically mapped with great precision [35].

PET/CT scanner consists of three main components (figure 1.10): (1) a CT gantry (2) a PET gantry, and (3) a patient bed. In a typical PET/CT protocol, patients first receive a CT scan and then a PET scan while the patient bed moves axially into the scanner. The operator initiates a whole-body scout CT scan (2–10 s) to determine a scan region. Then a whole-body helical CT (HCT) scan (30 s–2 min) is conducted. The last step is the PET scan (5–45 min). The patient stays still on the bed throughout these 3 acquisitions. All patient data can be acquired in 3D mode and are corrected for attenuation based on the CT transmission, random, scatter, and dead time effects. The final reconstructed images will be obtained by different algorithms such as 3D ordered-subset expectation maximization (OSEM). Multiple studies have demonstrated unequivocally the role of PET/CT, especially for oncologic applications [36, 37].

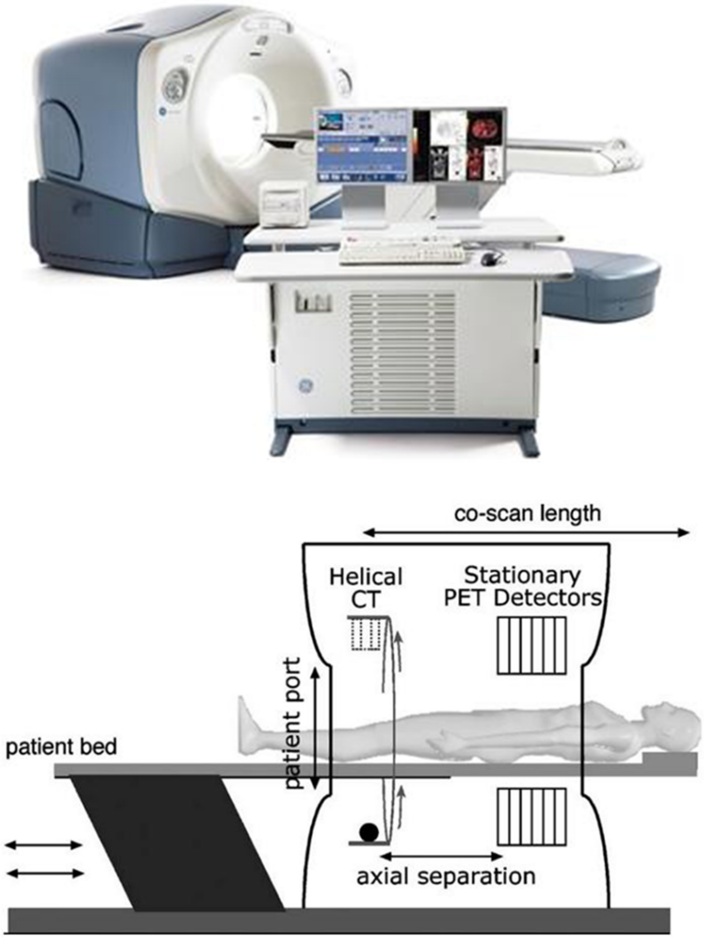

FIGURE 1.10: Standard PET/CT scanner and its diagram.

1.8 Internal Dosimetry

1.8.1 Components of the Calculation

The radiation absorbed dose is defined as the amount of energy deposited per unit mass. To estimate the dose, one must first specify the mass of the target tissue ($M(r_T)$), the cumulated activity in that object, as well as the activity in the surrounding regions. The yield of radiation Y and energy E of each radiation type i emitted per nuclear decay of the administered radionuclide must also be known. Furthermore, a quantity referred to as the absorbed fraction ϕ is needed, which represents the fraction of energy emitted from the source organ r_S that is deposited in the target organ r_T. These factors can be combined to form a generic equation for calculating the absorbed dose in r_T due to activity in r_S :

$$D(r_T, T_D) = \tilde{A}(r_S, T_D) \sum_i \frac{Y_i E_i \phi_i(r_T \leftarrow r_S, E_i)}{M(r_T)} \tag{1.4}$$

where $\tilde{A}(r_S, T_D)$ is the time-integrated activity (total number of nuclear transformations) in source tissue r_S over dose-integration period T_D.

Equation 1.4 is generic, different authors and groups have developed systems to calculate internal dose in different situations. There are three main systems: the ICRP (International Commission on Radiological Protection [1]), the MIRD (Medical Internal Radiation Dose [2]) and the RADAR (Radiation Dose Assessment Resource [3]) system. Most of the results in the ICRP system are oriented towards protection of radiation workers, whereas those of the MIRD system are oriented towards nuclear medicine patients. The RADAR system is designed to accommodate both and has been implemented in automated electronic methods that have been tested and used by the international nuclear medicine community for many years. Below are detailed the systems focused on the nuclear medicine patients:

MIRD System

The dose to the target summed over all source regions is given by [38, 39]:

$$D(r_T, T_D) = \sum_{r_S} \tilde{A}(r_S, T_D) S(r_T \leftarrow r_S) \tag{1.5}$$

where the S value $S(r_T \leftarrow r_S)$ represents the mean absorbed dose deposited in the target per unit of time-integrated activity that is present in the source.

RADAR System

The RADAR system [40] has about the simplest manifestation of the dose equation:

$$D = N \cdot DF \tag{1.6}$$

where N is the number of disintegrations that occur in a source organ and DF is mathematically the same as an S *value* as defined in the MIRD system. The number of disintegrations is the integral of a time-activity curve for a source region, like time-integrated activity $\tilde{A}(r_S, T_D)$. RADAR members produced compendia of decay data, dose conversion factors and catalogued standardized dose models for radiation workers and nuclear medicine patients, among other resources. They also produced the widely used OLINDA/EXM personal computer software code [41], which used these equations and the input data from the RADAR site.

[1] www.icrp.org
[2] www.nndc.bnl.gov/mird/
[3] www.doseinfo-radar.com/

It is considered that equation 1.5 illustrates the two major parts of internal dose calculations, which are (1) a 'biological' component, involving $\tilde{A}(r_S, T_D)$, and (2) a 'physical' part, involving all of the other terms given by $S(r_T \leftarrow r_S)$. The time-integrated activity $\tilde{A}(r_S, T_D)$ is often normalized by the administered activity to form the time-integrated activity coefficient $\tilde{a}(r_S, T_D)$ so that the estimated dose is reported in units of gray per megabecquerel ($Gy \cdot MBq^{-1}$).

1.8.2 Acquiring the Time-Integrated Activity

A biodistribution study is needed in order to determine the $\tilde{A}(r_S, T_D)$, the first part of the equation 1.5 which involve the biological distribution of the radioligand and retention of activity in the body. Data are obtained in animals (preclinical studies) or in human volunteers or patients (clinical studies). A series of nuclear medicine scans must first be acquired. Then, the reconstructed SPECT or PET images are segmented to obtain volume and activity estimates of source ROIs inside the patient. Finally, the acquired time-activity data can be plotted to form time-activity curves (TACs) for each source region, which are integrated to find the corresponding values of $\tilde{A}(r_S, T_D)$.

Animal data need to be extrapolated for use in calculating dose estimates for humans [42]. For either human or animal data, gathering the correct number of data points at appropriate time intervals is essential to a successful analysis [43].

In this section, each of these steps is described in detail.

Image Quantification

The first step in estimating time-integrated activities is to acquire a series of nuclear medicine images. This allows for the identification of source regions and the determination of activity in ROIs at different points in time. So, a dynamic study is needed. To increase the accuracy of time-integrated activity estimates for different areas in the body, hybrid devices such as SPECT/CT or PET/CT systems have been proposed instead of planar imaging [44]. This fact reduce uncertainties in absorbed dose calculations.

Region of Interest (ROI) Delineation

Once the imaging system is calibrated, ROIs need to be drawn to quantify the activity in larger objects. Despite efforts in recent years to provide reproducible operator-independent ROI drawing methods [44, 45], a gold standard has yet to be established.

Many centers today still rely on operator-dependent manual ROI drawing for image quantification.

In clinical and research studies, volumes of interest are commonly segmented using manual region delineation. Since drawing region boundaries on low resolution nuclear medicine images can be difficult, high resolution images obtained from an anatomical modality, such as CT or magnetic resonance imaging (MRI) may be used for this purpose. When planar images are acquired, ROIs must be delineated in 2D. If a hybrid SPECT/CT or PET/CT system is being used for organ level dose calculation, ROIs must be segmented in 3D to determine the total activity in these regions and the volume of these regions.

The different ROI delineation methods applied nowadays in clinical and dosimetry studies are detailed in section 4.4.1.

Time-Activity Curve (TAC)

The next step towards estimating the time-integrated activity in source regions is to plot the activity versus time for each region and fit a curve through this data. The area under this curve represents the total number of decays in the source (the time-integrated activity).

One way to find the area under the time-activity data is the trapezoidal method. This method involves adding up the areas of trapezoids formed by each pair of data points. In section 6.2.3 the method is detailed.

1.8.3 Dose Estimation Method

Once the 'biological' component in internal dose calculation is determined, the second step is to combine this data with the 'physical' data to find the corresponding dose distribution. This part is characterized by *Dose Factors* (RADAR system) for specified source and target regions for a particular radionuclide [40]. These DF are typically integrated in software programs to facilitate dose calculations, such as Organ Level Internal Dose Assessment with Exponential Modeling (OLINDA/EXM) [41] or MIRDOSE [46] software codes.

Using OLINDA/EXM (see section 3.4), the user inputs organ time-integrated activity and the program calculates the resulting absorbed dose for each organ. These doses are estimated based on organ level S values calculated for standard phantoms representing the average male or female.

The values for the *absorbed fractions* come from modeling assumptions or Monte Carlo calculations in antropomorphic phantoms (mathematical models of the human body). These phantoms were based on geometrical constructs to represent the body and its organs but more recently have been replaced with more realistic models based on medical image data [47, 48].

1.9 MC Simulations

1.9.1 Principles of MC Techniques

MC techniques are the most widely used kind of simulation methods for simulating nuclear medical imaging systems. MC simulations are a valuable tool to describe the transport of ionising radiation in these systems. The propagation of radiation, including absorption and scattering processes are determined by the Boltzmann transport equation [49]. This integro-differential equation can be analytically solved only in few cases consisting on oversimplified situations that would strongly differ from real clinical situations. MC simulations are stochastic solutions to the Boltzmann equation, so this numerical technique can reproduce the transport process in complex situations.

The general idea of Monte Carlo analysis is to create a model, which is as similar as possible to the real physical system of interest. Radiation transport is simulated by the creation of charged particles or photons from a defined source region(s), generally with a random initial orientation in space, with tracking of the particles as they travel through the system, sampling the *probability density functions* (PDFs) for their interactions to evaluate their trajectories and energy deposition at different points in the system. The interactions determine the penetration and motion of particles. The energy deposited during each interaction gives the radiation absorbed dose, when divided by the appropriate values of mass [50]. The key of the Monte Carlo method is, thus, the use of PDFs and random number generators (RNGs).

MC simulations employ random number generator to sample the interactions experienced by a particle in chronological succession. Theses interactions are stored in particle histories and accumulated or tallied in an appropriate manner to produce the desired result. The accuracy of the method is dependent on the number of histories simulated. A larger number of histories improve the accuracy of the simulation, which means that the statistical uncertainty decreases. However, increasing the number of events implies a large computational time and large data storage capacity.

1.9.2 MC Codes

MC codes can be divided into two broad categories [51]: (i) general purposes MC codes developed for general medical physics applications and (ii) dedicated software packages developed mainly for nuclear medicine imaging applications. General purpose codes such as EGS4, Geant4, MCNP, FLUKA or PENELOPE can be used in a variety of nuclear physics applications. Their main advantages are wide use and validation, as well as continuous support and update. The code systems vary in aspects such as, the type of the particle, the physics theories and cross-sections and the sampling techniques for using them, their ease of use and the speed with which simulations run.

The dedicated simulation codes are PET-EGS based on the EGS4 code [52], SimSPECT [53] derived from MCNP transport code, PETSIM [54], SimSET [55], EIDOLON [56], GATE [57] and GAMOS [58] based on Geant4, PeneloPET [59] based on PENELOPE, SORTEO [60] and SIMIND [61]. The main advantage of those packages is the relatively simple geometry construction, the fast implementation of simulation code and usually the performance advantages since they are optimized on specific applications. However there are disadvantages such as limits in the physics description and in the flexibility for simulating non-conventional imaging device.

Chapter 2

Aim and Outline

Estimation of radiation doses is an important component in the overall safety evaluation of the use of any radiopharmaceutical. Internal dosimetry estimates are intended to predict the risks of radiation in diagnosis and also the effectiveness and treatment outcome in therapeutic nuclear medicine. In spite of considerable progress on imaging devices and detection of the radiation, further efforts are needed in the future for optimizing diagnostic and therapeutic nuclear medicine procedures with respect to safety and efficacy for patient benefit.

Diagnostic nuclear medicine examinations are associated with low radiation doses and thus stochastic risks of cancer induction are outweighed by the diagnostic benefit of the image procedure. Nevertheless, the increasing radiation exposure from medical diagnostic procedures implies that tissues doses and their stochastic risks become an issue of concern by the medical physics community. Thus, in the European area, Directive 2013/59/EURATOM [62] on the protection of health against risks arising from ionizing radiation in medical exposures requires member states to obtain estimates of population doses from the individual doses for each medical exposure. It is considered that dosimetry should be quantified for each patient taking into account both, the cumulative values received over multiple imaging sessions and doses received by other diagnostic procedures that they may undergo. Once this risk is quantified, it may be used to optimize the amount of administered activity in order to maximize image quality while minimizing patient risk.

In therapeutic nuclear medicine, is essential to determine the individual kinetics of the radiopharmaceutical to be able to calculate the absorbed doses to critical organs or tissues and to the target volume with high accuracy. Despite the prospect for highly individualized therapy, dosimetry is not routinely employed as a clinical tool to optimize patient treatment. In current clinical practice, treatment is delivered based upon an

administered activity prescription. This prescribed activity is typically established in a primarily clinical trial (Phase I) from the toxicity response of only few patients, and is then applied to all subsequent patients. The dose to the tumour is neither quantified nor prescribed. The conservative "fixed activity" approach to treatment results in only a small percentage of patients receiving optimal care and, in the majority of cases, it lead to patient under-treatment. Due to patient variability of both agent pharmacokinetics and body morphometry, patient-specific dosimetry is an essential element to optimizing nuclear medicine therapy.

On the other hand, the rise in computing power over the last decades has allowed simulating physical processes more accurately. The integration MC simulations in the field of Nuclear Medicine are very helpful in the development and validation of dosimetry studies. They can provide realistic ground truth data for testing and optimization procedures or can be used directly to provide individual measurements.

According to what is mentioned above, the **goal** of the research described **in this thesis** is:

To contribute to analyze and optimize internal dose calculations in diagnostic and therapeutic nuclear medicine procedures with respect to patients who have undergone PET/CT scans. For these purposes, the following objectives are defined in this thesis:

- To develop a mathematical model in order to study the biodistribution of a radiopharmaceutical and the dosimetry in the source and target organs using MC techniques.
- To analyze and compare different classical methods commonly used for estimating internal dosimetry. To determine the precision and accuracy of each method using MC simulation as a gold standard.
- To assess intra- and inter- operator variability of dosimetry estimates for the different classical methods.
- To implement a MC method for estimating the personalized PET/CT dosimetry based on anatomical and functional images of the patient.

This thesis is structured as follows: *Chapter 1* discusses the fundamentals of nuclear medicine imaging. It discusses the physical principles that make nuclear medicine imaging and therapy possible with PET devices. It also provides background information about internal dose calculations. Furthermore, *Chapter 1* discusses some of the limitations of internal dose calculations in current practice, which provides the motivation for this thesis. In *Chapter 2*, a brief introduction to the problem and the objectives of

the thesis has been provided. *Chapter 3* describes in detail the transversal dosimetric tools applied in this dissertation for several applications in *Chapters 4-6*. *Chapters 4* and *5* are focused on the evaluation of the accuracy and precision of the performance of current internal dosimetry methods in clinic. In *Chapter 6* is described the development of a 3D image-based dosimetry technique using PENELOPE/penEasy MC code. It is also studied the application of this technique to PET simulated images where the organ activity distribution is known. Finally, in *Chapter 7* conclusions and a discussion of potential applications are included.

Chapter 3

Dosimetric Tools to Support Nuclear Medicine Imaging

The main purpose of this chapter is to gather and describe the utilization of dosimetric tools that have been used to carry out the tasks involved in this thesis work. MC SimSET code and STIR software were employed in the assessment of internal dosimetry estimates methods described in Chapter 4. It was used PENELOPE/penEasy MC toolkit in the implementation of patient-specific model defined in Chapter 6. Finally, OLINDA/EXM is introduced.

3.1 Dedicated MC Modelling Tool

3.1.1 SimSET Package

The *Simulation System for Emission Tomography (SimSET)* is a *dedicated* MC code for use in PET and SPECT [55,63]. SimSET is developed at the University of Washington Imaging Research Laboratory and freely available, uses MC techniques to model the instrumentation and the physical processes involved in both SPECT and PET imaging. It models the important physical phenomena including photoelectric absorption, Compton's scattering, coherent scattering, photon noncolinearity, and positron range. It supports a variety of collimator and detector designs, and already includes the attenuation properties for many common materials. The software is written in C-language and it consists of several modules. SimSET and its source code can be downloaded from `http://depts.washington.edu/simset`.

The central module is the *Photon History Generator (PHG)* which models the generation and transport of photons through attenuating media (object being imaged) to

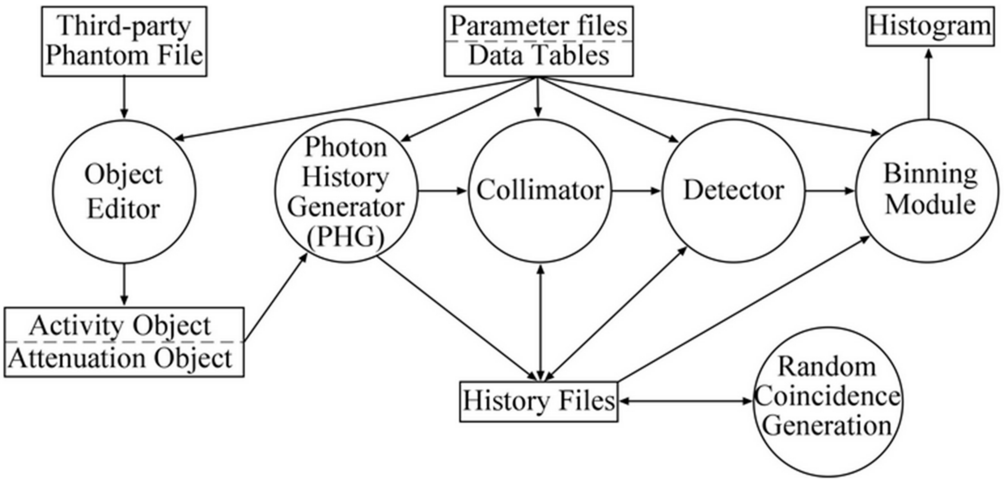

FIGURE 3.1: SimSET diagram.

the face of the collimator or detector. The *Collimator module* receives photons from the PHG and tracks them to the collimator. This module allows the user to choose a collimator's configuration depending on the system to be simulated. The *Detector module* receives photons either directly from the PHG module or from the Collimator module and tracks them in the specified detector, recording the interactions within the detector until they escape or all their energy has been deposited. This module allows the user to select the detector geometry and properties. The *Binning module* is used to process these interactions and generate the output data. It offers options to write the data in different histogram formats, such as sinograms. Photons can be selected for binning based on their deposited energy and scattering history. In PET simulations, the *Random Coincidence Generation module* can add random coincidences to a history file from the detector module before the binning processes the history file.

Each module creates a photon history file which contains information about the tracking of the photon, which can be used for further analysis of the simulation results. A diagram of the SimSET modules is shown in Figure 3.1.

3.1.1.1 Photon History Generator

It is the main module in SimSET package and generates photons and transports them through the object to the face of the collimator or detector. The inputs of PHG module are activity map, attenuation map, simulation options and data tables. Activity map defines the distribution of the isotope being simulated. Attenuation map defines the distribution of attenuating material being simulated. Both distributions are created by the *object editor*, which helps the user to define the activity and attenuation objects for the PHG expressed as voxel images. The simulation options are specified in a text file

(*phg params*) and data tables are supplied with the PHG package, providing information for operations like importance sampling and scatter modelling. The outputs of PHG module are the binned data, statistical information, photon history list, productivity table and simulation summary.

The simplified conceptual of the photon tracking algorithm is:

1. Sample the initial direction for the photon.
2. Sample the number of free-paths to travel before an interaction occurs.
3. Calculate the travel-distance corresponding to the selected free-paths, the attenuation values for all voxels encountered and the distance traveled through each voxel.
4. If the photon goes out the object without interacting, it is taken by the collimator/detector module. Otherwise, choose a scatter angle and corresponding energy value, and continue tracking.

The advantage of SimSET with respect to other MC package is that the PHG module never simulate the actual number of decays of a real scan, it simulates a smaller number. A weight is assigned to each decay which is determined by the volume in which it is generated, the amount of isotope assigned to that volume and the number of decays being simulated. Hence the weight is a number which can be used to easily convert histogram values to expected real-scan count rates.

3.1.1.2 Collimator Module

The Collimator module receives photons from the PHG and tracks them through the collimator being modeled. This module is very important for SPECT imaging where several collimators can be simulated. For PET, a collimator with axial segments is used when 2D acquisitions are carried out. Nevertheless, nowadays the most of PET scanners are operating in 3D mode and the axial segments are removed, it is the case of the studies taking into account in this thesis.

3.1.1.3 Detector Module

The Detector module receives photons either directly from the PHG module, this is our case when a 3D PET acquisitions are performed, or from the Collimator module. It tracks photons through the specified detector, recording the interactions within the

detector for each photon. The interactions are used to compute a detected location and total energy deposited. There are four supported detector types: planar (SPECT), dual head coincidence (PET), cylindrical (PET), and block (PET and SPECT) detector models, together with a 'simple' model in which only the Gaussian energy blurring is performed. The Cylindrical detector contains a series of adjacent regular right cylinders with transaxial layers.

The Detector module uses a detector parameter file to select both the detector model and other detection parameters such as the reference energy (511keV for PET) and the energy resolution percentage (FWHM).

The output of Detector module contains the total deposited energy, energy weighted centroid, list of interaction positions and energy deposited, and detector position. This information is passed from the Detector module to the Binning module.

3.1.1.4 Binning Module

The Binning module is used to process the photon and detection information. The photons are sorted into multi-dimensional histograms (sinograms) where photon or detection records are binned according to their transaxial distance and azimuthal angle.

The binning module can be used during the simulation as each record is accepted (on-the-fly), or it can be used after the simulation via processing a standard history file. The binning can be carried out according to photon energy (number of energy bins for each photon and energy window) and scattering history (separating for example trues from scattered photons). So, the binning step is defined by the user and it is another input file in the simulation.

The SimSET output data can be obtained as the sum of the coincidence weights in each detector pixel (bin) and the sum of the squares of the weights. Apart from the image projections onto the tomography detectors, SimSET also presents a statistical summary with the most relevant results from the simulation.

3.1.1.5 Random Coincidence Generation Module

SimSET offers direct simulation of randoms combined with the coincidence simulation. This option requires several steps and takes considerably more CPU time; this option is only recommended in cases where the computation from singles is likely to be inaccurate.

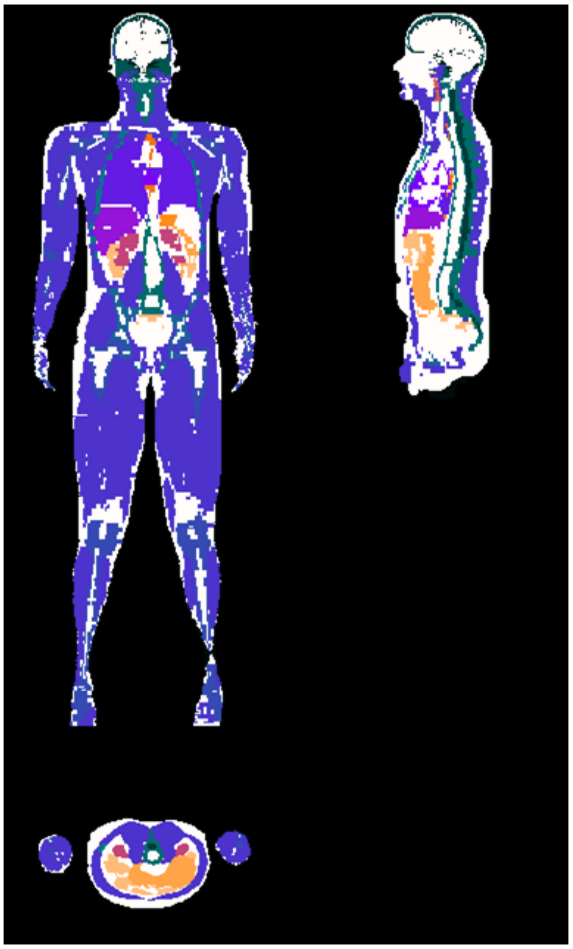

FIGURE 3.2: Saggital, coronal and transverse slice through the voxel-based Zubal phantom.

3.1.2 Object Geometry

A numerical phantom [64] was used to mimic the normal activity distribution of radioligands in PET studies. Zubal phantom[1] is a digital representation of an adult male obtained from a CT scan. The data has been segmented into about 50 different tissue types. The original dataset consists of $243 \times 128 \times 128$ *voxels*, with 8-bit depth. Each tissue type is represented by an arbitrary integer. An attenuation index translation table specially designed for the Zubal phantom is provided with the SimSET package. This translates the arbitrary tissue numbers in the original phantom into appropriate attenuation values for the different tissue types. In this thesis it has been used the Zubal phantom with legs and arms attached such as figure 3.2 shows.

[1] http://noodle.med.yale.edu/zubal/

3.1.3 Simulations

In the context of this thesis we used SimSET (version 2.9) MC package in order to simulate a General Electric Discovery ST PET/CT scanner. For 3D PET simulations three modules were required: PHG, detector and binning module. In order to reduce simulation time *multiple binning* files were created and were analyze on-the-fly, therefore it was used *Tomograph File* feature. Furthermore, forced detection and stratification were applied as a variance reduction techniques. The simulation conditions used in these modules are detailed in section 4.2.2.

We took advantage of the fact that SimSET simulation is intrinsically additive with the result, so dozens simulations were carried out in such a way that noise was 100 times less than noise obtained in real acquisitions. Thus, our simulations can be regarded as being noise-free simulations.

3.2 STIR Software

STIR [2] (Software for Tomographic Image Recosntruction) [65] is a flexible open source object-oriented C++ library for 3D PET reconstruction. It offers both analytic (FBP 2D and FBP 3D) as well as iterative reconstruction algorithms (OSMAPOSL - *Ordered Subsets Maximum A Posteriori One Step Late*, which reduces to OSEM or MLEM for appropriate parameters). STIR has been widely used in the scientific community, especially for first evaluations of new scanner designs. The reconstruction is based on 3D sinograms with a corresponding header file defining the dimensions. The MC simulations obtained by using the SimSET package cannot be directly reconstructed by using the algorithms included in the STIR library. For this reason, a program have been implemented and incorporated in STIR library to convert the SimSET sinograms to STIR's Interfile format. In this thesis were employed three different methods to reconstruct our data: FBP 2D, FBP 3D and OSEM (see section 4.2.3).

3.3 General MC Modelling Tool

3.3.1 PENELOPE/ penEasy code

PENELOPE [66, 67], an acronym that stands for PENetration and Energy LOss of Positrons and Electrons, is a general-purpose Monte Carlo simulation package that describes the transport of electrons, photons and positrons in any material and for the

[2] http://stir.sourceforge.net/

energy range from 50 eV to 1 GeV. PENELOPE, which is coded in Fortran90, is free and open source. It was developed at the Universitat de Barcelona and it is distributed by the Nuclear Energy Agency (NEA) [3].

Photons are simulated following a detailed procedure, in other words, their interactions are followed in chronological succession one by one until de photon reaches energy lower than a user-defined threshold (the absorption energy E_{abs}). For charged particles is adopted a mixed simulation scheme which distinguishes between hard and soft events. Hard events are those in which the energy loss and/or the change of the particle direction are larger than the given cutoffs. These events are simulated according to a detailed scheme (as for photons). If these conditions do not occur, events are said to be soft and are simulated using a condensed scheme based on multiple scattering theory. The cutoffs are determined by five user-defined transport parameters: C_1 and C_2 control the cutoff for elastic collisions, W_{CC} and W_{CR} are the cutoffs for inelastic and bremsstrahlung interactions, respectively and DS_{MAX} is an upper limit for the step length. If these parameters are all set to zero, PENELOPE effectively performs a detailed simulation of charged particle transport.

In PENELOPE, users are responsible for writing a steering main program that defines the source of particles, the simulation parameters, the quantities of interest to be scored, the VRTs to be applied and report the final results. The code penEasy[4] [68] , which is both free and open source, provides a general-purpose modular main program for PENELOPE. It needs many input files to run the simulation and provides different output tallies (figure 3.3). It was developed at the Institut de Tècniques Energètiques (Universitat Politècnica de Catalunya).

3.3.2 Geometry Construction

In penEasy, a geometry model capable of accommodating objects described in terms of quadric surfaces, voxels, or a superposition of both has been developed. The quadric geometry is handled by invoking PENELOPE's standard geometry package, called PENGEOM. For the simulation of voxelized geometries a set of transport routines named penVox is provided. This model accepts a list of voxels as input, each one defined by their material index and mass density. PenVox has been employed in this thesis, the list of voxels, their composition and density has been obtained by processing patients' CT scans [69, 70] or voxelized phantoms which emulate a CT, as it is described in Chapter 6.

[3] http://www.nea.fr
[4] http://www.upc.es/inte/downloads/penEasy.htm

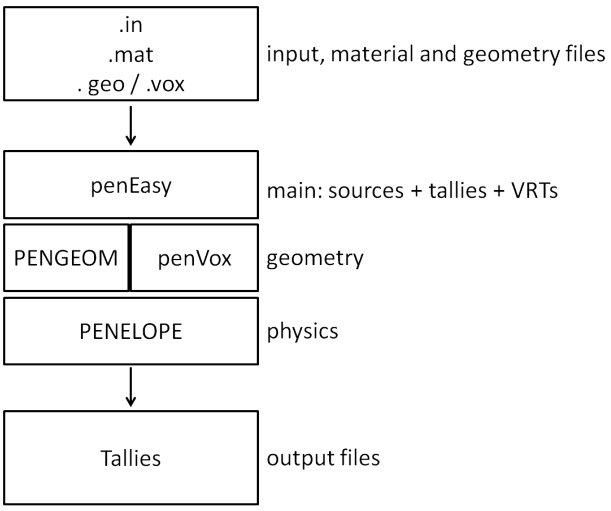

FIGURE 3.3: PENEASY diagram

.

3.3.3 PenEasy Tallies

PENEASY includes subroutines to score the most common quantities of interest. The tallies available in the current version are listed below.

- *Tally Spatial Dose Distrib*: estimates the absorbed dose per simulated history in bins defined by the user.
- *Tally Cylindrical Dose Distrib*: estimates the absorbed dose per simulated history in cylindrical volume elements defined by the user.
- *Tally Spherical Dose Distrib*: estimates the absorbed dose per simulated history in spherical volume elements defined by the user.
- *Tally Energy Deposition*: estimates the energy deposited per simulated history in each material.
- *Tally Fluence Track Length*: estimates the fluence spectrum integrated over the volume of the declared detection material.
- *Tally Phase Space File*: The state of all particles reaching the specified detection material is written in the output file.
- *Tally Particle Current Spectrum*: it is reported, classified according to the particle type, the energy spectrum of the particles that enter the specified detection material per unit simulated history.
- *Tally Particle Track Structure*: particle coordinates after each interaction (together with some other information) are written to an external file.

- *Tally Pulse Height Spectrum*: energy deposited by each history in the specified detection material is classified into energy bins.
- *Tally Voxel Dose Distrib*: estimates the absorbed dose per simulated history in each volume element(voxel) defined by the user.

3.3.4 Simulations

In the context of this thesis we used PENELOPE (version 2011 and 2014) with penEasy (version 20120601 and 20170510). Patient/phantom PET images were used as the particles source for the dose distribution calculation on the own patient/photon. For this purpose, it was modified the Box Isotropic Gauss Spectrum (BIGS) source model, which is included in penEasy (see 6.2.2). The isotope was simulated through the corresponding energy emission spectrum. Simulation parameters are described in detailed in section 6.3.2. VRT were not applied.

3.4 OLINDA/EXM code

The OLINDA/EXM (*O*rgan Level INternal Dose Assessment/EXponential Modeling) [41, 71] personal computer code performs dose calculations and kinetic modeling for radiopharmaceuticals. It implements the methods outlined by the RADAR group for internal dose assessment [72], which was described in section 1.8. These doses are estimated based on organ level DF (*dose factor*) calculated for standard phantoms representing the average male or female where DF is the mean absorbed dose to the target organ, t from unit activity of the relevant radioisotope distributed within the source organ S. The dose is given by summing up the contributions from all source organs.

In this thesis it was used OLINDA/EXM program (version 1.0), time-integrated activity coefficients were inputted into the code, which use the Cristy and Eckerman anthropomorphic phantoms [47] and a isotope database over 800 radionuclides in order to obtain dose estimations.

Chapter 4

Impact of region-of-interest delineation methods and reconstruction algorithms on internal dosimetry estimates using PET

This chapter presents an evaluation of the performance of current ROI delineation methods and reconstruction algorithms on the accuracy of internal dosimetry estimates. Simulated PET studies for two radioligands with different biodistribution have been developed as a gold standard to which compare these delineation methods.

4.1 Introduction

As previously mentioned in Chapter 1, estimation of radiation exposure affecting human subjects undergoing PET exploration plays a central role in the development of new radioligands. Internal dosimetry estimates for each radioligand are essential to calculate the safety limits of injected activity and the maximum number of scans that a subject can undergo. In a diagnostic context, these procedures imply the administration of activity levels that do not lead to the appearance of radiation deterministic effects; therefore, only stochastic risks have to be considered. However, in any use of ionizing radiation, one must prevent or minimize the risks of the use of the radiation while allowing its beneficial applications.

Radiation exposure estimations are, in general, obtained from biodistribution and dosimetry studies where the time course of the distribution of radioligand in organs and tissues is measured. In these kind of studies, multiple whole-body PET scans are acquired after radioligand injection and regions-of-interest (ROIs) placed on the images are used to measure the amount of radioactivity in each organ over time. Time-integrated activity coefficients are then calculated from the time course of the radioligand and are used by software packages such as Olinda/EXM [73] to obtain dosimetry estimates.

Several methods for delineating ROIs and quantification of dosimetry estimates are currently being used. Whole-organ ROIs are drawn on high-resolution structural images (computed tomography (CT) or magnetic resonance imaging (MRI)) for easier identification of the organs and then forward projecting the ROIs to the coregistered PET datasets [74, 75]. However, this manual ROI delineation method is a tedious and time-consuming task, even for experts. As a consequence, simplified methods in order to expedite ROI drawing are also employed. One of these methods suggests delineate ROIs on subsamples of the organs to obtain the mean activity concentration, along an approximation of organ volume [76–78]. A further simplification consists of compressing PET images into a single antero-posterior planar image and drawing planar ROIs on it [79–82]. However, delineation and overlapping organs may lead to biased results. There have been several attempts to compare the performance of these methods [5, 82, 83]. Nevertheless, the absence of a gold standard with which to compare the dosimetry estimates obtained have made it impossible to draw conclusions about the accuracy of these methods.

Monte Carlo (MC) simulations are an important tool in the assessment and optimization of image processing methods in nuclear medicine. MC simulations provide an adaptable environment where the ground truth is known and where the realism of the input models can be suitable reproduced. Dedicated MC codes (SimSET, GATE) for PET/SPECT systems, are well known for its efficiency in the simulation of voxel-based objects [84].

PET image quality, which is related to the reconstruction method used, the corrections for degrading factors applied (randoms, attenuation, scatter, and partial volume) and the number of counts acquired, is another factor to consider in dosimetry studies. Several reconstruction methods, based on the filtered back-projection (FBP) and on the ordered-subsets expectation-maximization (OSEM) algorithm [34] are currently being used. Corrections such as attenuation, randoms and dead time are routinely applied since they have been shown to increase image quality and quantification accuracy. Scatter correction is also usually applied, but most of the commercial tomographs apply simplified scatter correction methods that only take into account a single scatter

correction [85, 86]. Although there is extensive literature comparing the performance of both methods in whole-body [87] and brain [88] studies, little is known about their performance in dosimetry studies.

4.2 Implementation of a Numerical Model

4.2.1 Reference Case Studies

Two different radioligands with distinct biodistribution and kinetics were simulated ([^{11}C]raclopride and [^{11}C]GSK931145). The main route of clearance for [^{11}C]raclopride was urinary, while the principal route of clearance for [^{11}C]GSK931145 was considered to be intestinal. The voxel-based Zubal phantom with arms down [64] was used to generate a realistic anatomical model for subsequent Monte Carlo simulation. The original whole-body phantom was rebinned to a size of $64 \times 64 \times 200$ *voxels*, with a voxel size of $10 \times 10 \times 10$ mm^3. Nine activity models reproducing the radiotracer concentration in each organ over time were created. Each model reproduced a different time point after injected activity. A homogeneous activity to each organ was assigned using time-activity curves of the simulated radioligands extracted from previously published human PET data [5, 76, 77]. Attenuation maps were created from the Zubal phantom segmented into three different tissues: lungs, bone and soft tissue.

4.2.2 PET Image Simulations

PET acquisitions were simulated using SimSET [1] [55] Monte Carlo code (version 2.9), which was configured for a General Electric Discovery ST PET/CT scanner [89], table 4.1 described the main technical characteristics of the scanner. The detector was modeled as a single ring of bismuth germanate (BGO) material. The energy window was 375–650 keV, and simulations were performed in 3D. The output sinograms covered a 15.7 cm axial field of view (FOV). The number of transaxial and angular bins were 128 and 140, respectively, and 192 was the number of axial slices (1 cm slice size) [90]. Eight bed positions each corresponding to the dimension of the scanner axial FOV were independently simulated to achieve whole-body coverage. An overlap of 1.3 cm (corresponding to four slices) was considered between two consecutive bed positions to compensate for the loss of sensitivity on both extremities of the axial FOV. To realistically simulate the noise levels in dynamic PET studies, firstly, noise-free sinograms (noise in simulations was 100 times less than noise obtained in real acquisitions) were scaled to have the same number

[1] http://depts.washington.edu/simset

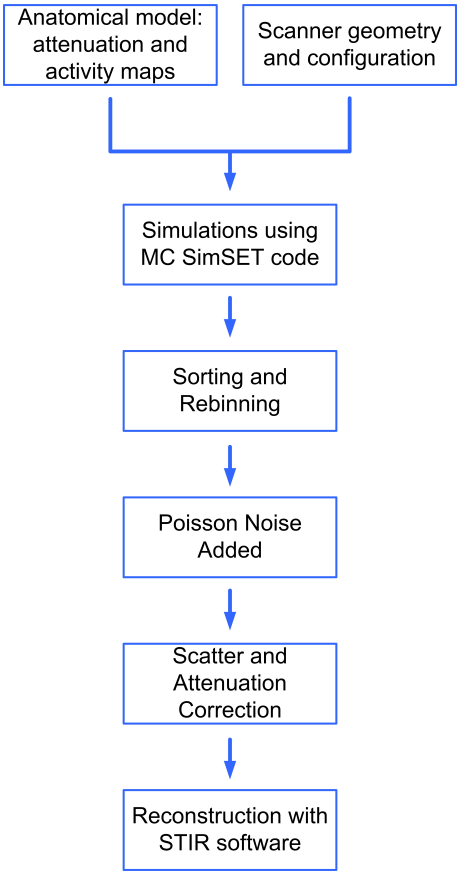

FIGURE 4.1: Current setup of the development of a numerical phantom showing the major processing steps.

of counts as in a clinical scan [91]. Secondly, Poisson distribution noise was added to each of them to mimic the number of counts collected per frame in realistic dynamic PET studies. True coincidences, single scatter coincidences and multiple scatter coincidences were stored in separate files to assess the effect of Compton scatter. Then, standard PET corrections were made [43]. Two different scatter correction methods were applied on the sinogram: (a) an ideal scatter correction (ISC) which considered only true coincidences on the sinograms [92] and (b) ideal single scatter correction by subtracting Monte Carlo simulated single scatter coincidences from the sinograms. Attenuation correction and rebinning (single-slice rebinning algorithm [93]) were performed on the sinograms for the true coincidences before reconstruction. Figure 4.1 shows the major processing steps carried out to create a numerical phantom. Forced detection was applied as importance sampling technique in order to accelerate the simulations. The total time to generate the simulation data of a bed varies depending on the source organ and the bed position. So, the time can range from 1 to 40 days using 2 or 3 CPUs in parallel.

4.2.3 Reconstruction Algorithms

STIR [65] was employed to reconstruct the data using three different methods (http://stir.sourceforge.net): (a) 2D filtered back projection (FBP 2D) (transaxial filter: ramp, cutoff 0.2 cycles); (b) 3D filtered back projection (FBP 3D): 3D reprojection (transaxial filter: ramp, cutoff frequency 0.2 cycles; axial filter: Colsher, cutoff frequency 0.5 cycles); and (c) OSEM: number of subset: 5; number of iterations, from 1 to 20. The resulting images consisted of nine frames of volumes of the size $128 \times 128 \times 47$ mm^3. The voxel size was $5.47 \times 5.47 \times 3.34$ mm^3.

4.2.4 Calibration Factor Estimation

Activity units were obtained after calibration using a SimSET Monte Carlo simulation of a homogeneous cylindrical phantom with the same parameters as those used for the simulation of the dosimetry study, as it has been described in subsection 4.2.2. A calibration factor was obtained for the reconstruction algorithms applied.

4.3 SimSET Validation

4.3.1 PET System Assessment

This section is focused on the validation of the SimSET code for the PET system described in 4.2.2 based on a GE Discovery ST PET/CT scanner. To perform the validation, we obtained SimSET MC simulations of a numerical phantom and we compared them to the experimental measurements.

TABLE 4.1: Main Technical Caractheristics of a GE Discovery ST PET/CT scanner.

Main Technical Caractheristics			
Detector ring diameter (cm)	88.6	No. of detector blocks	280
Detector material	BGO	No. of detector modules	35
No. of individual crystals	10080	Tungsten collimator size (mm)	0.8×54
No. of crystals/ring	420	Axial FOV (cm)	15.7
No. of detector rings	24	Transaxial FOV (cm)	70
No. of image planes	47	Axial sampling interval (mm)	3.27
Crystal size (mm^3)	$6.3 \times 6.3 \times 30$	Coincidence window width (ns)	11.7
Face of crystal block (mm^2)	38×38	Energy window (keV)	375-650
Crystal in a block	6×6	Angular bins in sinogram	210
Crystal in a block	6×6	Transaxial bins in sinogram	249

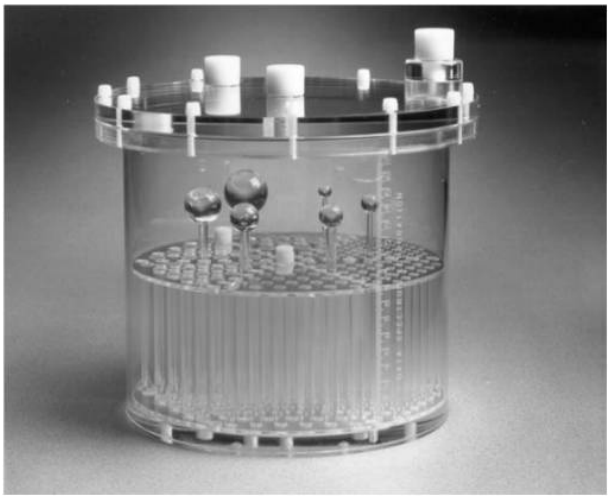

(a)

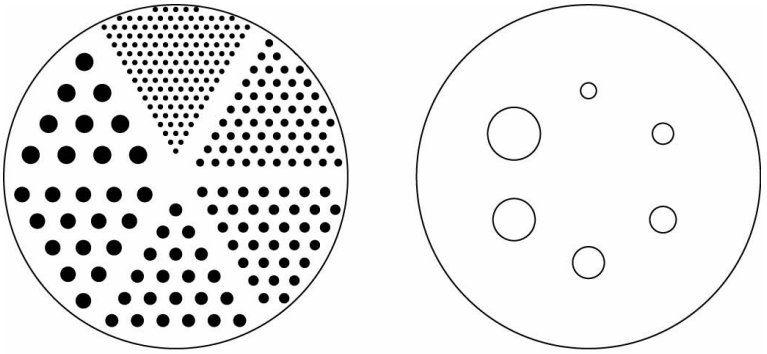

(b)

FIGURE 4.2: A Deluxe Jaszczak Phantom. (a) components (b) position and diameter of 148 cold rods in 6 sectors and 6 cold spheres.

Geometrical Phantom

The test was based on an Ultra Deluxe model of Jaszczak Phantom with defined geometry (fig. 4.2) . This phantom provides information regarding the performance of SPECT and PET imaging devices [94, 95]. It was constructed of a clear Acrylic Plexiglass material and consists of six spheres with different diameters and 148 rods in 6 sectors.

There are various accessory inserts available for Jaszczak phantom; in this validation the hollow sphere and micro-hollow sphere sets were used (fig. 4.3). These sets intend to simulate hot and cold spherical "lesions" for quantitative evaluation of spatial resolution, attenuation and scatter effects. Specifications of these components are described in Table 4.2.

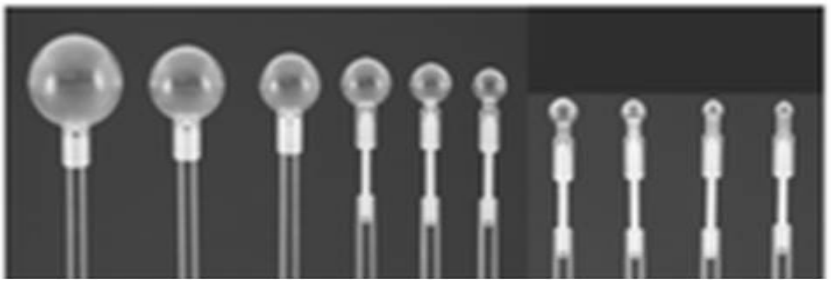

FIGURE 4.3: Hollow and Micro-Hollow Spheres set for circular and elliptical Jaszczak phantom.

In order to perform the MC simulations, a numerical phantom was obtained from the digitalization of the acquired CT of the Jaszczak phantom. The activity map was obtained by considering the holes as the only hot regions and the attenuation map was obtained by considering an attenuation coefficient of 1.00 g/cm^3 for water and 1.18 g/cm^3 for polymethyl methacrylate.

Experimental Data Acquisition

A Jaszczak Ultra Deluxe phantom scan was acquired in a GE Discovery ST PET/CT scanner using a protocol in 3D mode at the Molecular Imaging Centre (CRC-CIM) in the Barcelona Biomedical Research Park (PRBB). The phantom was filled with water and the six co-axial isocentre spheres with different diameters were uniformly filled with a known solution of water and ^{18}F-FDG. The phantom was then mounted on the standard bed and centred in the transverse and axial FOV. Prior to emission scan, a CT scan was acquired and used for subsequent attenuation correction. The duration of the emission scan was 20 min. Finally, images were reconstructed using a 3D ML-OS-EM reconstruction algorithm [96] to generate $128 \times 128 \times 47$ *voxel volumes* ($3.91 \times 3.91 \times 3.27$ mm^3). Two acquisitions were performed, one with hollow sphere inserts and one with micro-hollow sphere inserts.

TABLE 4.2: Specifications of Hollow and Micro-Hollow Spheres set.

Hollow Sphere Inserts		Micro-Hollow Sphere Inserts	
Diameter (mm)	Volum (mL)	Diameter (mm)	Volum (mL)
31.2	16.0	7.8	0.25
24.8	8.0	6.2	0.125
19.7	4.0	4.9	0.063
15.6	2.0	3.9	0.031
12.4	1.0		
9.9	0.5		

SimSET Simulation Data Acquisition

PET acquisitions were simulated configuring the Monte Carlo code for a GE Discovery ST scanner, as it was described in section 4.2.2. The STIR package was used to reconstruct the images of Jaszczak phantom simulations.

Results

Phantom PET images were coregistered with the simulated images, and a scaling factor was applied to this simulated data to replicate the acquired counts in the experimental PET scans (fig. 4.4). The profiles of the PET scanned data and simulated measurements were normalized to the same maximum in order to compare and evaluate them after delineating the appropriate ROIs. The resulting profiles are shown in figures 4.5 and 4.6.

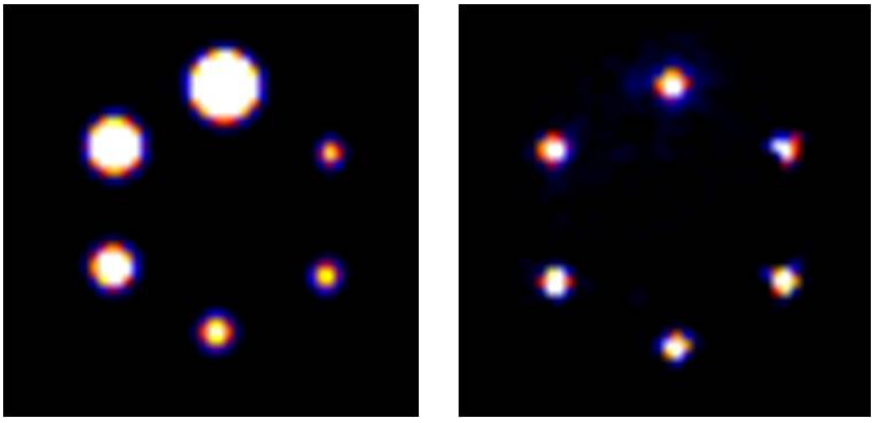

(a)

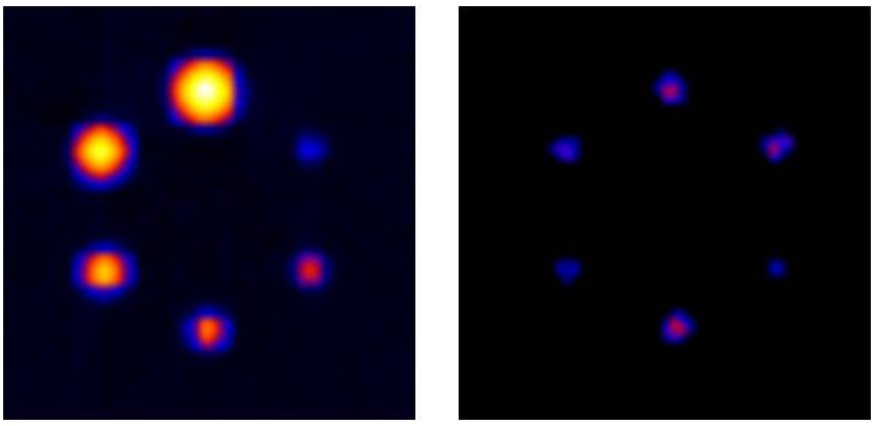

(b)

FIGURE 4.4: Coregistered Jaszczak phantom images with hollow and micro-hollow sphere inserts of (a) experimental PET scans and (b) simulation scans in a transverse slice.

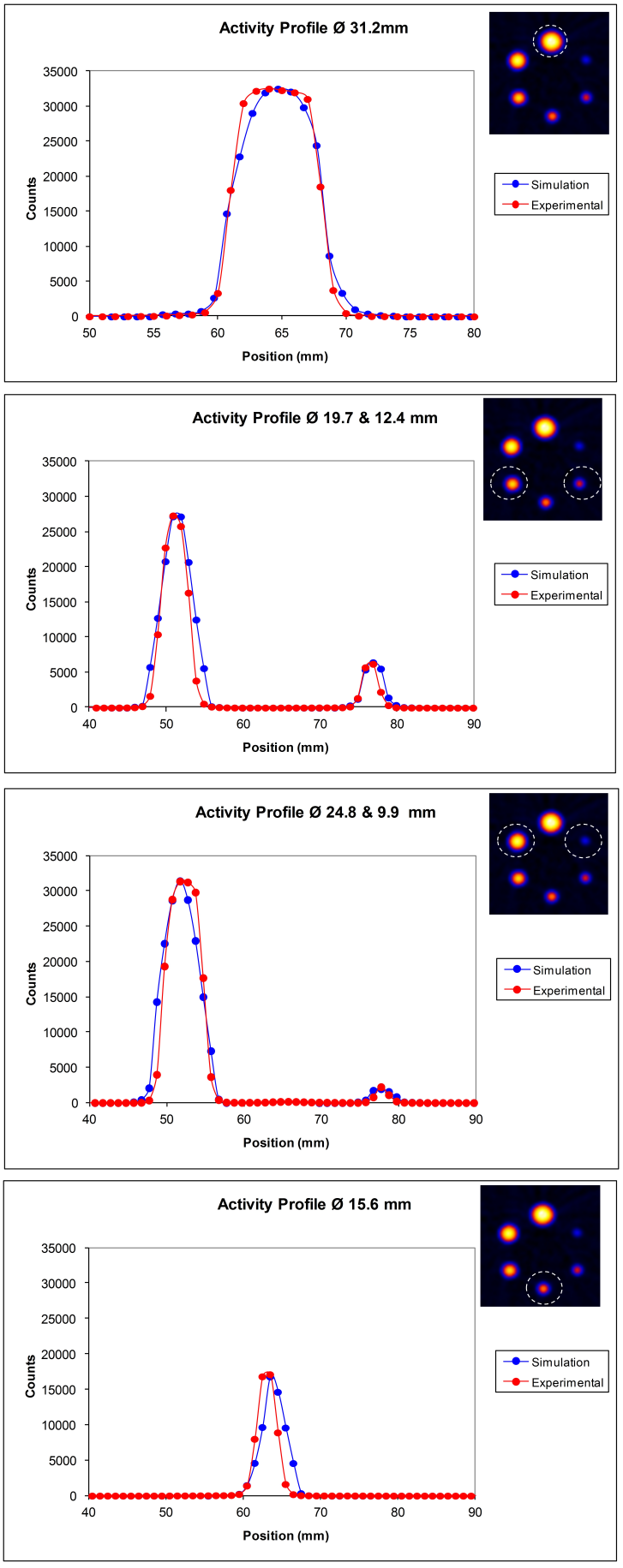

FIGURE 4.5: Activity profiles of the large spheres scanned image and simulated image.

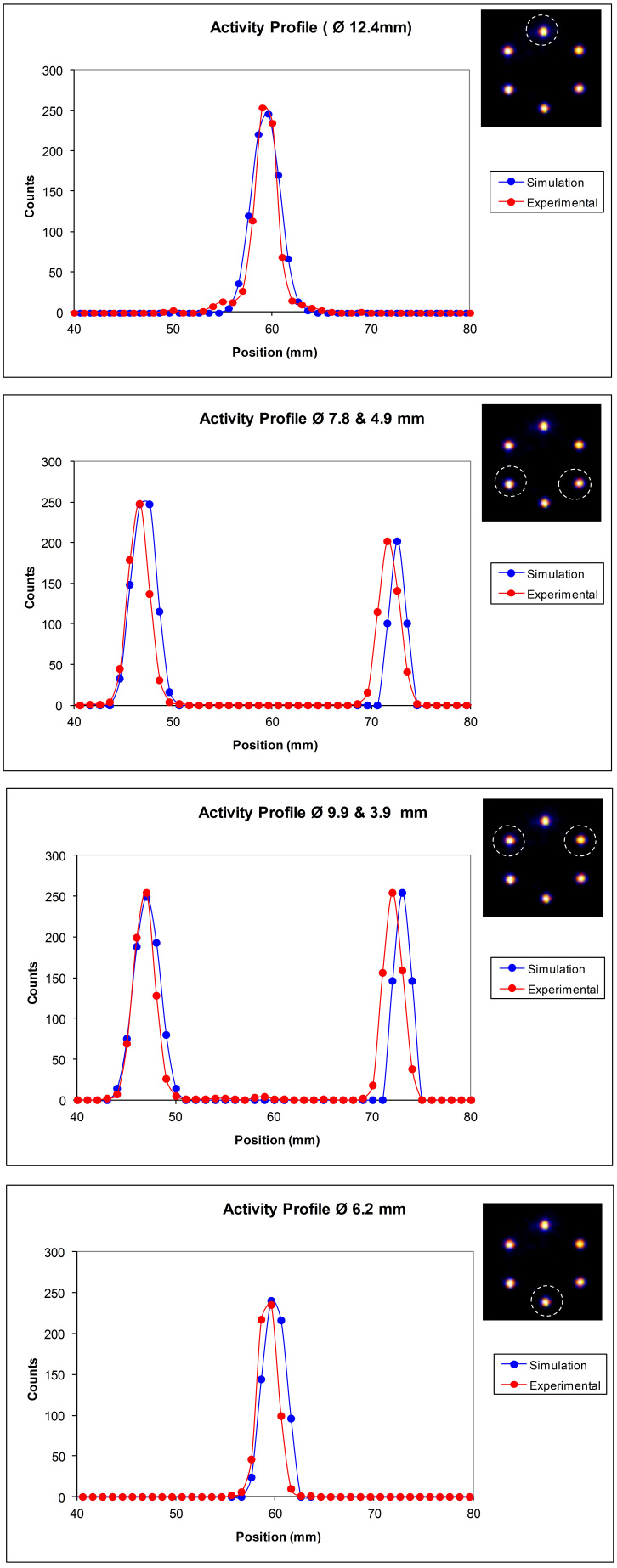

FIGURE 4.6: Activity profiles of the small spheres scanned image and simulated image.

Measurements of the variation of the full width at half maximum (FWHM) were taken at different slices of the axial FOV for all spheres considered. We found a maximum discrepancy of 0.7 mm between simulated and experimental results. We observed an average discrepancy between simulated and measured results of 12.21% for FWHM. Tables 4.3 and 4.4 show the values of the FWHM estimated. Data profiles provided a reasonable agreement between experimental and simulation images for both cases, large and small spheres.

TABLE 4.3: FWHM in mm from simulations and real experiments scanned images for large spheres considered.

	ϕ Hollow Spheres Inserts (mm)					
	31.2	24.8	19.7	15.6	12.4	9.9
FWHM (mm)						
Experimental	7.28	5.38	3.95	2.99	2.38	1.77
Simulation	7.33	5.74	4.36	3.49	3.09	2.34

TABLE 4.4: FWHM in mm from simulations and real experiments scanned images for small spheres considered.

	ϕ Micro-Hollow Spheres Inserts (mm)					
	12.4	9.9	7.8	6.2	4.9	3.9
FWHM (mm)						
Experimental	2.55	2.56	2.53	2.45	2.54	2.47
Simulation	3.13	3.17	3.15	3.00	2.00	1.92

4.3.2 Attenuation Correction Assessment

Attenuation correction using Monte Carlo SimSET code utilities has been validated. A simulation of a homogeneous cylinder phantom was carried out with the specific parameters based on GE Discovery ST PET/CT scanner.

The phantom was simulated to be uniformly filled with a positron emitter source. There were considered two cases: (i) attenuated cylinder and (ii) non-attenuated cylinder, in both scenarios with 10^{10} simulated particles, of which 10^8 reach the detector. The output sinogram of the attenuated cylinder was considered with and without attenuation correction. The application of this correction required that the sinogram to be multiplied with an attenuation correction map. Filtered back-projection was considered to reconstruct the images employing STIR software.

Visually, the implementation of attenuation correction to the sinogram improved the quality of the reconstructed image (fig. 4.7). The effects of attenuation correction to the image can be clearly seen, as shown in figure 4.8(b). Higher activity at the edge of the phantom image was eliminated after attenuation correction implemented. The

attenuation corrected image shows more uniform distribution of activity throughout the phantom. This effect was seen by comparing the line profile for the images before and after correction (fig. 4.9). Implementation of attenuation correction cause the intensity profiles more uniform. However, the variability of the profile of the data with attenuation correction would be more stable with a greater number of simulated particles. Moreover, attenuation correction induces additional statistical noise in corrected PET images.

In order to estimate the calibration factor described in subsection 4.2.4, the simulation of the homogeneous cylindrical phantom with attenuation correction was carried out again with a greater number of simulated particles.

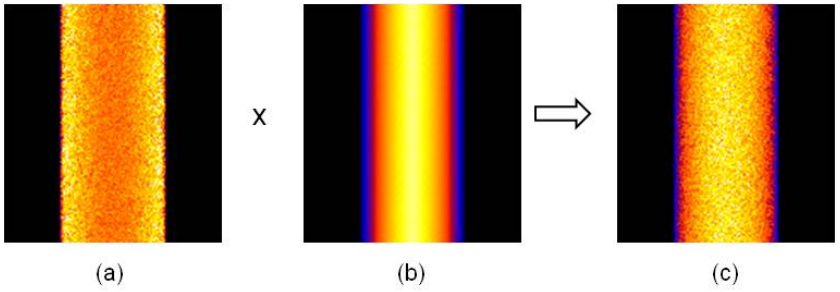

FIGURE 4.7: The attenuation correction step: multiplication of the emission sinogram with the attenuation correction map (a) original sinogram, (b) attenuation correction map and (c) attenuation corrected sinogram.

4.4 Classical Methods on Internal Dosimetry

4.4.1 Delineation Methods

Dosimetry was estimated by using three ROI delineation methods differing in their complexity and execution time. ROIs were drawn on the following organs using MRIcro software: brain, heart, lungs, stomach, liver, gallbladder, intestine, kidneys, urinary bladder and cortical bone [97]. For planar images, the user draws a region on the image by using the available MRIcro tools. In 3D methods, the drawing is performed on each slice encompassing the volume of interest and the set of resulting regions are then combined to form a 3D volume [98]. These ROIs were drawn in three different ways:

Antero-Posterior Compressed Images (AP)

Images were compressed by projecting the reconstructed images in the antero-posterior direction to obtain planar images. ROIs were drawn on the planar images (one single slice) covering the entire organ; it was done six times by four different operators due to

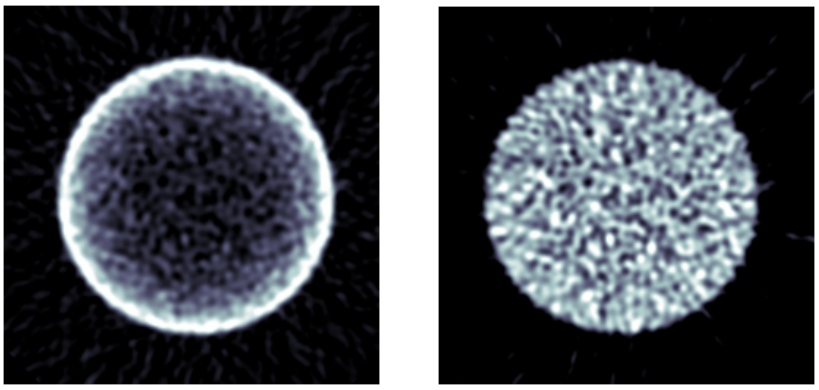

(a) (b)

FIGURE 4.8: Comparison of images before and after attenuation correction. (a) Before attenuation correction (b) after attenuation correction.

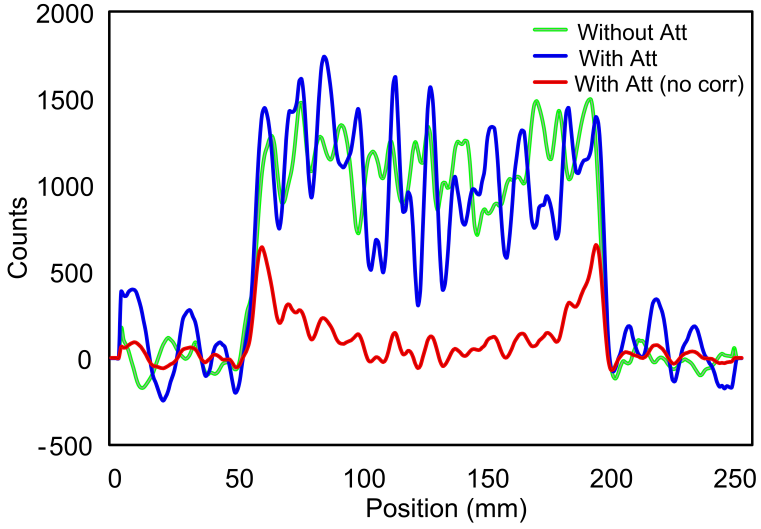

FIGURE 4.9: Profiles of the attenuated simulation data with and without correction, and no attenuated simulated data.

the variability expected using this method. Results were expressed as the mean value and the uncertainty in the mean.

Subsample of the Organs (S)

Spherical ROIs were applied on 3D images, and only the center and radius of the ROI were fixed interactively using the graphical interface. For reference simulated data, ROIs were scaled according to the organ volumes derived from Zubal phantom and a same operator has drawn ROIs three times. Results were expressed as the mean value and the uncertainty in the mean. In addition, to assess the variability of the results on organ size, variations within $\pm$ 20% in organ volumes were applied from the anatomical regions of the Zubal phantom.

Whole Organ (W)

For reference simulated data, we considered (i) the optimal case using ROIs obtained from the anatomical regions of the Zubal phantom and (ii) to assess the variability of the results on organ size; variations within ± 20% in organ volumes were applied from the anatomical regions of the Zubal phantom.

4.4.2 Time-Integrated Activity Coefficients and Absorbed Dose Calculations

ROIs delineated using the methods described in the previous section were applied to the PET images to obtain time-activity curves. The area under the noncorrected time-activity curves (TACs) was calculated with the trapezoidal method of integration [43]. To be conservative, we calculated the area under the curve from the final data acquisition to infinity by assuming that decline in radioactivity occurred only by physical decay. The area under the time-activity curve of the source organ from time zero to infinity divided by the injected activity is equivalent to the time-integrated activity coefficient ($\tilde{a}(r_s, T_D)$). The ($\tilde{a}(r_s, T_D)$) for all the source organs was summed and subtracted from the true total time-integrated activity coefficient value ($T_{1/2}/ln2 = 0.49\ h$) to calculate the ($\tilde{a}(r_s, T_D)$) of the remainder of the body ($T_{1/2}$: the radioactive half-life of C-11). Time-integrated activity coefficients were inputted into OLINDA/EXM (version 1.0) software [1], and a 70 kg adult male and a 55 kg adult female phantom were used to obtain both organ AD and ED.

4.4.3 Reference Dose Estimations

Reference TACS from the considered studies [5, 76, 77] were also inputted into OLINDA/EXM to obtain the true dosimetry estimates for comparison purposes.

4.5 Results

4.5.1 ROI Method Comparison on Simulated PET Images

Figure 4.10 shows transverse slices of the resulting images over time, showing the biodistribution and routes of excretion of [^{11}C]raclopride and [^{11}C]GSK931145. As we have already pointed out, both biodistributions simulated high activity in the liver for early scans. As expected, activity in the contents of the stomach and small intestine was

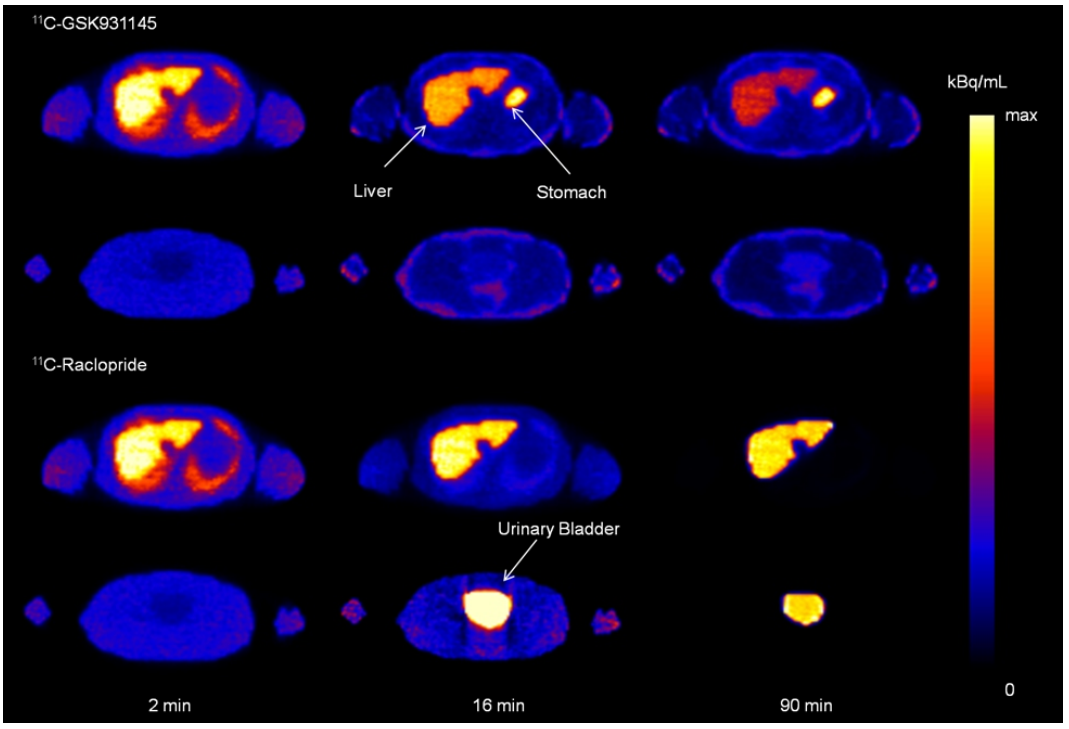

FIGURE 4.10: Illustative transverse slices showing the simulated biodistribution of a [^{11}C]GSK931145 and b [^{11}C]raclopride (bottom) in whole-body PET images at 2, 16, and 90 min after injection of the radioligand. For each radioligand, two slices at the level of the liver and urinary bladder are shown. Images reconstructed using OSEM and ISC.

present in [^{11}C]GSK931145 biodistribution where the simulated route of clearance was intestinal. Activity in the urinary bladder was present in [^{11}C]raclopride biodistribution simulating urinary excretion.

4.5.2 Reconstruction

Effective dose estimates using images reconstructed using OSEM increased their value when the number of iterations was increased until a plateau was reached after approximately 15 iterations. Using the W ROI delineation method for the [^{11}C]GSK931145 distribution, no differences in ED estimates were found when OSEM, FBP 2D, and FBP 3D were applied (Fig. 4.11). The same pattern was found when S and AP ROI delineation methods were applied.

No significant differences (less than 1%) were found in ED estimates when using full scatter correction and single scatter correction.

For the sake of simplicity, from now onward, results are referred to simulated PET images reconstructed using FBP 2D algorithm and ideal scatter correction.

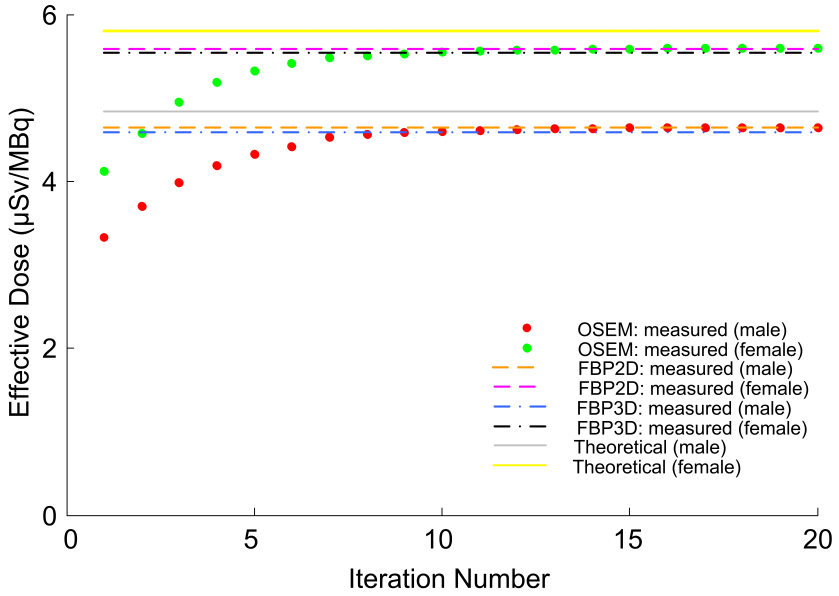

FIGURE 4.11: Comparison of the reconstruction algorithm applied: FBP2D, FBP3D, and OSEM with five subsets and from 1 to 20 iterations, which corresponds to positions 1 to 20 on the x-axis. Values are the effective dose estimates for the [^{11}C]GSK931145 distribution whole-body ROI delineation method.

4.5.3 Delineation Methods

Measured and true TACs showed close agreement when S and W ROI delineation methods were used. When the AP method was used, measured TACs presented higher activity than simulated TACs in those organs where the ROI enclosed the whole organ (heart, lungs, and liver) (Figs. 4.12 and 4.13).

However, lower activity in the TACs in comparison with the simulated ones was found for the AP method for those organs where only a portion of the organ was delineated (kidneys and intestine) due to overlapping between organs.

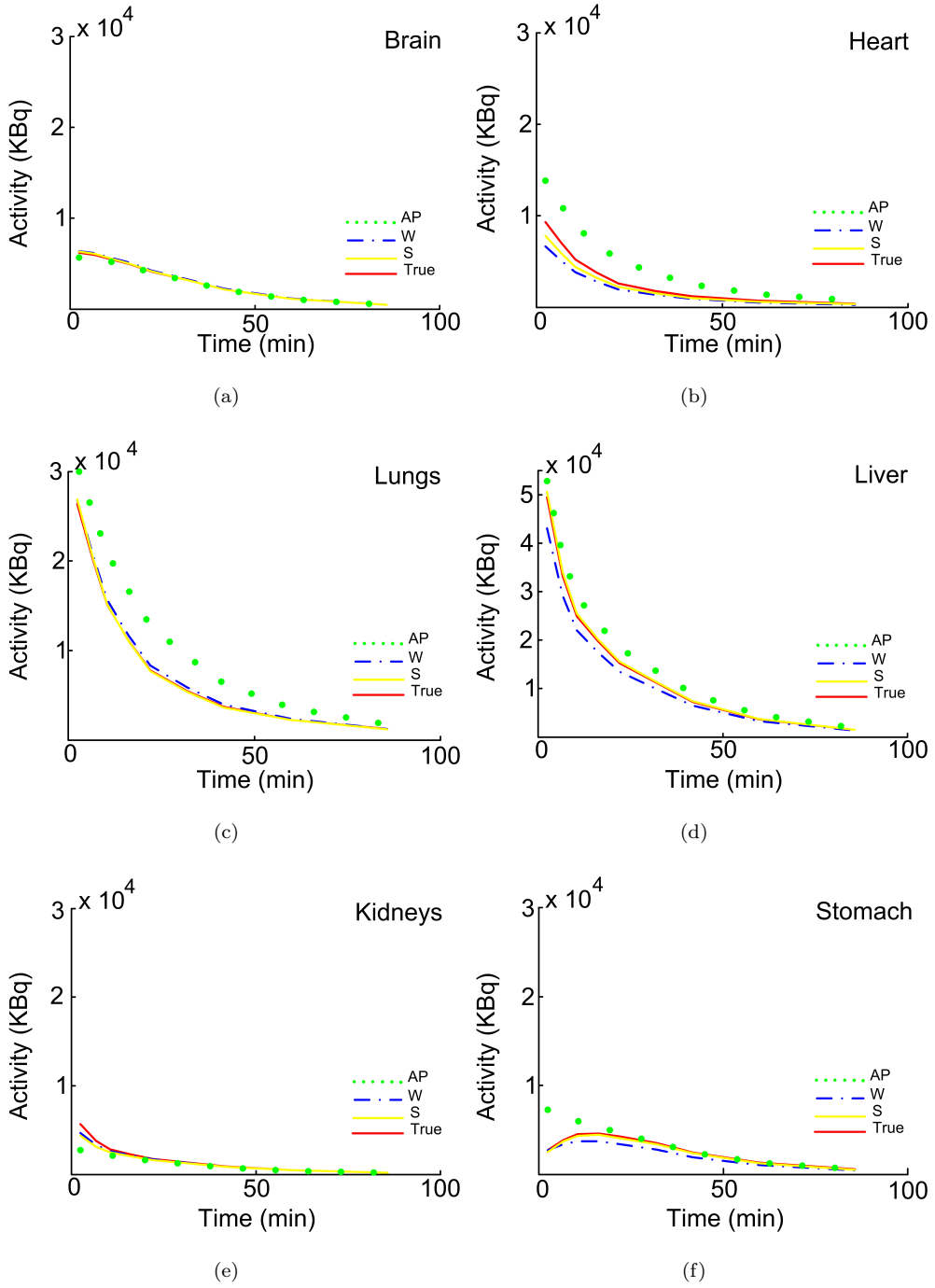

FIGURE 4.12: Simulated and true time-activity curves using different ROI delineation methods (AP antero-posterior, S subsamples, W whole body) of some representative organs for [^{11}C]GSK931145. Images reconstructed using FBP2D and ISC.

A similar pattern was found in the time-integrated activity coefficient and absorbed dose where S and W were comparable to the true values, and AP methods showed differing results depending on how the ROIs were drawn due to overlapping between organs (Figs. 4.14, 4.15 and 4.16). As expected, higher TACs lead to higher ($\tilde{a}(r_s, T_D)$) and dose estimations.

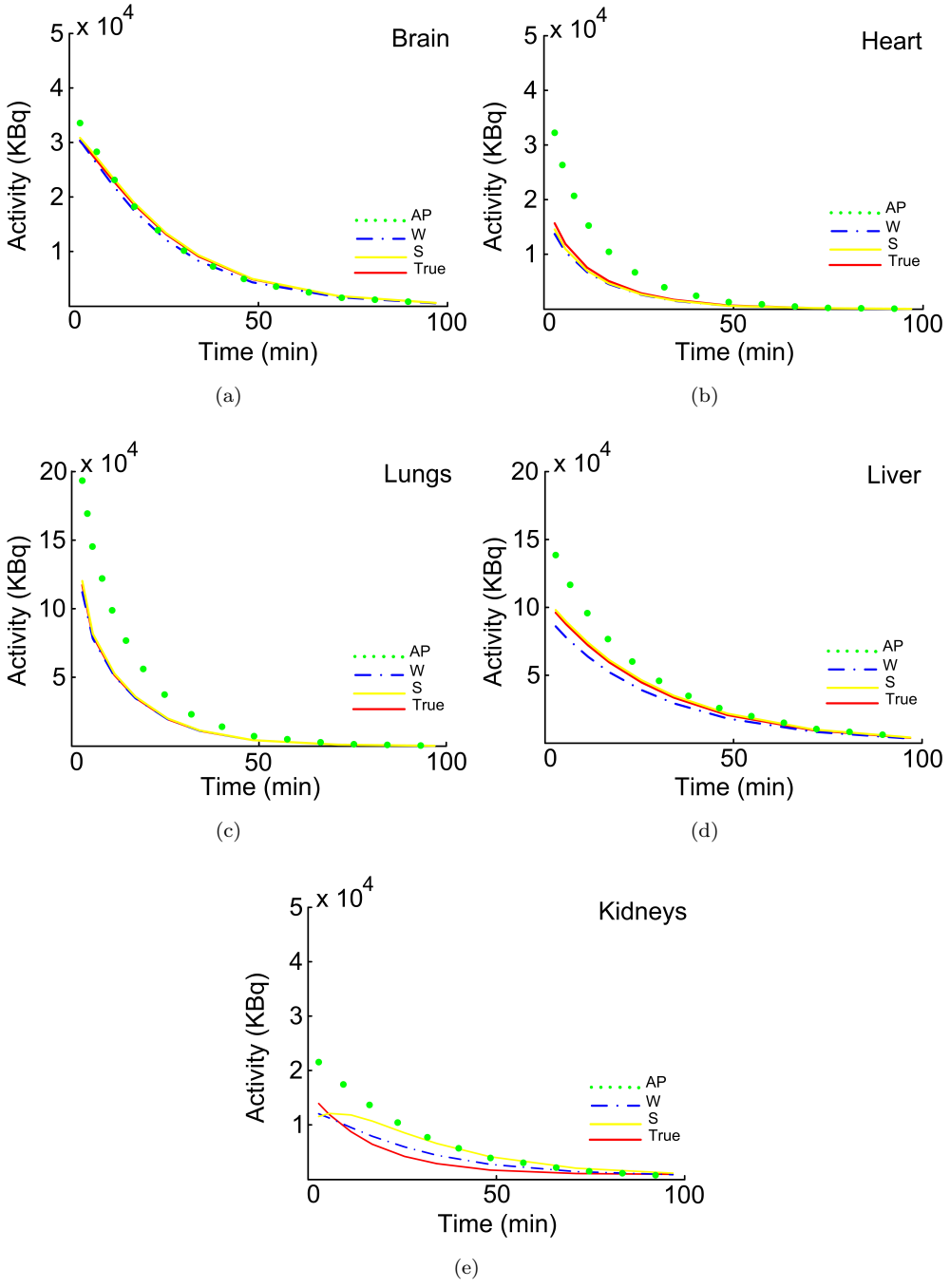

FIGURE 4.13: Simulated and true time-activity curves using different ROI delineation methods (AP antero-posterior, S subsamples, W whole body) of some representative organs for [^{11}C]raclopride. Images reconstructed using FBP2D and ISC.

For both simulated radioligands, effective dose estimates using S and W methods showed close agreement with true values ([^{11}C]GSK931145 4.8 $\mu Sv/MBq$ (true), 4.6 $\mu Sv/MBq$ (W), 4.5 $\pm$ 0.5 $\mu Sv/MBq$ (S) for m ales and 5.8 $\mu Sv/MBq$ (true), 5.6 $\mu Sv/MBq$ (W), 5.6 $\pm$ 0.6 $\mu Sv/MBq$ (S) for females; [^{11}C]raclopride 6.0 $\mu Sv/MBq$ (true), 5.8 $\mu Sv/MBq$ (W), 5.4 $\pm$ 0.2 $\mu Sv/MBq$ (S) for males and 7.8 $\mu Sv/MBq$ (true), 7.4 $\mu Sv/MBq$ (W), 7.2 $\pm$ 0.2 $\mu Sv/MBq$ (S) for females) (Tables 4.5 and 4.6). For

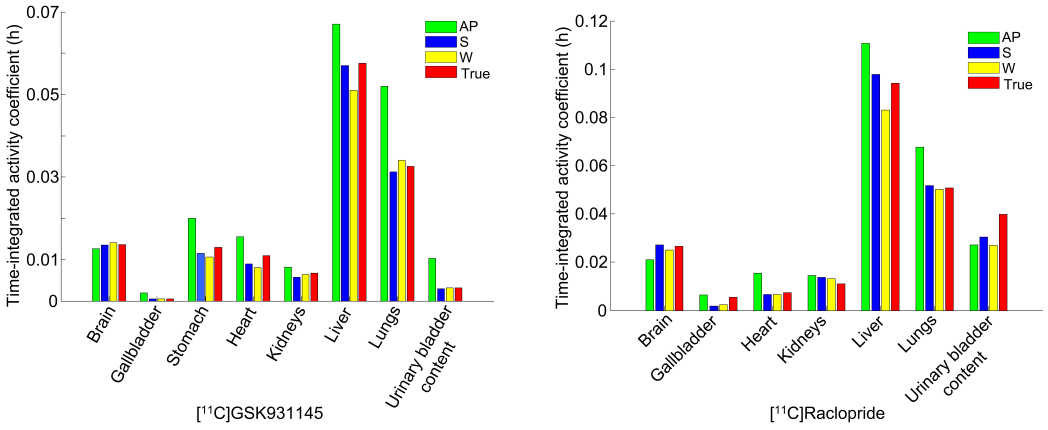

FIGURE 4.14: Time-integrated activity coefficient ($\tilde{a}(r_s, T_D)$) for (a) [^{11}C]GSK931145 and (b) [^{11}C]raclopride distributions. ($\tilde{a}(r_s, T_D)$) calculated from 2D planar images (AP ROI method applied) and tomographic (3D) images (S and W ROI methods applied).

[^{11}C]GSK931145 radioligand, ROIs drawn on AP compressed images provided higher effective dose estimates than true values and the S and W ROI delineation methods (4.8 $\mu Sv/MBq$ (true), 6.7 ± 0.5 $\mu Sv/MBq$ (AP) for males and 5.8 $\mu Sv/MBq$ (true), 8.3 ± 0.6 $\mu Sv/MBq$ (AP) for females). For [^{11}C]raclopride, true effective dose was higher than the similar values provided by the three delineation methods (6.0 $\mu Sv/MBq$ (true), 6.1 ± 0.3 $\mu Sv/MBq$ (AP) for males and 7.8 $\mu Sv/MBq$ (true), 7.8 ± 0.4 $\mu Sv/MBq$ (AP) for females). The organs with the highest tissue-weighted (w_t were taken from ICRP Publication 60) absorbed dose and ED were the lungs and the liver. The estimations obtained with the S and W methods showed good agreement with the true values (Tables 4.5 and 4.6). The AP method provided higher values in ED and AD in the lungs and liver in comparison with the true value (Tables 4.5 and 4.6). Considering a real situation including errors on organ volume estimates, errors up to $\pm 20\%$ of the organ size when using the S method for [^{11}C]raclopride lead to errors in the ED of up to $\pm 10\%$ (Fig. 4.17). Men and women showed the same pattern. Nevertheless, women's dose estimations were on average 22% and 29% higher than men's results for [^{11}C]GSK931145 and [^{11}C]raclopride, respectively. These percentages are consistents with results of previous studies [99, 100].

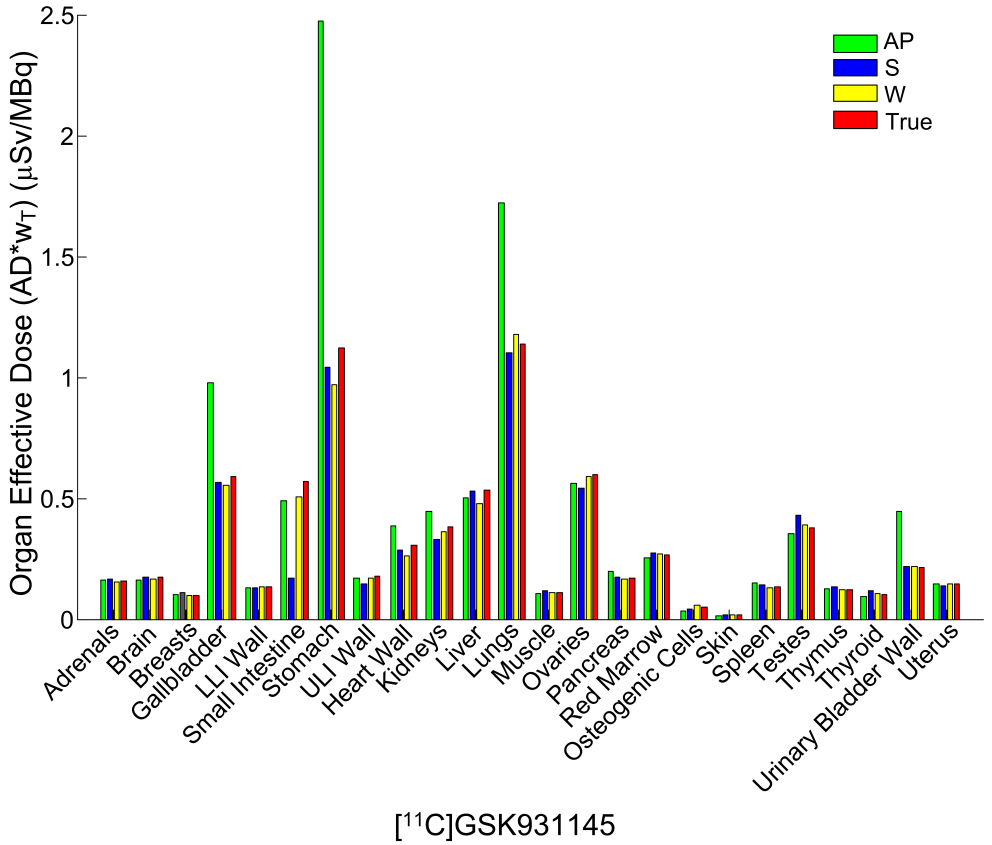

FIGURE 4.15: Comparison of the organ-effective doses ($\mu Sv/MBq$) using different ROI delineation methods (AP, S, and W) for [^{11}C]GSK931145 distribution.

TABLE 4.5: Radiation-absorbed dose (AD) and effective dose (ED) estimates using different ROI delineation methods (AP, S, and W)for [^{11}C]GSK931145 biodistribution.

	[^{11}C]GSK931145			
	True	AP	S	W
Liver AD (uSv/MBq):				
Male	10.7	10.0 ± 1.8	10.6 ± 0.2	9.6
Female	14.1	13.2 ± 2.4	14.0 ± 0.3	12.7
Lung AD (uSv/MBq):				
Male	9.5	14.4 ± 1.8	9.2 ± 1.7	9.8
Female	12.0	18.2 ± 2.3	11.6 ± 2.1	12.4
Stomach AD (uSv/MBq):				
Male	9.4	20.6 ± 4.9	8.7 ± 0.2	8.1
Female	11.0	24.3 ± 5.8	10.2 ± 0.2	9.5
ED (uSv/MBq):				
Male	4.8	6.7 ± 0.5	4.5 ± 0.5	4.6
Female	5.8	8.3 ± 0.6	5.6 ± 0.6	5.6

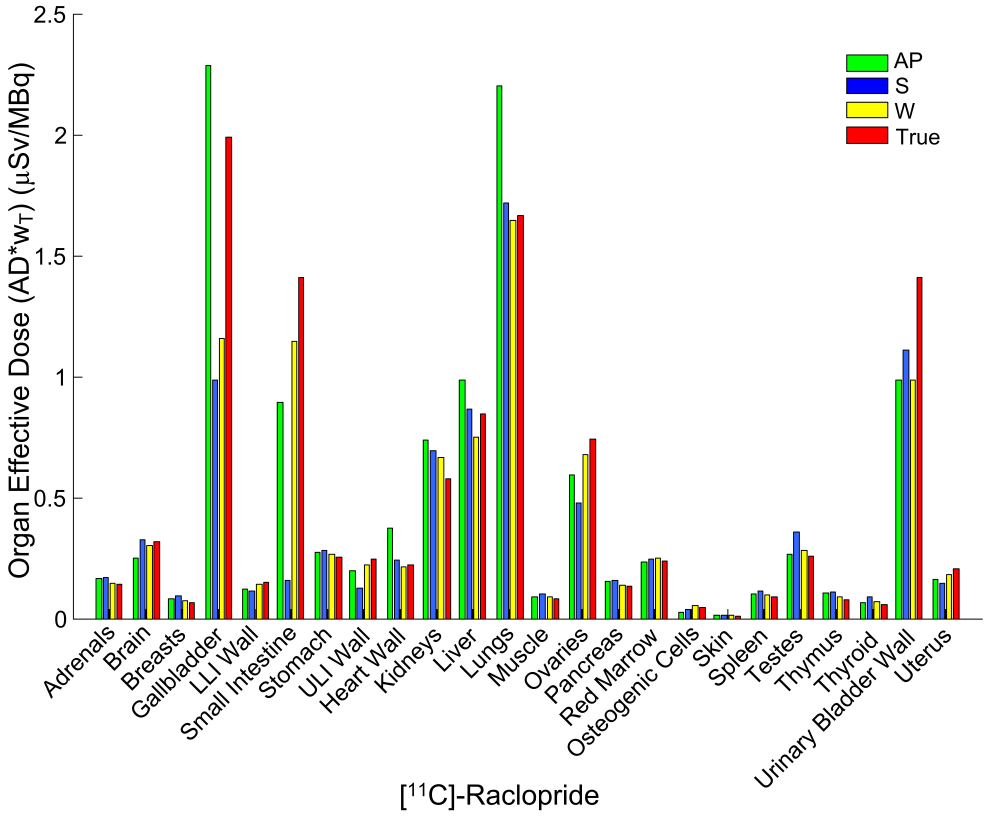

FIGURE 4.16: Comparison of the organ-effective doses ($\mu Sv/MBq$) using different ROI delineation methods (AP, S, and W) for [^{11}C]raclopride distribution.

TABLE 4.6: Radiation-absorbed dose (AD) and effective dose (ED) estimates using different ROI delineation methods (AP, S, and W) for [^{11}C]Raclopride.

	[^{11}C]Raclopride			
	True	AP	S	W
Liver AD (uSv/MBq):				
Male	16.9	19.7 ± 0.9	17.3 ± 0.1	15.0
Female	22.3	26.0 ± 1.2	22.9 ± 0.1	19.8
Lung AD (uSv/MBq):				
Male	13.9	18.3 ± 1.9	14.3 ± 0.1	13.7
Female	17.5	23.1 ± 2.4	18.1 ± 0.1	17.3
Stomach AD (uSv/MBq):				
Male	2.1	2.3 ± 0.1	2.4 ± 0.1	2.2
Female	2.7	2.9 ± 0.1	2.8 ± 0.1	2.8
ED (uSv/MBq):				
Male	6.0	6.1 ± 0.3	5.4 ± 0.2	5.8
Female	7.8	7.8 ± 0.4	7.2 ± 0.2	5.8

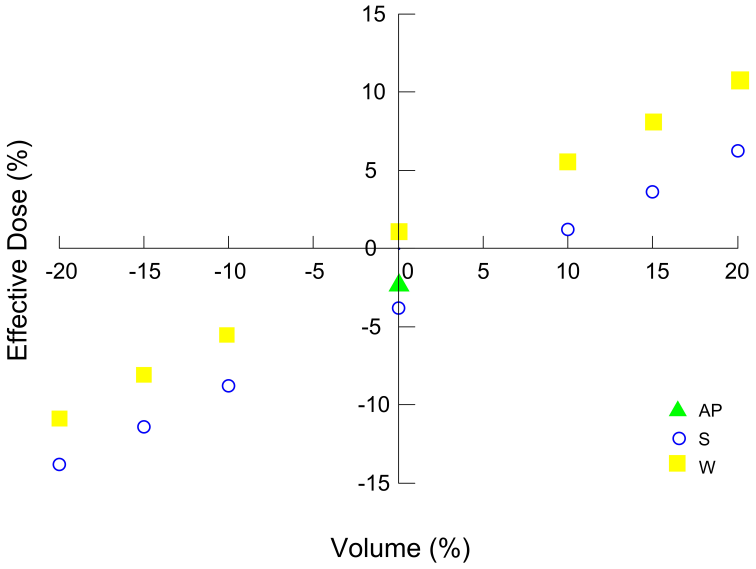

FIGURE 4.17: Percentage difference of effective dose from the whole-organ method for [^{11}C]raclopride distribution using different organ volumes.

4.6 Discussion

4.6.1 Reconstruction

OSEM provided closer ED estimates to the simulated ones. However, the influence of reconstruction algorithms was minimal, due to similar quantitative accuracy was found with either FBP (2D and 3D) or OSEM reconstruction methods. This can be explained by the fact that in dosimetry studies, not only is the relative contrast between structures important but also the global activity distributed on organs.

An activity calibration method for each reconstruction algorithm is an important step to obtain images providing accurate global activity estimates. Additionally, the absorbed dose received by an organ has a contribution from distant organs; thus, in terms of calibration of the global mean activity, differences in contrast have a lower effect. Furthermore, large ROIs encompassing complete organs used in dosimetry contribute to reduce the impact that the partial volume effect may have on the images [101]. A similar argument could be used for the lack of differences found when using full scatter correction and single scatter correction. Full scatter correction is, in theory, more accurate than single scatter correction. However, the calibrated activity used for dosimetry estimations provides an accurate mean global distribution which leads to accurate ED estimates.

4.6.2 ROI Delineation Comparison

In this study, 2D planar image analyses (AP) and two 3D ROI delineation methods (S and W) for obtaining time-activity curves were compared using PET simulated images as the gold standard. The differences in the ED obtained were small between 3D methods, as it would be expected when taking into account organs of the same volume. However, there is a slight underestimation of the ED in comparison with the true value. It was observed that doses estimations were higher for females than males; this is due to the smaller body and organ sizes than those of males. Additionally, female gonads are inside the body instead of outside, receiving a higher radiation dose given the proximity to several organs, such as liver and kidneys, which are often important source organs. For [^{11}C]GSK931145 radioligand, with intestinal route of excretion, planar methods overestimate due to a combination of delineating, overlapping between ROIs (mainly for lungs and stomach) and the background activity in the planar projection view. The fact that these differences were not found for [^{11}C]raclopride radioligand could be attributed to the route of excretion, since the involved organs reduce the impact of errors related to delineation and overlapping on the effective dose. The same behaviour would be expected for radioligands with the same biodistribution and route of excretion. The mean execution time for the delineation of whole-organ ROI procedure compared to 2D delineation methods (subsamples and AP) was 6 h vs 15 min per subject, respectively. 3D method was considerably more time-consuming since the ROIs were drawn manually on the whole set of CT transverse slices. The time spent tracing ROIs by using subsamples of the organ or delineating ROIs on 2D compressed images was similar (15 min per subject). In 3D method, ROIs were created by manually drawing the regions on each 2D slice of a 3D volume. In the AP method, each ROI was drawn on the AP compressed image (one single slice). For the subsampled organ method, spherical ROIs were selected using a graphical interface and applied on 3D images. Each ROI was restricted to a sphere with a fixed radius around the specified coordinates selected by the operator for each organ.

It was observed that ED estimations were sensitive to whichever delineation ROI method was applied. The difficulty lies in delineating the border of each region with precision, whether excluding or not blurred borders in the forming ROIs. Thus, slight differences in boundary delineation have a great effect on dose estimations. However, in diagnostic applications, using a phantom instead of a patient-specific model seems to be acceptable.

4.7 Conclusions

Among the three methods compared to draw ROIs, the subsampled organ method showed the best balance between quantitative accuracy.

Similar quantitative accuracy was found either FBP (2D and 3D) or OSEM reconstruction methods. In the same way, the full scatter correction and single scatter correction no presented differences in terms of quantitative accuracy.

Radioligands with an intestinal route of excretion, such as [^{11}C]GSK931145 overestimate doses in planar images. The involved organs such as stomach and lungs lead to a greater errors related to delineation and overlapping on the ED.

Chapter 5

Inter- and Intra-Operator Variability on Internal Dosimetry Using PET

Considering the issue brought up in section 4.4, in this chapter we investigated the impact of ROI delineation methods on precision in the calculation of internal dosimetry estimates. Inter- and intra-operator variability was evaluated using a previous study undergone at Molecular Imaging Centre (CRC-CIM) in the Barcelona Biomedical Research Park (PRBB). PET/CT images were given up by the pharmaceutical company GlaxoSmithKline (GSK).

5.1 Introduction

One of the most difficult issues facing PET-based in diagnosis, but above all in therapeutic applications is the accurate delineation of target regions from typical blurred and noisy functional images. Image segmentation is defined as the process of classifying the voxels of an image into a set of distinct classes. Medical image segmentation has been identified as the key problem of medical image analysis [35, 102]. The difficulty in PET image segmentation is compounded by the low spatial resolution and high noise characteristics of PET images.

Several segmentation methods have been proposed the last decades [35, 103, 104], there is a large variability in terms of computational complexity and amount of user interaction required by the various image segmentation techniques. Due to the difficulties and known limitations of these techniques, manual delineation of regions of interest

performed by experts is still the most widely used technique [104, 105]. However, it suffers from many drawbacks; manual delineation is time consuming, labour intensive and operator-dependent.

In the major of internal dosimetry studies manual delineation is used [106–108], the lack of reliable methods to perform automated organ segmentation makes internal dosimetry estimates operator dependent. To the best of our knowledge, the impact of ROI delineation methods on the inter- and intra-operator variability in internal dosimetry estimates has not been reported to date.

5.2 Clinical Human Data

Inter- and intra-operator variability of the different methods to obtain dosimetry estimates was evaluated using clinical data acquired in an earlier study [5]. In such study, eight healthy human volunteers (4 M/4 F) underwent whole-body PET/CT scans on a General Electric Discovery ST scanner which used a 3D mode protocol. Their demographic data are shown in Table 5.1. Before tracer injection and emission scanning, a transmission scan was acquired for each bed position (80 mA,120 keV) for subsequent attenuation correction and reconstructed to a $512 \times 512 \times 593$ grid of $0.98 \times 0.98 \times 1.80\ mm^3$ voxel size. Whole-body emission scans were performed following the intravenous administration of [^{11}C]GSK931145 radioligand. The total scanning time was approximately 110 min (2×15, 2×30, 2×60, 1×120, 1×180 and 1×240 s for each bed) with six to seven overlapping bed positions beginning at the head and continuing to the middle of the thigh. PET data were reconstructed using an OSEM reconstruction algorithm which included correction for attenuation, scatter (single scatter simulation method [109]), randoms, and dead time to generate a matrix of $128 \times 128 \times 327$ and $3.91 \times 3.91 \times 3.27\ mm^3$ voxel size. Whole-body PET images of a healthy human subject over scanning time are shown in figure 5.1. For activity quantification in PET planar images and according to previous works, there were no background susbstraction. In such studies, it was demonstrated that analysis of compressed planar images were comparable to tomographic images, but with a slight overestimation (conservative calculation) [5, 80, 81, 83].

A homogeneous water-filled phantom with a known concentration of F-18 was used to determine the cross-calibration factor between PET and the dose calibrator. This factor was applied to the PET data to generate quantitative images.

TABLE 5.1: Demographics data for [^{11}C]GSK931145 human study [5].

Subject ♯	Gender	Age (year)	Height (m)	Weight (kg)	BMI (kg/m^2)
1	M	19	1.83	70	21
2	M	23	1.81	85	26
3	M	23	1.79	75	23
4	M	26	1.80	80	25
5	F	49	1.64	78	29
6	F	46	1.56	59	24
7	F	50	1.60	81	32
8	F	62	1.64	60	25
MEAN ± SD		37.25 ± 16.28	1.70 ± 0.12	73.5 ± 9.9	25.6 ± 3.3

BMI Body mass index

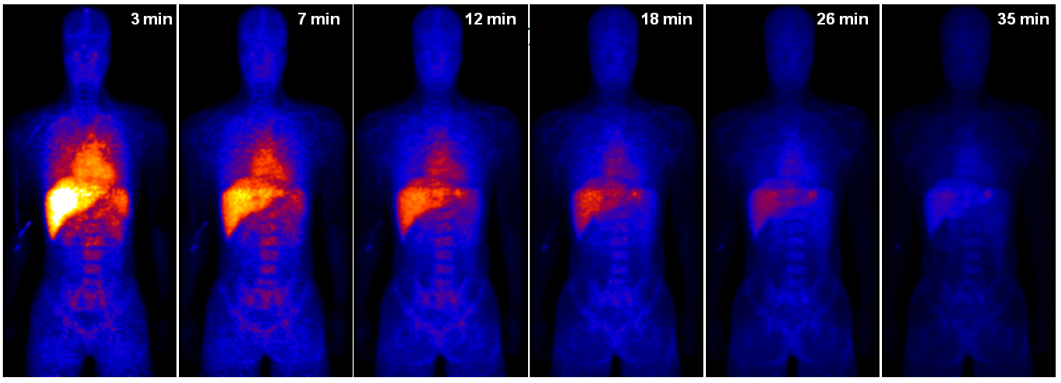

FIGURE 5.1: Whole-body PET images of a healthy human subject after injection of [^{11}C]GSK931145.

5.3 Assessment of Inter- and Intra- Operator Variability

The three delineation procedures which are detailed in subsection 4.4.1 were used by six (for AP and S methods) and five (for W method) independent operators on all subjects to examine inter-operator variability. Additionally, two of the operators carried out the procedures twice to examine intraoperator variability. Regarding subsample method, ROIs were scaled according to the organ volumes derived from adult (male and female) numerical phantoms [47]. Figure 5.2 shows the three delineation methods applied on a whole-body PET images of a healthy human subject. Figure 5.3 exposes the PET images of the eight subjects and the three ROI delineation method (whole-organ, subsamples and anterio-posterior) tested on them. Their size complexity can be observed.

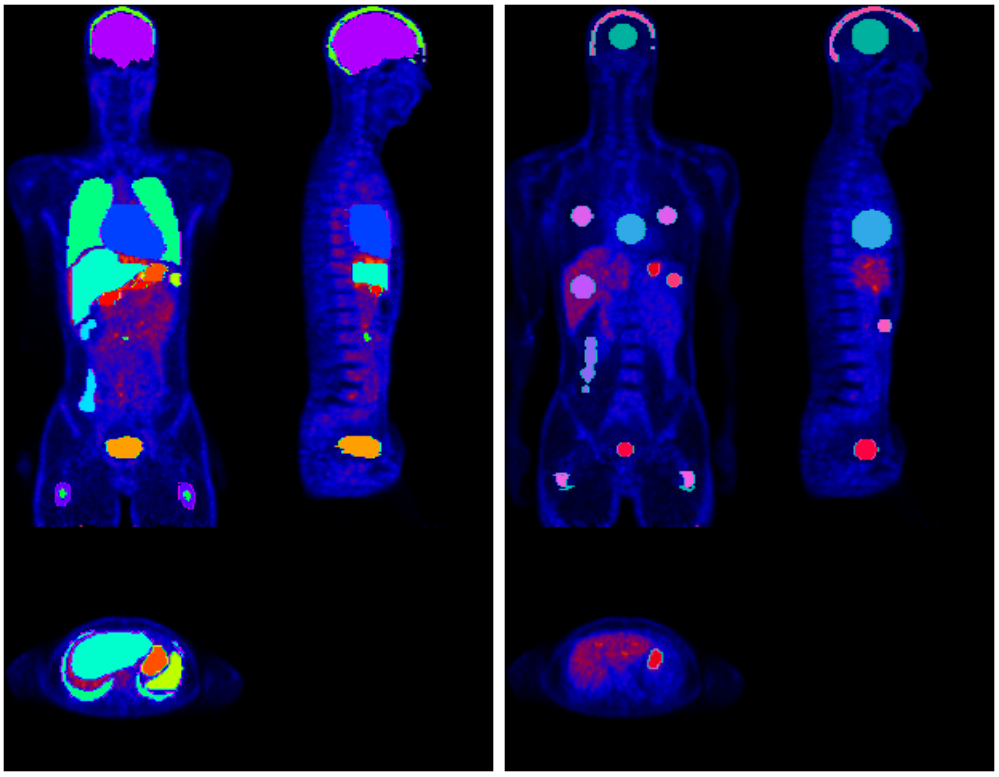

(a) (b)

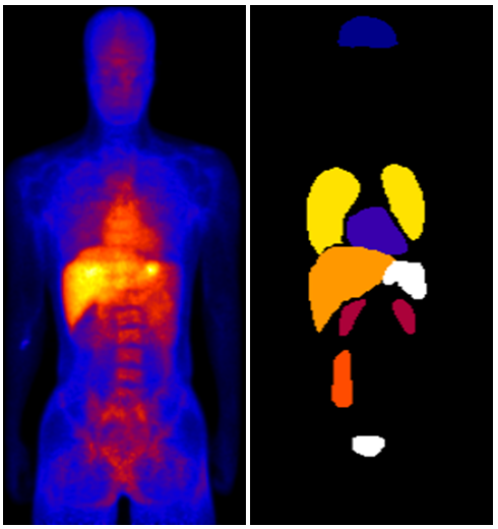

(c)

FIGURE 5.2: ROI delineation methods tested on a whole-body PET images of a healthy human suject: (a) 3D volume covering the whole-organ, (b) 3D subsamples of the organs and (c) antero-posterior projections.

The intra- and inter-operator variability in effective doses (EDs) was calculated as the mean variability of the standard deviation of the ED calculated by all operators (eqs.5.1 and 5.3).

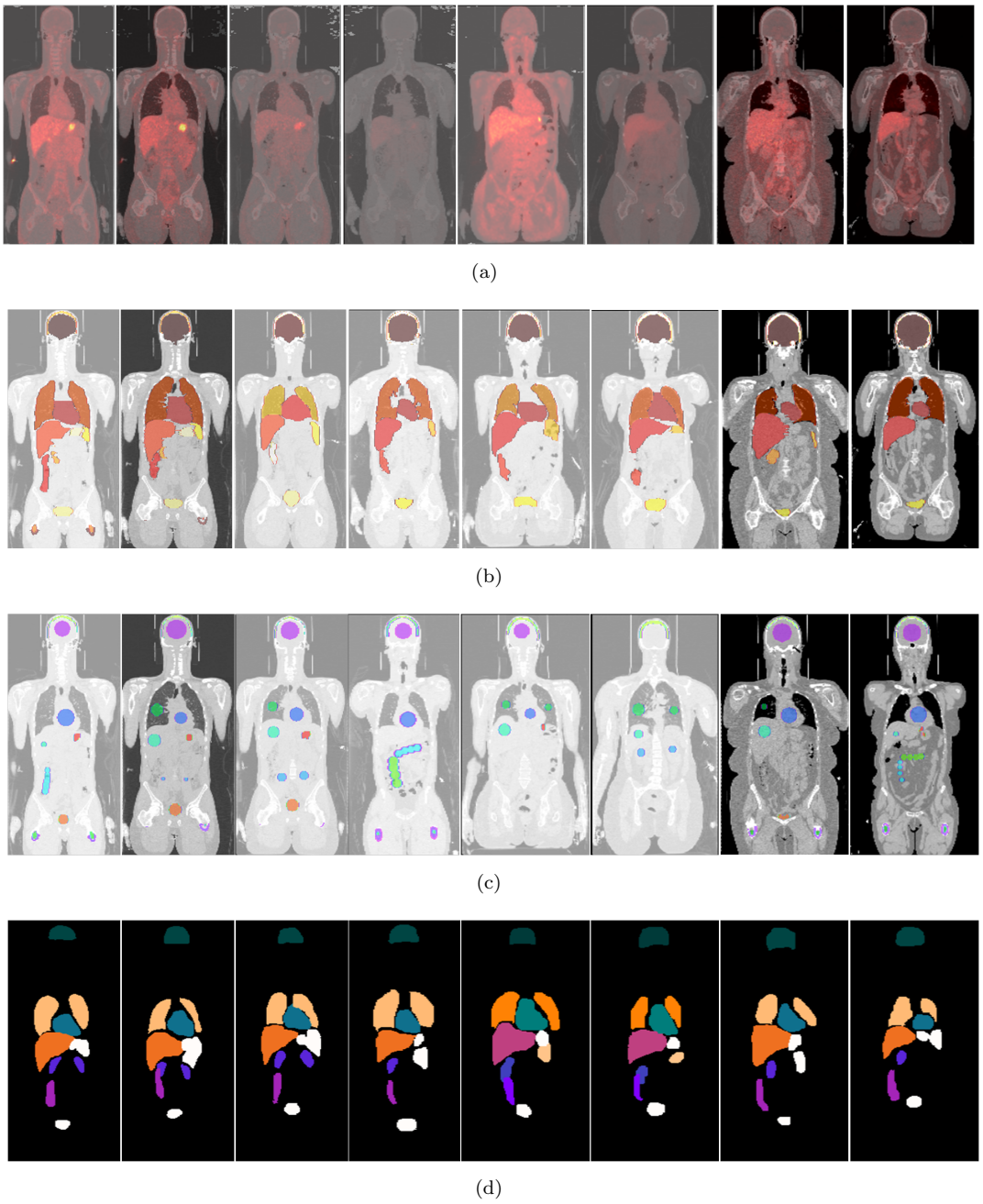

(a)

(b)

(c)

(d)

FIGURE 5.3: Coronal view of eight healthy human subjects: (a) CT images overlaid with whole-body PET images, (b) whole-organ ROI, (c) subsamples of the organs and (d) ROI delineated on antero-posterior projections, applied by one of the operators.

Intra-subject variability was estimated as:

$$V_{intra} = \frac{100}{N} \sum_{i=1}^{N} \frac{|ED_i^1 - ED_i^2|}{ED_i^{mean}}, \tag{5.1}$$

where ED_i^1 and ED_i^2 are the ED values for both ROI delineations carried out by the same operator, N is the number of subjects and ED_i^{mean} was calculated as:

$$ED_i^{mean} = \frac{ED_i^1 + ED_i^2}{2}, \tag{5.2}$$

Inter-subject variability was estimated as:

$$V_{inter} = \frac{100}{N} \sum_{i=1}^{N} \frac{|ED_i - ED^{mean}|}{ED^{mean}}, \tag{5.3}$$

where ED_i is the mean ED value, N is the number of subjects and ED^{mean} was calculated as:

$$ED^{mean} = \frac{1}{N} \sum_{i=1}^{N} ED_i, \tag{5.4}$$

Estimation of the uncertainty of the variability for the three delineation methods was provided. Similar calculations were done to estimate the percentage of variability of the absorbed doses (ADs). Standard uncertainty was estimated as:

$$u = \frac{\sigma}{\sqrt{N}}, \tag{5.5}$$

where σ is the standard desviation and N is the number of subjects.

Finally, human data were analyzed using two-way analysis of variance (ANOVA) to test differences in the ED values using operator and methods of ROI delineation as factors. When the overall F statistic was significant, post hoc comparison of ROI methods using the Scheffé approach was performed. A probability threshold of 0.05 was chosen as the significance level. Statistical analysis system (SAS) 9.2 for Windows was used for statistical analysis.

5.4 Results

Variance analysis presented significant differences in mean dosimetry estimates depending on the delineation method ($p < 0.001$). Post hoc analysis showed significant differences in the effective dose between the AP method and the other two methods studied (S

and W). However, there were no differences between S and W. No significant differences were also found between the effective dose measured by different operators.

The three delineation methods showed the same intra-operator variability in the effective ED estimates. AP method showed higher intra-operator variability in the AD estimates than the S and W methods (Tables 5.2 and 5.3). AP also showed higher inter-operator variability in the ED estimates and AD estimates than the S and W methods (Tables 5.2 and 5.3), except in the case of the gallbladder and the small intestine, very close organs and difficult to delineate. Figure 5.4 shows the subject with the major inter-operator variability, it corresponds to AP delineation method. The ROIs of the two independent operators that estimated the maximum and minimum ED values were shown. Inter-operator variability was slightly reduced in the case that both operators delineated ROIs according to same criteria.

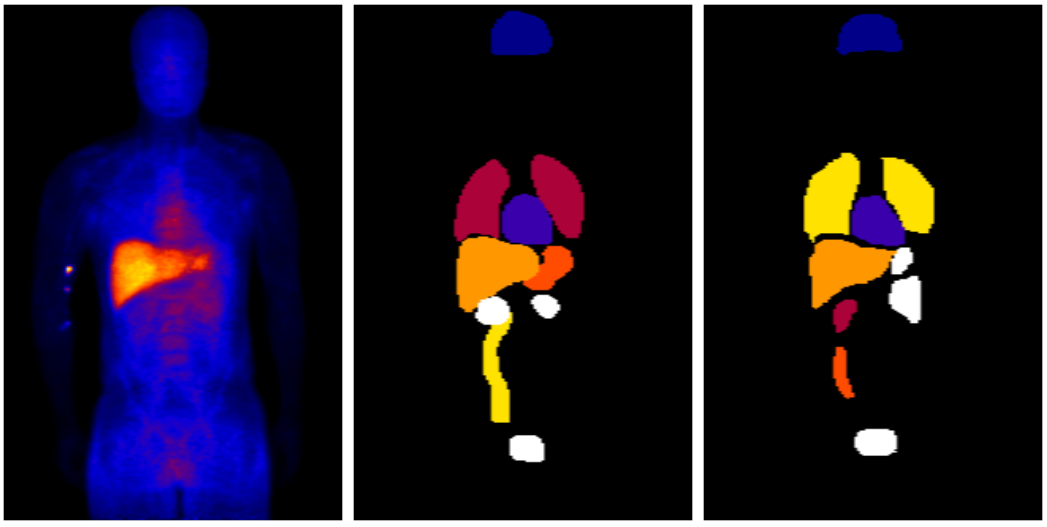

(a) (b) (c)

FIGURE 5.4: Subject to examine inter-operator variability using AP ROI delineation procedure. (a) Whole-body PET planar image, (b) ROIs drawn by operator 1 that estimated the maximum ED value and (c) ROIs drawn by operator 4 that estimated the minimum ED value.

TABLE 5.2: Inter- and intra-operator percentage variability.

	Method	Variability (intra-operator)	Variability (inter-operator)
ED (μSv/MBq)	AP	$4 \pm 1\%$	$11 \pm 1\%$
	S	$4 \pm 1\%$	$4 \pm 1\%$
	W	$4 \pm 1\%$	$5 \pm 1\%$

TABLE 5.3: Inter- and intra-operator percentage variability.

Organ	Method	Variability (intra-operator)	Variability (inter-operator) AD (μGy)	Variability (inter-operator) AD x $W_T{}^a$ (μGy)
Brain	AP	$15.3 \pm 4.7\%$	$19.1 \pm 2.6\%$	0.10%
(W_T=0.005)	S	$3.3 \pm 0.9\%$	$5.9 \pm 2.0\%$	0.03%
	W	$6.6 \pm 2.6\%$	$6.1 \pm 2.1\%$	0.03%
Gallbladder	AP	$3.1 \pm 1.2\%$	$3.2 \pm 0.8\%$	0.16%
(W_T=0.05)	S	$7.8 \pm 3.7\%$	$25.4 \pm 3.8\%$	1.27%
	W	$5.0 \pm 1.2\%$	$5.0 \pm 0.8\%$	0.25%
Small Intestine	AP	$2.2 \pm 0.7\%$	$2.9 \pm 0.4\%$	0.01%
(W_T=0.005)	S	$7.1 \pm 2.5\%$	$39.7 \pm 2.8\%$	0.20%
	W	$20.6 \pm 4.4\%$	$19.5 \pm 3.3\%$	0.10%
Liver	AP	$11.5 \pm 5.7\%$	$12.1 \pm 3.2\%$	0.61%
(W_T=0.05)	S	$8.3 \pm 5.0\%$	$8.0 \pm 2.6\%$	0.40%
	W	$3.5 \pm 0.6\%$	$4.2 \pm 0.7\%$	0.21%
Lungs	AP	$13.4 \pm 5.1\%$	$17.6 \pm 2.6\%$	2.11%
(W_T=0.12)	S	$15.2 \pm 9.2\%$	$15.3 \pm 7.3\%$	1.83%
	W	$11.0 \pm 5.6\%$	$11.9 \pm 4.6\%$	1.43%
Stomach	AP	$14.2 \pm 4.6\%$	$30.6 \pm 1.8\%$	3.68%
(W_T=0.12)	S	$11.3 \pm 2.7\%$	$15.3 \pm 3.3\%$	1.84%
	W	$7.5 \pm 2.2\%$	$8.4 \pm 2.1\%$	1.01%
Heart	AP	$9.9 \pm 2.9\%$	$18.9 \pm 1.9\%$	0.95%
(W_T=0.05)	S	$4.6 \pm 2.7\%$	$6.8 \pm 2.0\%$	0.34%
	W	$3.1 \pm 0.8\%$	$4.4 \pm 0.9\%$	0.22%
Kidneys	AP	$37.7 \pm 7.4\%$	$32.7 \pm 4.7\%$	0.16%
(W_T=0.005)	S	$4.3 \pm 1.5\%$	$15.0 \pm 5.8\%$	0.08%
	W	$8.4 \pm 2.9\%$	$11.3 \pm 3.3\%$	0.06%
Urinary Bladder	AP	$17.1 \pm 4.5\%$	$28.2 \pm 3.0\%$	1.41%
(W_T=0.05)	S	$4.9 \pm 1.3\%$	$8.9 \pm 2.9\%$	0.40%
	W	$4.3 \pm 1.4\%$	$4.3 \pm 1.2\%$	0.20%

[a]Tissue weighting factor

5.5 Discussion

The AP method showed the highest inter-operator variability, in particular, the highest organ doses were obtained when including the blurred borders, and the corresponding ED were overestimated.

Inter-operator variability results showed higher reproducibility of the 3D methods in comparison with 2D methods. The S method was substantially less time consuming and showed comparable inter- and intra-operator variability compared with the W method and may provide the best option in the balance between analysis time, accuracy, and reproducibility. Nevertheless, care should be taken when using the S method since errors in the organ volume estimation may have an impact on the effective dose estimates [110,111]. This is the case of subjects that are quite different from the phantom used by

Olinda/EXM. In these cases, whole-organ ROIs would be desirable. The higher values provided from the 2D approach, as regards quantifying the human radiation burden, represent more conservative dose estimates. Thus, some researchers have suggested that the 2D planar method appear to be a reasonable strategy for assessing the radiation risk of most internally administered radiopharmaceuticals. Nevertheless, it does not appear to be the optimal method for individual dosimetry estimates of ligands due to its high inter- and intra-operator variability.

5.6 Conclusions

Among the three methods compared to draw ROIs, the subsampled organ method showed the best balance between quantitative accuracy, inter- and intra-subject variability and practical implementation.

Whole-organ ROI method was the best option in cases where patients' anatomy are quite different from the reference phantom used by OLINDA/EXM.

Chapter 6

Implementation of patient-individualized model for internal dosimetry

This chapter describes the development of a 3D image-based dosimetry technique using PENELOPE/penEasy Monte Carlo code. Dedicated routines in MATLAB environment were developed to perform patient-specific dosimetry in nuclear medicine patients' who undergone PET/CT or SPECT/CT images. It is also described the application of this technique to PET simulated images where the organ activity distribution was known.

6.1 Introduction

In nuclear medicine, radionuclides are used in variety of diagnostic and therapeutic procedures. In the development of new radiopharmaceuticals internal dosimetry is essential to evaluate the risk and benefit of any methods. In diagnostic applications relatively small amounts of radioactivity are used in comparison to therapeutic procedures. The absorbed dose from internally distributed radioactivity used in diagnostic procedures is usually estimated using standardized models based on reference individuals and not specific patients. Model based approach may be acceptable for diagnostic radiopharmaceuticals as it was seen in chapter 4, taking into account that all input data employed in the calculation has some associated uncertainty. The dose estimated will include the inherent uncertainty from the input data as well as related to the application of standardized models of the body to a population of patients who may vary substantially in size, age, and other physical characteristics. In therapeutic applications, however,

more attention to accuracy and precision is needed [42]. Typical Targeted Radionuclide Therapy treatments are based on administering a fixed activity per unit body weight approach to all patients. The aim is to deliver sufficient dose to the tumor while limiting toxicity to healthy tissue. If a fixed-activity is employed, patients are almost always given low amounts of the radionuclide in order to avoid harmful effects to normal tissue. So, only a small fraction of patients receive optimal care. Therefore, there is an increasing necessity for developing accurate and precise methods for individualized patient dosimetric estimation [9].

So, it is not surprising that the new European Council Directive 2013/59 [62] mandates dosimetry-based treatment planning for radiopharmaceutical therapies. Article 56 states that 'For all medical exposure of patients for radiotherapeutic [1] purposes, exposures of target volumes shall be individually planned and their delivery appropriately verified.'

Monte Carlo method appears as the most advanced technique for this purpose. Many dosimetry tools capable of voxelized dose calculations have been developed, such as the EGS-based 3D-RD code [112], the OEDIPE tool [113] based on the MCNPX code, software based on the MCNP-4B code [114], the DPM program [115], other tools based on GEANT4 code as VIDA software [116], MCID tool based on MCNP5 [117] and programs based on FLUKA code [118]. This study implement Monte Carlo methodology utilizing the PENELOPE/penEasy MC code with the final goal of estimate individualized internal dosimetry in nuclear medicine patients' undergone PET/CT or SPECT/CT images.

6.2 PENELOPE/penEasy for Monte Carlo Simulations on Nuclear Medicine Images

To perform 3D patient-specific absorbed dose calculation by MC simulation is required: (a) the spatial distribution of tissue density and composition taking into account CT data, (b) cumulated activity at the voxel level as input data, provided by the functional images associated with the information coming from biokinetics studies. The workflow diagram in figure 6.1 shows an overview of the method proposed with key components and inputs. The general idea of the method is to use the acquired hybrid image, from which a series of files will be created specifying the anatomy of the patient and the distribution of the injected radiopharmaceutical. These files are placed as input files of the PENELOPE/penEasy MC code. From the output file we will obtain the patient's

[1] According to the Directive (article 4, definition (81)) 'radiotherapeutic' means pertaining to radiotherapy, including nuclear medicine for therapeutic purposes.

dose distribution map and the subsequent dose image, finally if a dynamic study is provided the total accumulated dose at the organ or voxel level will be estimated. This process is detailed in the next sections.

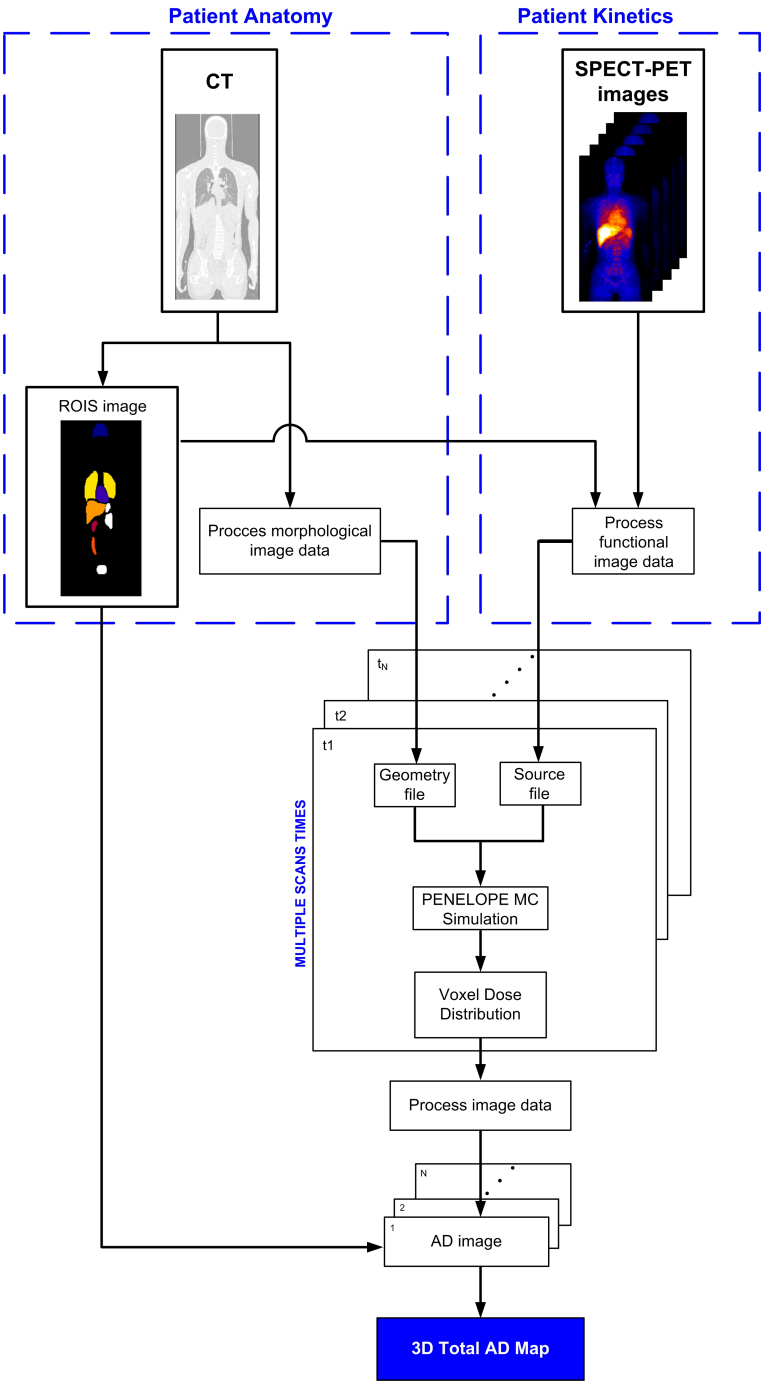

FIGURE 6.1: Workfkow diagram of the method proposed to perform 3D patient-specific absorbed dose calculation.

6.2.1 Input Files Development

6.2.1.1 Geometry and Materials

From CT images can be derived the tissue mass density and the elemental composition, so CT data need to be conveniently interpreted and imported in the code. Routines have been developed in MATLAB (version 7.5, R2007b) environment to convert the CT number (expressed in Hounsfield Unit, HU) into the corresponding material medium (density and composition).

The routine divides the HU range into several intervals and assigns the density and material to each interval based on a specific calibration of the CT scanner. The calibration curve could be configured by the user for their specific CT scanner. The automatic material assignment only assigns biological materials to voxels. Based on their mass density, voxels will be assigned lungs, water, muscle and bone. The list of supported materials with associated density ranges is provided in table 6.1.

TABLE 6.1: Material mass densities in the automatic CT to material conversion.

Material (ICRP 1975)	Density [g/cm^3] Low	High
Lung	0.00	0.59
Water	0.59	1.01
Muscle, skeletal	1.01	1.075
Bone	1.075	6.00

The CT number of any voxel is given as below which is represented in Hounsfield units (HU):

$$CT_{Number}(HU(x,y,z)) = 1000\frac{\mu_t(x,y,z) - \mu_w}{\mu_w} \tag{6.1}$$

Where x, y, z is the coordinate of a voxel, μ_t and μ_w are the linear attenuation coefficients of tissue in a voxel (x, y, z) and water, respectively.

The output CT data is listed in a format readable by the PENELOPE/penEasy MC code (*Geometry file*). The voxelized Geometry file representing the patient are imported in PENELOPE/penEasy by means of a set of routines called penVox with the same size as the CT image. PenVox accepts a list of voxels as input, each one characterized by a material index (which univocally identifies a material in the PENELOPE/penEasy system) and mass density. Figure 6.2 shows a workflow diagram of the steps to follow to obtain the patient's voxelized anatomy.

The morphological image is also employed to delineate organs of interest. It can be used any image tool that is available, for instance MRIcro software [97],that allows the

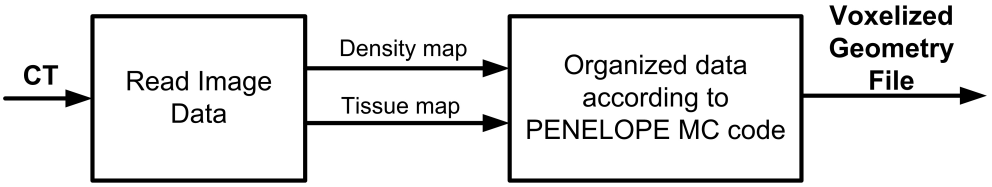

FIGURE 6.2: Workfkow diagram to obtain voxelized Geometry file.

delineation of ROIs and save the output image of the organ as the same format as CT. A new routine was created focused on merge all the output ROI images in a single one identifying each organ with an integer number. Later, the merged ROI image data is listed in a file that relates voxels to the organ to which they belong (*Voxel-ROI file*). A block diagram in figure 6.3 shows this procedure.

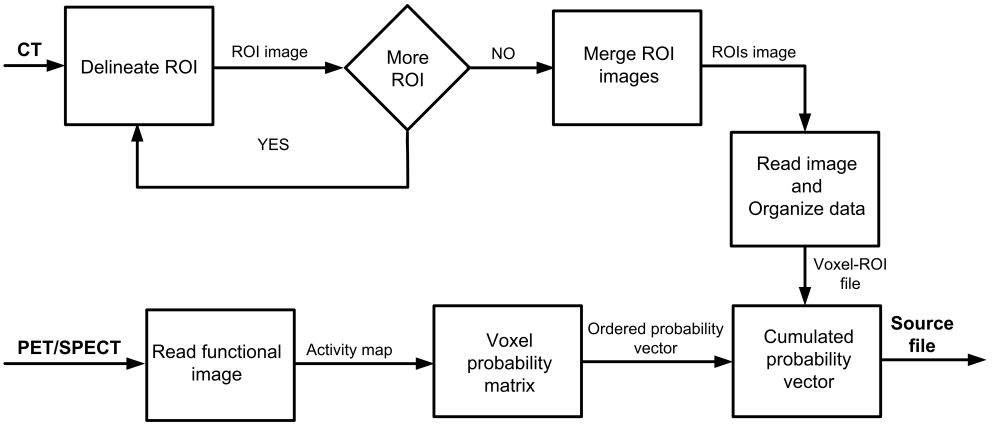

FIGURE 6.3: Workfkow diagram describing the process to obtain radiation source file.

6.2.1.2 Radiation Source

SPECT or PET images are obtained by administering a tracer amount of radiopharmaceutical labelled with a gamma/positron emitting isotope. In order to know the position of the beta particle emitted, functional images are used to estimate the cumulative probability density functions that the positron annihilation (for beta-plus radiopharmaceuticals) with the appropriate electron (from the patients' body) or gamma emission (for beta minus-gamma radiopharmaceuticals) has occurred in each voxel. Dedicated MATLAB routines have been developed in order to convert the SPECT or PET images into a source distribution readable by PENELOPE/PENEASY MC code. The first step of the routines is reading the image and assigne a frequency of each voxel that annihilation occurs, being proportional to its relative counts with respect to the total image counts. Then, probability vector is ordered and cumulative probability vector is created. In a second step of the routines, the *Voxel-ROI file* that has been obtained from the merged ROI image is used to relate voxel index, cumulative probability density

function and organ; these data are listed in a format readable by the MC code. So, this output test file (*Source file*) describes the source model, in this case is the own body of the patient, relating voxel with the ROI who belongs and the probability that the annihilation was produced in that voxel. Figure 6.3 shows detail the detailed process to follow for obtaining the source file.

6.2.2 Monte Carlo Dose Calculations

Simulations were done with the PENELOPE code (version 2011) [67] and penEasy (version 20120601) [68] was used as the main program. More details regarding the code were given in section 3.xx In the penEasy main program is indicated the source model, the geometry model, the tallies (i.e. quantities of interest in the simulation) and variance reduction techniques.

penEasy includes two configurable source models, of which only one can be activated by simulation. The Box Isotropic Gauss Spectrum (BIGS) source model allows defining volumetric sources limited by quadric surfaces, and in the limit case, point sources. Photons, electrons or positrons can be configured with an energy emission spectrum, or with a spectrum defined by a Gaussian function. The second source model is the PSF (Phase-Space File) reads the initial state of the particles to be simulated from an external phase space file, generally created by the main program in a previous simulation.

For our purpose, the PENELOPE/penEasy routine BIGS was modified to import the source file described in 6.2.1.2 and select the voxel for the starting position of each decaying particle. This information is used as PENELOPE/penEasy input file. So, instead of randomly placing events in the source region to create a uniform activity distribution, evens are generated voxel-by-voxel based on the source map derived from functional images. Within each voxel, events are assumed to be uniformly distributed, with randomly selected position and direction vectors.

In the used version of penEasy (v.20120601), the isotope to be simulated is indicated in the input file from the corresponding energy emission spectrum (energy and probability) previously calculated. The corresponding beta spectrum has to be estimated with tools as EDISTR, a computer program to obtain a nuclear decay data base for radiation dosimetry [119]. This software applies the Fermi theory of beta decay [120]. However, there is a testing version of penEasy (in 2017 a non public version), where disintegration schemes of several isotopes are included according to the *Laboratoire National Henri Becquerel (LNHB)*[2]with an specific subroutine called *penNuc*. LNHB, located on

[2] http://www.lnhb.fr/en/

Paris, is a Metrology Laboratory in the field of ionizing radiation. Results from both penEasy versions are detailed in section 6.3.3.

The geometry model file obtained in subsection 6.2.1.1 is indicated in the input file, as well as the considered output file, *voxel dose distribution tally*. Figure 6.4 shows a block diagram of this MC simulation process.

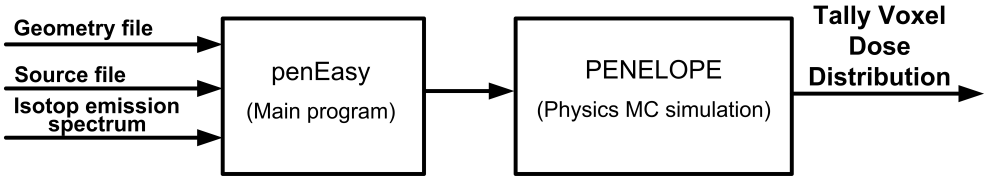

Figure 6.4: Workfkow diagram describing the process to obtain the voxel dose distribution output file.

6.2.3 Absorbed Dose Map

As a result of the simulation with PENELOPE/penEasy MC code, an output file corresponding to a dose distribution map at the voxel level is obtained, together with its statistical uncertainty. New routines in the MATLAB environment were developed in order to process the output file. Firstly, the voxel dose distribution file is read and then, rewritten in a new format to load it into the routine that convert the absorbed dose data file to an image of absorbed dose (figure 6.5). Moreover, this routine allows obtaining information from different parameters of interest, the user can request: cumulative dose in each organ, maximum and minimum voxel values, standard deviation and organ volume (figure 6.6). Sometimes, especially when are used PET/CT techniques for the study of new radioligands, we do not have a static image but we have a dynamic study. In this case, images at different time points after administering the radiopharmaceutical are acquired, so we can obtain ROI quantitative information over time.

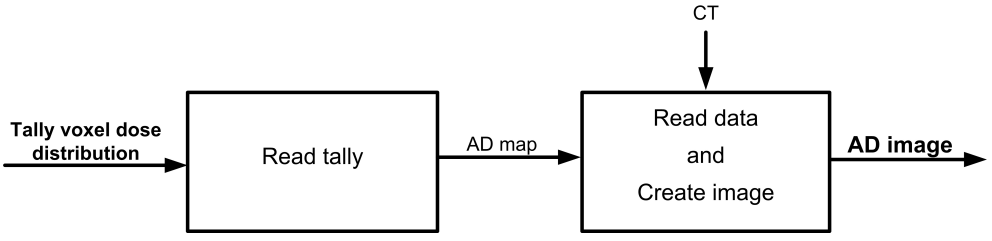

Figure 6.5: Block diagram describing the process to obtain the absorbed dose image.

If a dynamic study is provided, a specific routine allows obtaining the cumulative total absorbed dose due to the radiopharmaceutical in the organs of interest for the

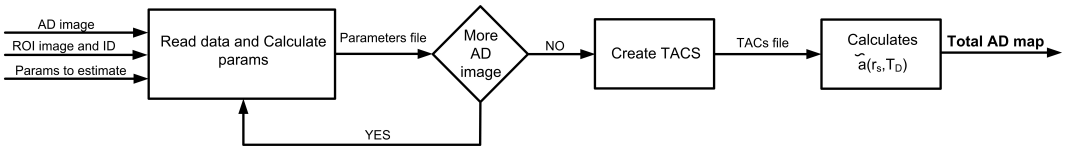

FIGURE 6.6: Workflow diagram describing the process to obtain the total absorbed dose map.

user. We need the dose distribution map for each of the images acquired throughout the dynamic study, that is, for each frame we will apply the process described up to now.

If we graphically represent the absorbed dose values in each time point considered, we find N points corresponding to N frames. So, for each ROI a time-activity curve (TAC) is drawn. In section 1.8 it was described the time-integrated activity coefficient ($\tilde{a}(r_s, T_D)$) over time as a parameter of interest. This coefficient measures the number of disintegrations per unit of activity injected, and it is defined as the area under non decay-corrected time-activity curve divided by the injected activity. For our purpose, the parameter of interest is the cumulated total dose in each organ in a dynamic study, i.e. only the area under the time-activity curve. In order to estimate the total absorbed dose the trapezoidal rule was applied. Area under the time-activity curve for each region was determined by trapezoidal integration plus physical decay for the tail of the curve after the last acquired time point.

Trapezoidal Rule

The trapezoidal rule is a numerical method that approximates the value of a definite integral. We consider the definite integral by the equation:

$$\int_a^b f(x)dx \tag{6.2}$$

where $f(x)$ is the integrand, a is the lower limit of the integrand and b is the upper limit of the integrand.

Trapezoidal Rule is based on the Newton-Cotes Formula [121] that states if one can approximate the integrand as an n^{th} order polynomial. Then the integral of that function is approximated by the integral of that n^{th} order polynomial.

$$f_n(x) = a_0 + a_1 x + ... + a_{n-1}x^{n-1} + a_n x^n \tag{6.3}$$

So,

$$\int_a^b f(x)dx \approx \int_a^b f_n(x)dx \tag{6.4}$$

Trapezoidal Rule assumes n=1, that is, the area under the lineal polynomial:

$$\int_a^b f(x)dx = (b-a)[\frac{f(a)+f(b)}{2}] \tag{6.5}$$

In the time-activity curve the trapezoidal rule approximates the area under the curve as the sum of the areas of the trapezoids that are formed, extrapolating the last point to infinity (figure 6.7). From scan start to scan end, the area is described as the sum of the trapezoid areas (6.5). From t_0 to scan start point the area is described as a triangle area:

$$A_0 = t_1 \frac{A_1}{2} \tag{6.6}$$

In order to extrapolate the last point to infinity we integrate the disintegration function, as it is detailed in the next equations:

$$\int_{scanend}^{\infty} f(x)dx = \int_{scanend}^{\infty} A_0 e^{-\lambda t} = \frac{A_{scanend}}{\lambda} \tag{6.7}$$

where λ is the decay constant.

Taking into account the definition of the λ as its probability of decay per unit time, we can express the area under the last point to infinity as:

$$T_{1/2} = \frac{ln2}{\lambda} \tag{6.8}$$

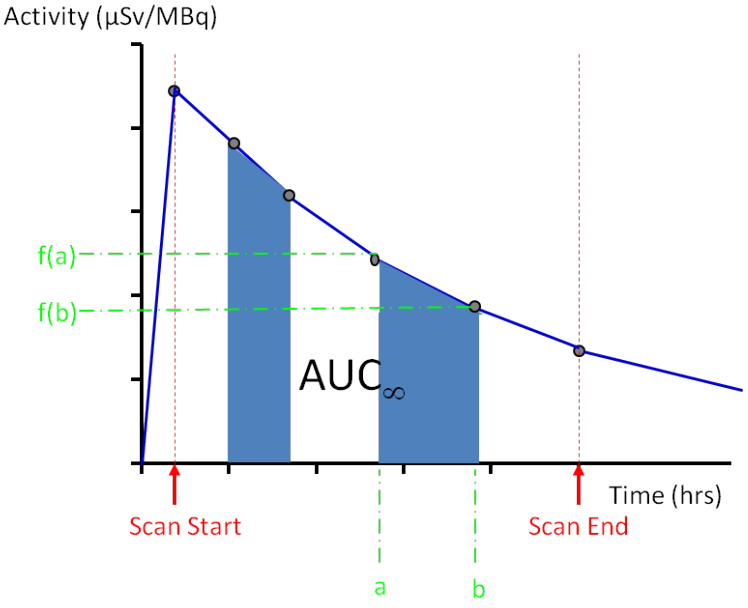

FIGURE 6.7: Trapezoidal rule is applied in order to estimate the area under the time-activity curve.

$$\int_{scanend}^{\infty} f(x)dx = A_{scanend}\frac{T_{1/2}}{ln2} \tag{6.9}$$

where $T_{1/2}$ is the half-life of the nucleid.

Figure 6.6 shows the steps that follows the MATLAB routine develop for a dynamic study analysis. Firstly, TACs file is created with the mean dose values of the organs or voxels of interest (as requested) and the respective time points of the dynamic study. Then, area under each TAC is estimated as it was described in previous section (trapezoidal rule). The output file gives us cumulative total dose in organ or voxel level.

6.3 Application to a Theoretical Case

In order to validate the developed routines, we have used simulated PET images where the activity of the radiopharmaceutical is well known. The details of the study of these simulated PET images were described in *Chapter* 4.

6.3.1 Geometry and Source Specifications

Patient anatomy was represented by the voxelized Zubal phantom with a resolution of $128 \times 128 \times 352$ mm^3 and a voxel size of $5.47 \times 5.47 \times 3.34$ mm^3. This phantom represents the CT of the study and it was used to create the geometry file for simulation. Simulations materials were changed to the mass densities of lungs, water, muscle, bone and air. Table 6.1 provides the list of materials and associated density considered.

Kinetic patient was represented by the simulated PET images described in subsection 4.2.2. Nine acquisitions over time performed the PET simulated dynamic study. Developed routines (fig. 6.3) were applied to each acquisition; nine output source files were obtained. Each file defines voxel, ROI which it belongs and probability density function that the positron annihilation was produced in that voxel.

6.3.2 Monte Carlo Dose Calculations

Simulations were performed for $[^{11}C]$GSK931145 biodistribution, one of the radionuclides studied in Chapter 4, the energy emission spectrum of $[^{11}C]$ was introduced in penEasy main program. As regards radiation transport, for the total dose calculation (beta+gamma) were considered. To calculate separately the photon contribution, an additional simulation was carried out disregarding electron/positron transport, and setting the kinetic energy of positrons to 10 keV.

For total dose calculations, absorption energy for electrons, positrons and photons ($E_{e^-;e^+;ph}$) was set to 960 keV ($e^-$and e^+) and 10 keV (ph). It was considered that positron energy is absorbed in the voxel itself. As for the rest of simulation parameters we set: $C_1 = C_2 = 0.1$, $W_{CC} = E_{abs}^{e^-;e^+}$ and $W_{CR} = E_{abs}^{ph}$. No variance reduction techniques were implemented. An approximate total number of $5E11$ histories were simulated for each frame, calculations for the 9 frames were split into 9 separate statistically independent simulations that ran in parallel on 9 separate CPUs. A statistical uncertainty around 1% was achieved in each voxel. The time needed for simulation was around 72 hours, it can be pointed out that could be reduced with the increasing availability of powerful computers.

The particles path simulated and energy deposition was scored at the voxel level and converted into absorbed dose per simulated history. The output was a text file providing the absorbed dose/disintegration voxel by voxel, together with its statistical uncertainty. Dose distributions calculated by PENELOPE/penEasy MC simulation included self-doses as well as the cross-doses from all source organs.

The ROIs considered were: liver, heart, kidneys, lungs, small intestine and brain. The absorbed dose obtained with the OLINDA/EXM software (see section 4.4.3) was corrected by the mass, due to the anatomical difference between the phantom that OLINDA/EXM uses and the Zubal phantom considered in this study. Finally, the mean organ doses calculated using MC were compared to the organ doses calculated using OLINDA/EXM by finding the percentage difference between doses estimated by each of these methods.

6.3.3 Results

Slices of the resulting AD images in nine different time points after [11C]GSK931145 administration are shown in figure 6.8 . As it was expected, images show high activity in the liver which is the critical organ and activity in the contents of the stomach and small intestine due to the route of clearance of the simulated biodistribution was intestinal.

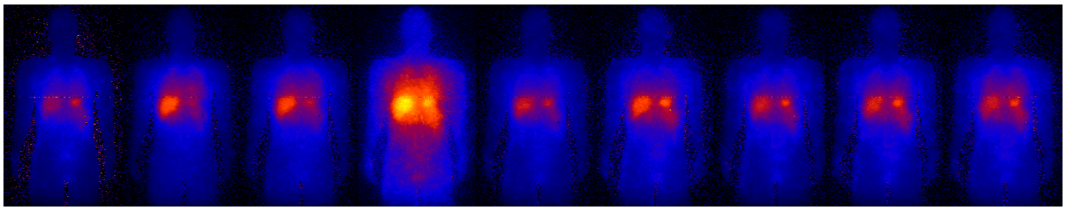

Figure 6.8: Sagittal view of the AD images of the Zubal phantom after 2.4, 6.6, 10.4, 16.2, 22.1, 31.9, 41.8, 59.9 and 85.7 minutes from the radiopharmaceutical administration.

Figure 6.9 shows the total organ doses calculated by OLINDA/EXM and the mean doses calculated with PENELOPE/penEasy MC simulation, both for the case of photons and beta particles, and for only photonic contribution. In the comparison six regions were considered: liver, heart, small intestine, kidneys, lungs and brain.

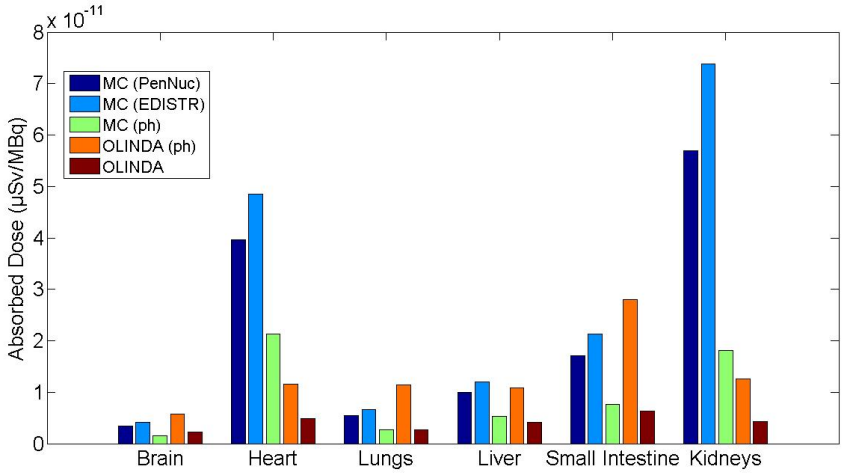

FIGURE 6.9: Absorbed doses in different ROIs calculated by Monte Carlo simulation and OLINDA/EXM software. It was considered photons and beta particles contribution and only photons contribution.

Both versions of PENELOPE/penEasy MC simulations gave us equivalent results. The mean doses calculated with penNuc were 22% lower. Thus, considering that the one that uses EDISTR and penNuc had a similar pattern, from now on EDISTR will be used for comparison purposes.

Liver and heart were considered in this study as the source organs with the highest cumulated activity, where self-irradiation is the dominant contribution to the total dose. Liver percentage differences between Monte Carlo code and OLINDA/EXM doses were -11.16% considering photons and beta particles contribution and -31.35% for only photons contribution. These results are concordant with other studies as *Momennezhad et.al* , who compared absorbed doses calculated with GATE MC simulation and MIRDOSE [122]. They reported percentage differences between GATE MC code and MIRDOSE doses until 24.3% in the liver region. *Grimes et.al* reported percentage differences between EGS MC code and OLINDA/EXM patient-specific S values for liver self-irradiation ranging from 1.8 to 7.3 (using ^{90}Y) or from -2.3 to 1.3 (using ^{131}I) [123].

There was not good agreement regarding the heart or kidneys. The large discrepancies between OLINDA/EXM and Monte Carlo can be explained by the differences in the specific-anatomy used in each case. Mass heart differences between the phantom used in OLINDA/EXM and the Zubal phantom were 88% and 65% for heart and kidneys, respectively.

Lungs region was considered as an example of a large organ and a not uniform tissue medium as it could be the liver region, the percentage differences between Monte Carlo code and OLINDA/EXM doses were 41.64% (ph + β) and 2.32% (ph).

Regarding more distant organs, small intestine is a target organ at a medium distance from the source organs considered in this study. Percentage differences values were 23.84% (ph + β) and -21.28% (ph). In the case of the brain, it is a target organ farther from any source organ. It has practically no activity due to self-irradiation, so the absorbed dose comes from cross-irradiation. Percentage differences were 26.48% (ph + β) and 30.76% (ph).

6.4 Conclusions

Specific routines were developed to be applied together with the PENELOPE/penEasy MC code to perform patient-specific image-based 3D dosimetry by simulating loaded PET/CT or SPECT/CT images. The simulation generates voxel-level absorbed dose maps which include self- and cross-irradiation doses. In addition, information on different parameters can be acquired: cumulative organ dose, maximum and minimum voxel organ values, volume of the organ and dose-volume histograms.

The technique described in this chapter was applied to a theoretical study using simulated PET images of a voxelized Zubal phantom. The results were benchmarked with the ones obtained using the OLINDA/EXM software.

The comparison was in good agreement in those organs were both phantoms considered, Zubal for MC simulation and the reference adult for OLINDA/EXM, were close. Largest differences were observed when sources and targets are distant; it could be expected for photons in a context of cross-irradiation. So, it has to be considered for radiopharmaceuticals with high energy photons where the contributions of cross-irradiation are more significant. However, the major discrepancies were observed for those organs which substantially differ in both models.

OLINDA/EXM is not the best option tool for patient-specific dosimetry when patient anatomy differs from the geometric modeling of the software. Patient anatomy has a large impact in the absorbed dose calculations. The greater the anatomical variation, the greater the differences in dose estimation.

The internal dosimetry toolkit presented in this work offers a novel method using PENELOPE/penEasy MC simulation, to provide patient-specific internal dose estimations that can be applied to patients undergoing PET/CT or SPECT/CT scans.

Chapter 7

Conclusions and Applications

7.1 Conclusions

The aim of this thesis was to optimize radiation dose estimations in diagnostic and therapeutic nuclear medicine procedures. The improvement has been achieved analyzing classical methods commonly used for estimating internal dosimetry and by implementation of patient-specific toolkit to perform image-based 3D dosimetry by simulating loaded PET/CT or SPECT/CT images.

Accuracy of the current radiation exposure estimation methods was assessed in *Chapter 4*. This estimation is based on biodistribution and dosimetry studies, where the main study aspects related to this accuracy are ROI delineation methods and reconstruction algorithms. Other features such as the biokinetic of the radiopharmaceutical and the scatter correction were taking into account. So, it was developed a gold standard to which compare the delineation methods to study: antero-posterior compressed images (AP), subsample of the organs (S) and whole-organ (W). It was concluded that:

- ED estimations were sensitive to whichever delineation ROI method was applied.
- Subsampled organ method showed the best balance between quantitative accuracy and practical implementation.
- Biokinetics of the radioligand influences in the ED estimation.
- Radioligands with an intestinal route of excretion overestimate ED in planar methods due to the involved organs.
- Similar quantitative accuracy was found either with FBP (2D and 3D) and OSEM reconstruction methods.

- Full scatter correction and single scatter correction showed comparable quantitative accuracy.

Moreover, the same pattern related to accuracy was found when using full scatter correction and single scatter correction.

Inter- and intra-operator variability of currently used dose calculation procedures was assessed in *Chapter 5*. It was provided for first time (to the best of our knowledge) insight into the impact of operator variability in dose estimations. It was concluded that:

- 3D methods showed higher reproducibility in comparison with 2D planar method.
- AP method showed the highest inter-operator variability, which implies an overestimation of the ED.
- Subsampled organ method showed the best balance between quantitative accuracy, inter- and intra-subject variability and practical implementation.

The implemented patient-individualized model presented in *Chapter* 6, yielded a promising method in terms of internal dosimetry estimations. Specific routines were developed to be applied with the PENELOPE/penEasy MC code to perform patient-specific image-based 3D dosimetry. Voxel-level absorbed dose maps which include self- and cross-irradiation doses were generated from the morphological and functional patient images. The information of other parameters of interest was reported, such as cumulative organ dose, maximum and minimum voxel organ values, volume of the organ and dose-volume histograms. The model implemented was applied to a theoretical study using simulated PET images of a voxelized phantom. The results were benchmarked with the ones obtained using the OLINDA/EXM software. It was observed that OLINDA/EXM is not the best option tool for internal dose estimates when patient anatomy differs from the geometric modeling incorporated in the software. So, patient anatomy has a large impact in the AD calculations. The internal dosimetry toolkit presented in this work offers a novel method using PENELOPE/penEasy MC simulation to provide patient-specific internal dose estimations.

7.2 Applications

The present work offers new insights on the optimal way to use the classical methods of internal dosimetry. In particular, the optimal way to delineate reference regions and the impact of different reconstruction and correction methods.

A second important application of this thesis is the field of theranostic with the distribution of a targeting agent labelled with a gamma or positron emitting isotope can be measured using SPECT and PET, respectively. Subsequently, the targeting agent can be labelled with an alpha or beta (β^-) emitting isotope (e.g. ^{177}Lu, ^{131}I, etc.) and used for radionuclide therapy. This is the case of several compounds currently used for oncological treatment [124]. In this context, the results of this thesis provide an excellent tool to perform patient-specific internal dosimetry in order to provide optimal effective dose. Thus, the internal dosimetry toolkit presented in this work also offers a powerful tool to assess the value of potential new theranostic agents and in this way encouraging further development in humans. Conversely, this tool may also help to take the decision to discontinue the development of a theranostic agent that do not deliver enough radioactive dose to the target and probably lacking efficacy.

7.3 List of Publications

This thesis work has give rise to several oral presentations and posters in conferences and a paper submitted to journal.

- **López-Vilanova N.**, Duch M.A., Bullich S. Dosimetría interna de pacientes de medicina nuclear con el código de simulación PENELOPE. Oral communication in National Congress of the Radiation Protection Spanish Society and the Medical Physics Spanish Society (SEFM & SEPR). June 2017, Girona, Spain.

- **López-Vilanova N.**, Pavía J., Duch M.A., Catafau A., Ros D., Bullich S. Impact of fegion-of-interest delineation methods, reconstruction algorithms, and intra- and inter-operator variability in internal dosimetry estimates using PET, Mol Imaging Biol (2017) 19:305-314.

- **López-Vilanova N.**, Pavía J., Duch M.A., Catafau A., Ros D., Bullich S. Study on PET internal dosimetry estimates using different region-of-interest delineation methods. Analysis of intra- and inter- operator variability. Oral communication in 13th European Association of Nuclear Medicine (EANM) meeting. October 2013, Lyon, France.

- **López-Vilanova N.**, Pavía J., Ros D., Bullich S. Impact of region-of-interest delineation methods on internal dosimetry estimates using PET. Radiotherapy and Oncology, 103 (Supp 1), May 2012: S536-S537. Poster in 31st European Society for Therapeutic Radiology and Oncology (ESTRO) meeting. May 2012, Barcelona, Spain.

Bibliography

[1] E. Commission, "Radiation protection n° 180. medical radiation exposure of the european population. part 1/2," 2014, available from: https://ec.europa.eu/energy/sites/ener/files/documents/RP180.pdf.

[2] A. Rahmim and H. Zaidi, "PET versus SPECT: strengths, limitations and challenges," *Nuclear Medicine Communications*, vol. 29, no. 3, 2008.

[3] A. A. M. van der Veldt, E. F. Smit, and A. A. Lammertsma, "Positron Emission Tomography as a Method for Measuring Drug Delivery to Tumors in vivo: The Example of [11C]docetaxel," *Frontiers in Oncology*, vol. 3, no. August, p. 208, 2013. [Online]. Available: http://journal.frontiersin.org/article/10.3389/fonc.2013.00208/abstract

[4] C.-H. Yeong, M.-H. Cheng, and K.-H. Ng, "Therapeutic radionuclides in nuclear medicine: current and future prospects," *Journal of Zhejiang University Science B*, vol. 15, no. 10, pp. 845–863, 2014. [Online]. Available: http://link.springer.com/10.1631/jzus.B1400131

[5] S. Bullich, M. Slifstein, J. Passchier, N. V. Murthy, L. S. Kegeles, J.-H. Kim, X. Xu, R. N. Gunn, R. Herance, J. D. Gispert, A. Gutiérrez, M. Farré, M. Laruelle, and A. M. Catafau, "Biodistribution and Radiation Dosimetry of the Glycine Transporter-1 Ligand (11)C-GSK931145 Determined from Primate and Human Whole-Body PET." *Molecular imaging & biology : MIB : the official publication of the Academy of Molecular Imaging*, vol. 13, no. 4, pp. 776–784, Aug. 2011. [Online]. Available: http://www.ncbi.nlm.nih.gov/pubmed/20730499

[6] M. Lassmann and G. Pedroli, "Dose optimization in nuclear medicine," *Clinical and Translational Imaging*, vol. 4, no. 1, pp. 3–4, Feb 2016. [Online]. Available: https://doi.org/10.1007/s40336-015-0154-7

[7] E. Commission, "Proyecto DOMNES. Prospección Nacional de procedimientos de diagnóstico en medicina nuclear utilizados en los centros sanitarios Españoles. Estimación de dosis recibidas por los pacientes y la población," 2012.

[8] M. Cremonesi, M. E. Ferrari, L. Bodei, C. Chiesa, A. Sarnelli, C. Garibaldi, M. Pacilio, L. Strigari, P. E. Summers, R. Orecchia, C. M. Grana, and F. Botta, "Correlation of dose with toxicity and tumour response to 90Y- and 177Lu-PRRT provides the basis for optimization through individualized treatment planning," *European Journal of Nuclear Medicine and Molecular Imaging*, vol. 45, no. 13, pp. 2426–2441, Dec 2018. [Online]. Available: https://doi.org/10.1007/s00259-018-4044-x

[9] L. Strigari, M. Konijnenberg, C. Chiesa, M. BardiesYong, D. Sjögreen, G. Lassmann, and G. Flux, "The evidence base for the use of internal dosimetry in the clinical practice of molecular radiotherapy," *European Journal of Nuclear Medicine and Molecular Imaging*, vol. 41, no. 10, p. 1976–1988, 2014.

[10] C. Alberti, "From molecular imaging in preclinical/clinical oncology to theranostic applications in targeted tumor therapy," *European Review for Medical and Pharmacological Sciences*, vol. 16, no. 14, pp. 1925–1933, 2012.

[11] P. Sharma and A. Mukherjee, "Newer positron emission tomography radiopharmaceuticals for radiotherapy planning : an overview," vol. 4, no. 2, pp. 1–7, 2016.

[12] X. Geets, J.-F. Daisne, V. Gregoire, M. Hamoir, and M. Lonneux, "Role of 11-C-methionine positron emission tomography for the delineation of the tumor volume in pharyngo-laryngeal squamous cell carcinoma: comparison with FDG-PET and CT," *Radiotherapy and Oncology*, vol. 71, no. 3, pp. 267–273, jun 2004. [Online]. Available: https://doi.org/10.1016/j.radonc.2004.02.013

[13] M. Picchio, C. Crivellaro, G. Giovacchini, L. Gianolli, and C. Messa, "PET-CT for treatment planning in prostate cancer," *The quarterly journal of nuclear medicine and molecular imaging*, vol. 53, no. 2, pp. 245–268, apr 2009.

[14] R. J. Bleicher, R. Essner, L. J. Foshag, L. A. Wanek, and D. L. Morton, "Role of sentinel lymphadenectomy in thin invasive cutaneous melanomas," *Journal of Clinical Oncology*, vol. 21, no. 7, pp. 1326–1331, 2003, pMID: 12663722. [Online]. Available: https://doi.org/10.1200/JCO.2003.06.123

[15] M. Luster, S. E. Clarke, M. Dietlein, M. Lassmann, P. Lind, W. J. G. Oyen, J. Tennvall, and E. Bombardieri, "Guidelines for radioiodine therapy of differentiated thyroid cancer," *European Journal of Nuclear Medicine and Molecular Imaging*, vol. 35, no. 10, p. 1941, Aug 2008. [Online]. Available: https://doi.org/10.1007/s00259-008-0883-1

[16] J. J. Zaknun, L. Bodei, J. Mueller-Brand, M. E. Pavel, R. P. Baum, D. Hörsch, M. S. O'Dorisio, T. M. O'Dorisiol, J. R. Howe, M. Cremonesi, and D. J. Kwekkeboom, "The joint IAEA, EANM, and SNMMI practical guidance on peptide receptor radionuclide therapy (PRRNT) in neuroendocrine tumours," *European Journal of Nuclear Medicine and Molecular Imaging*, vol. 40, no. 5, pp. 800–816, 2013.

[17] S. Basu, T. C. Kwee, S. Surti, E. A. Akin, D. Yoo, and A. Alavi, "Fundamentals of pet and pet/ct imaging," *Annals of the New York Academy of Sciences*, vol. 1228, no. 1, pp. 1–18. [Online]. Available: https://nyaspubs.onlinelibrary.wiley.com/doi/abs/10.1111/j.1749-6632.2011.06077.x

[18] T. C. Kwee, D. A. Torigian, and A. Alavi, "Overview of positron emission tomography, hybrid positron emission tomography instrumentation, and positron emission tomography quantification," *Journal of Thoracic Imaging*, vol. 28, no. 1, pp. 4–10, 2013.

[19] T. G. Turkington, "Introduction to PET instrumentation." *Journal of nuclear medicine technology*, vol. 29, no. 1, pp. 4–11, 2001. [Online]. Available: http://www.ncbi.nlm.nih.gov/pubmed/11283211

[20] P. Zanzonico, "Positron emission tomography: a review of basic principles, scanner design and performance, and current systems," *Seminars in Nuclear Medicine*, vol. 34, no. 2, pp. 87 – 111, 2004. [Online]. Available: http://www.sciencedirect.com/science/article/pii/S0001299803001041

[21] S. DeBenedetti, C. E. Cowan, W. R. Konneker, and H. Primakoff, "On the angular distribution of two-photon annihilation radiation," *Phys. Rev.*, vol. 77, pp. 205–212, Jan 1950. [Online]. Available: https://link.aps.org/doi/10.1103/PhysRev.77.205

[22] S. R. Cherry and M. Dahlbom, *PET: Physics, Instrumentation, and Scanners*. Springer, 2006.

[23] D. W. Townsend, *Basic Science of PET and PET/CT*. Springer, 2006.

[24] J. A. Sorenson and M. E. Phelps. Orlando, Florida: Grune and Stratton, 1987.

[25] R. D. Badawi and P. K. Marsden, "Developments in component-based normalization for 3D PET." *Physics in medicine and biology*, vol. 44, no. 2, pp. 571–594, feb 1999.

[26] G. Muehllehner and J. S. Karp, "Positron emission tomography," *Physics in Medicine & Biology*, vol. 51, no. 13, p. R117, 2006. [Online]. Available: http://stacks.iop.org/0031-9155/51/i=13/a=R08

[27] P. E. Kinahan, B. H. Hasegawa, and T. Beyer, "X-ray-based attenuation correction for positron emission tomography/computed tomography scanners," *Seminars in Nuclear Medicine*, vol. 33, no. 3, pp. 166 – 179, 2003. [Online]. Available: http://www.sciencedirect.com/science/article/pii/S0001299803700038

[28] C. S. Levin, M. Dahlbom, and E. J. Hoffman, "A Monte Carlo correction for the effect of Compton scattering in 3D PET brain imaging," *IEEE Transactions on Nuclear Science*, vol. 42, no. 4, pp. 1181–1185, Aug 1995.

[29] H. Zaidi, "Comparative evaluation of scatter correction techniques in 3d positron emission tomography," *European Journal of Nuclear Medicine*, vol. 27, no. 12, pp. 1813–1826, Dec 2000. [Online]. Available: https://doi.org/10.1007/s002590000385

[30] N. Boussion, M. Hatt, F. Lamare, Y. Bizais, A. Turzo, C. C.-L. Rest, and D. Visvikis, "A multiresolution image based approach for correction of partial volume effects in emission tomography," *Physics in Medicine & Biology*, vol. 51, no. 7, p. 1857, 2006. [Online]. Available: http://stacks.iop.org/0031-9155/51/i=7/a=016

[31] M. Soret, S. L. Bacharach, and I. Buvat, "Partial-Volume Effect in PET Tumor Imaging," *Journal of Nuclear Medicine*, vol. 48, no. 6, pp. 932–945, 2007. [Online]. Available: http://jnm.snmjournals.org/cgi/doi/10.2967/jnumed.106.035774

[32] J. G. Colsher, "Fully-three-dimensional positron emission tomography," *Physics in Medicine & Biology*, vol. 25, no. 1, p. 103, 1980. [Online]. Available: http://stacks.iop.org/0031-9155/25/i=1/a=010

[33] L. A. Shepp and Y. Vardi, "Maximum likelihood reconstruction for emission tomography." *IEEE transactions on medical imaging*, vol. 1, no. 2, pp. 113–122, 1982.

[34] H. M. Hudson and R. S. Larkin, "Accelerated image reconstruction using ordered subsets of projection data," *IEEE transactions on medical imaging*, vol. 13, no. 4, pp. 601–609, 1994.

[35] H. Zaidi and I. El Naqa, "PET-guided delineation of radiation therapy treatment volumes: A survey of image segmentation techniques," *European Journal of Nuclear Medicine and Molecular Imaging*, vol. 37, no. 11, pp. 2165–2187, 2010.

[36] J. Czernin, M. Allen-auerbach, and H. R. Schelbert, "Improvements in Cancer Staging with PET / CT : Literature-Based Evidence as of September 2006," vol. 48, no. 1, pp. 78–89, 2007.

[37] E. M. Kamel, S. Korom, B. Seifert, D. Ph, G. K. V. Schulthess, D. Ph, and H. C. Steinert, "Staging of Non–Small-Cell Lung Cancer with Integrated Positron-Emission Tomography and Computed Tomography," pp. 2500–2507, 2003.

[38] R. W. Howell, B. W. Wessels, and R. Loevinger, "The MIRD Perspective 1999," *Journal of Nuclear Medicine*, vol. 40, no. 1, pp. 3S–10S, 1999.

[39] W. E. Bolch, K. F. Eckerman, G. Sgouros, and S. R. Thomas, "MIRD Pamphlet No. 21: A Generalized Schema for Radiopharmaceutical Dosimetry–Standardization of Nomenclature," *Journal of Nuclear Medicine*, vol. 50, no. 3, pp. 477–484, 2009. [Online]. Available: http://jnm.snmjournals.org/cgi/doi/10.2967/jnumed.108.056036

[40] M. G. Stabin and J. A. Siegel, "Physical models and dose factors for use in internal dose assessment." *Health physics*, vol. 85, no. 3, pp. 294–310, sep 2003.

[41] M. G. Stabin, R. B. Sparks, and E. Crowe, "OLINDA/EXM: the second-generation personal computer software for internal dose assessment in nuclear medicine," *Journal of nuclear medicine : official publication, Society of Nuclear Medicine*, vol. 46, no. 6, pp. 1023–1027, June 2005. [Online]. Available: http://www.ncbi.nlm.nih.gov/pubmed/15937315

[42] M. G. Stabin, "Update: The case for patient-specific dosimetry in radionuclide therapy," *Cancer Biotherapy and Radiopharmaceuticals*, vol. 23, no. 3, pp. 273–284, 2008, pMID: 18593360. [Online]. Available: https://doi.org/10.1089/cbr.2007.0445

[43] J. a. Siegel, S. R. Thomas, J. B. Stubbs, M. G. Stabin, M. T. Hays, K. F. Koral, J. S. Robertson, R. W. Howell, B. W. Wessels, D. R. Fisher, D. a. Weber, and a. B. Brill, "MIRD pamphlet no. 16: Techniques for quantitative radiopharmaceutical biodistribution data acquisition and analysis for use in human radiation dose estimates." *Journal of nuclear medicine : official publication, Society of Nuclear Medicine*, vol. 40, no. 2, pp. 37S–61S, feb 1999. [Online]. Available: http://www.ncbi.nlm.nih.gov/pubmed/10025848

[44] B. E. Zimmerman, D. Grošev, I. Buvat, M. A. Coca Pérez, E. C. Frey, A. Green, A. Krisanachinda, M. Lassmann, M. Ljungberg, L. Pozzo, K. A. Quadir, M. A. Terán Gretter, J. Van Staden, and G. L. Poli, "Multi-centre evaluation of accuracy and reproducibility of planar and SPECT image quantification: An IAEA phantom study," *Zeitschrift fur Medizinische Physik*, vol. 27, no. 2, pp. 98–112, 2017.

[45] A. E. Besemer, B. Titz, J. J. Grudzinski, J. P. Weichert, J. S. Kuo, H. I. Robins, L. T. Hall, and B. P. Bednarz, "Impact of PET and MRI threshold-based tumor volume segmentation on patient-specific targeted radionuclide therapy dosimetry

using CLR1404," *Physics in Medicine & Biology*, vol. 62, no. 15, p. 6008, 2017. [Online]. Available: http://stacks.iop.org/0031-9155/62/i=15/a=6008

[46] M. G. Stabin, "MIRDOSE: personal computer software for internal dose assessment in nuclear medicine," *Journal of nuclear medicine : official publication, Society of Nuclear Medicine*, vol. 37, no. 3, pp. 538–546, 1996.

[47] M. Cristy and K. Eckerman, *Specific Absorbed Fractions of Energy at Various Ages from Internal Photon Sources: 1, Methods*, 1987. [Online]. Available: http://ordose.ornl.gov/documents/tm8381V1.pdf

[48] M. G. Stabin, M. A. Emmons, W. P. Segars, and M. J. Fernald, "Realistic reference adult and paediatric phantom series for internal and external dosimetry," *Radiation Protection Dosimetry*, vol. 149, no. 1, pp. 56–59, 2012.

[49] L. Zheng-Ming and A. Brahme, "An overview of the transport theory of charged particles," *Radiation Physics and Chemistry*, vol. 41, no. 4, pp. 673 – 703, 1993. [Online]. Available: http://www.sciencedirect.com/science/article/pii/0969806X9390318O

[50] H. Zaidi and K. F. Koral, "Scatter modelling and compensation in emission tomography," *European Journal of Nuclear Medicine and Molecular Imaging*, vol. 31, no. 5, pp. 761–782, May 2004. [Online]. Available: https://doi.org/10.1007/s00259-004-1495-z

[51] H. Zaidi, "Relevance of accurate monte carlo modeling in nuclear medical imaging," *Medical Physics*, vol. 26, no. 4, pp. 574–608. [Online]. Available: https://aapm.onlinelibrary.wiley.com/doi/abs/10.1118/1.598559

[52] I. Castiglioni, O. Cremonesi, M. C. Gilardi, V. Bettinardi, G. Rizzo, A. Savi, E. Bellotti, and F. Fazio, "Scatter correction techniques in 3d pet: a monte carlo evaluation," *IEEE Transactions on Nuclear Science*, vol. 46, no. 6, pp. 2053–2058, Dec 1999.

[53] M. Belanger, J. Yanch, A. Lu, and A. Dobrznecki, "The simspect photon selector and multiple angular sampling of photons," *Regional Anesthesia and Pain Medicine*, vol. 3, pp. 2023–2025, 02 1998.

[54] C. J. Thompson, J. Moreno-Cantu, and Y. Picard, "PETSIM: Monte Carlo simulation of all sensitivity and resolution parameters of cylindrical positron imaging systems." *Physics in medicine and biology*, vol. 37, no. 3, pp. 731–749, mar 1992.

[55] R. Harrison, S. Vannoy, D. Haynor, S. Gillispie, M. Kaplan, and T. Lewellen, "Preliminary Experience With The Photon History Generator Module Of A

Public-domain Simulation System For Emission Tomography," *1993 IEEE Conference Record Nuclear Science Symposium and Medical Imaging Conference*, pp. 1154–1158. [Online]. Available: http://ieeexplore.ieee.org/lpdocs/epic03/wrapper.htm?arnumber=701828

[56] H. Zaidi, C. Labbé, and C. Morel, "Implementation of an environment for Monte Carlo simulation of fully 3-D positron tomography on a high-performance parallel platform," *Parallel Computing*, vol. 24, no. 9, pp. 1523–1536, 1998.

[57] S. Jan, G. Santin, D. Strul, S. Staelens, K. Assié, and et.al., "GATE: a simulation toolkit for PET and SPECT," *Physics in medicine and biology*, vol. 49, no. 19, pp. 4543–4561, oct 2004.

[58] P. Arce, P. Rato, M. Canadas, and J. I. Lagares, "Gamos: A geant4-based easy and flexible framework for nuclear medicine applications," in *2008 IEEE Nuclear Science Symposium Conference Record*, Oct 2008, pp. 3162–3168.

[59] S. España, J. L. Herraiz, E. Vicente, J. J. Vaquero, M. Desco, and J. M. Udias, "Penelopet, a monte carlo pet simulation tool based on penelope: features and validation," *Physics in Medicine & Biology*, vol. 54, no. 6, p. 1723, 2009. [Online]. Available: http://stacks.iop.org/0031-9155/54/i=6/a=021

[60] A. McLennan, A. Reilhac, and M. Brady, "Sorteo: Monte carlo-based simulator with list-mode capabilities," *Conference proceedings : Annual International Conference of the IEEE Engineering in Medicine and Biology Society. IEEE Engineering in Medicine and Biology Society. Annual Conference*, vol. 2009, pp. 3751–3754, 2009.

[61] M. Bahreyni Toossi, J. Islamian, M. Momennezhad, M. Ljungberg, and S. Naseri, "SIMIND Monte Carlo simulation of a single photon emission CT," *Journal of Medical Physics*, vol. 35, no. 1, pp. 42–47, 2010.

[62] E. Union, "Council Directive 2013/59/Euratom. Off J Eur Union," pp. 1–73, 2014.

[63] T. Lewellen, R. Harrison, and S. Vannoy, "The simset program, in monte carlo calculations," in *Monte Carlo Calculations in Nuclear Medicine*, M. Ljungberg, S. Strand, and M. King, Eds., Institute of Physics Publishing: Philadelphia, 1998, pp. 77–92.

[64] I. G. Zubal, C. R. Harrell, E. O. Smith, Z. Rattner, G. Gindi, and P. B. Hoffer, "Computerized three-dimensional segmented human anatomy," *Medical Physics*, vol. 21, no. 2, pp. 299–302, 1994. [Online]. Available: https://aapm.onlinelibrary.wiley.com/doi/abs/10.1118/1.597290

[65] K. Thielemans, C. Tsoumpas, S. Mustafovic, T. Beisel, P. Aguiar, N. Dikaios, and M. W. Jacobson, "STIR: software for tomographic image reconstruction release 2," *Physics in medicine & biology*, vol. 57, no. 4, pp. 867–83, feb 2012. [Online]. Available: http://www.ncbi.nlm.nih.gov/pubmed/22290410

[66] F. Salvat, J. Fernández-Varea, and J. Sempau, *PENELOPE-2008 : A Code System for Monte Carlo Simulation*. OECD/Nuclear Energy Agency, Issy-les-Molineaux, France, 2008, no. 6416.

[67] J. Baró, J. Sempau, J. Fernández-Varea, and F. Salvat, "PENELOPE: An algorithm for Monte Carlo simulation of the penetration and energy loss of electrons and positrons in matter," *Nuclear Instruments and Methods in Physics Research Section B: Beam Interactions with Materials and Atoms*, vol. 100, no. 1, pp. 31 – 46, 1995. [Online]. Available: http://www.sciencedirect.com/science/article/pii/0168583X95003495

[68] J. Sempau, A. Badal, and L. Brualla, "A PENELOPE-based system for the automated Monte Carlo simulation of clinacs and voxelized geometries-application to far-from-axis fields," *Medical Physics*, vol. 38, no. 11, pp. 5887–5895, 2011.

[69] W. Schneider, T. Bortfeld, and W. Schlegel, "Correlation between ct numbers and tissue parameters needed for monte carlo simulations of clinical dose distributions," *Physics in Medicine & Biology*, vol. 45, no. 2, p. 459, 2000. [Online]. Available: http://stacks.iop.org/0031-9155/45/i=2/a=314

[70] B. Vanderstraeten, P. W. Chin, M. Fix, A. Leal, G. Mora, N. Reynaert, J. Seco, M. Soukup, E. Spezi, W. D. Neve, and H. Thierens, "Conversion of ct numbers into tissue parameters for monte carlo dose calculations: a multi-centre study," *Physics in Medicine & Biology*, vol. 52, no. 3, p. 539, 2007. [Online]. Available: http://stacks.iop.org/0031-9155/52/i=3/a=001

[71] M. Stabin and J. A. Siegel, "Radar Dose Estimate Report: a Compendium of Radiopharmaceutical Dose Estimates Based on Olinda/Exm Version 2.0," *Journal of Nuclear Medicine*, vol. 59, no. 1, p. jnumed.117.196261, 2017. [Online]. Available: http://jnm.snmjournals.org/lookup/doi/10.2967/jnumed.117.196261

[72] M. Stabin, J. Siegel, J. Hunt, R. Sparks, J. Lipsztein, and K. Eckerman, "Radar - the radiation dose assessment resource. an online source of dose information for nuclear medicine and occupational radiation safety," *Journal of Nuclear Medicine*, vol. 42, p. 243, 2001.

[73] M. G. Stabin, R. B. Sparks, and E. Crowe, "OLINDA/EXM: the second-generation personal computer software for internal dose assessment in nuclear

medicine." *Journal of nuclear medicine : official publication, Society of Nuclear Medicine*, vol. 46, no. 6, pp. 1023–7, jun 2005. [Online]. Available: http://www.ncbi.nlm.nih.gov/pubmed/15937315

[74] M.-J. Bélanger, N. R. Simpson, T. Wang, R. L. Van Heertum, J. J. Mann, and R. V. Parsey, "Biodistribution and radiation dosimetry of [11C]DASB in baboons," *Nuclear medicine & biology*, vol. 31, no. 8, pp. 1097–102, nov 2004. [Online]. Available: http://www.ncbi.nlm.nih.gov/pubmed/15607492

[75] K. Van Laere, M. Koole, S. M. Sanabria Bohorquez, K. Goffin, I. Guenther, M. J. Belanger, J. Cote, P. Rothenberg, I. De Lepeleire, I. D. Grachev, R. J. Hargreaves, G. Bormans, and H. D. Burns, "Whole-body biodistribution and radiation dosimetry of the human cannabinoid type-1 receptor ligand 18F-MK-9470 in healthy subjects," *Journal of nuclear medicine : official publication, Society of Nuclear Medicine*, vol. 49, no. 3, pp. 439–45, mar 2008. [Online]. Available: http://www.ncbi.nlm.nih.gov/pubmed/18287275

[76] M. Slifstein, D.-R. Hwang, D. Martine, J. Ekelun, Y. Huang, E. Hackett, A. Abi-Darghamand, and M. Laruelle, "Biodistribution and Radiation Dosimetry of the Dopamine D2 Ligand 11C-Raclopride Determined from Human Whole-Body PET," *Nuclear medicine & biology*, vol. 47, pp. 313–319, 2006.

[77] M.-J. a. Ribeiro, M. Ricard, S. Bourgeois, M.-A. Lièvre, M. Bottlaender, P. Gervais, F. Dollé, and A. Syrota, "Biodistribution and radiation dosimetry of [11C]raclopride in healthy volunteers," *European journal of nuclear medicine and molecular imaging*, vol. 32, no. 8, pp. 952–8, Aug. 2005. [Online]. Available: http://www.ncbi.nlm.nih.gov/pubmed/15841376

[78] N. M. Scheinin, T. K. Tolvanen, I. Wilson, E. M. Arponen, K. a. Någren, and J. O. Rinne, "Biodistribution and radiation dosimetry of the amyloid imaging agent 11C-PIB in humans," *Journal of nuclear medicine : official publication, Society of Nuclear Medicine*, vol. 48, no. 1, pp. 128–33, jan 2007. [Online]. Available: http://www.ncbi.nlm.nih.gov/pubmed/17204709

[79] A. K. Brown, M. Fujita, Y. Fujimura, J.-S. Liow, M. Stabin, Y. H. Ryu, M. Imaizumi, J. Hong, V. W. Pike, and R. B. Innis, "Radiation dosimetry and biodistribution in monkey and man of 11C-PBR28: a PET radioligand to image inflammation," *Journal of nuclear medicine : official publication, Society of Nuclear Medicine*, vol. 48, no. 12, pp. 2072–9, dec 2007. [Online]. Available: http://www.ncbi.nlm.nih.gov/pubmed/18006619

[80] V. L. Cropley, M. Fujita, J. L. Musachio, J. Hong, S. Ghose, J. Sangare, P. J. Nathan, V. W. Pike, and R. B. Innis, "Whole-body biodistribution and

estimation of radiation-absorbed doses of the dopamine D1 receptor radioligand 11C-NNC 112 in humans," *Journal of nuclear medicine : official publication, Society of Nuclear Medicine*, vol. 47, no. 1, pp. 100–4, jan 2006. [Online]. Available: http://www.ncbi.nlm.nih.gov/pubmed/16391193

[81] V. D. Lu Jian-Qiang, Ichise Masanori, LiowJeih-San, Ghose Subroto, "Biodistribution and Radiation Dosimetry of the Determined from Human Whole-Body PET," *J. Nucl. Med.*, vol. 45, pp. 1555–1559, 2004.

[82] D. R. Sprague, M. Fujita, Y. H. Ryu, J.-S. Liow, V. W. Pike, and R. B. Innis, "Whole-body biodistribution and radiation dosimetry in monkeys and humans of the phosphodiesterase 4 radioligand [(11)C](R)-rolipram: comparison of two-dimensional planar, bisected and quadrisected image analyses," *Nuclear Medicine & biology*, vol. 35, no. 4, pp. 493–500, may 2008.

[83] D. N. Tipre, J. Lu, M. Fujita, M. Ichise, D. Vines, and R. B. Innis, "Radiation dosimetry estimates for the PET serotonin transporter probe 11 C-DASB determined from whole-body imaging in non-human primates," *Nuclear Medicine Communications*, pp. 81–86, 2004.

[84] P. Papadimitroulas, G. Loudos, A. Le Maitre, M. Hatt, F. Tixier, N. Efthimiou, G. C. Nikiforidis, D. Visvikis, and G. C. Kagadis, "Investigation of realistic PET simulations incorporating tumor patient's specificity using anthropomorphic models: Creation of an oncology database," *Medical Physics*, vol. 40, no. 11, 2013.

[85] J. M. Ollinger, "Model-based scatter correction for fully 3D PET," *Physics in medicine & biology*, vol. 41, no. 1, pp. 153–76, jan 1996. [Online]. Available: http://www.ncbi.nlm.nih.gov/pubmed/8685253

[86] Watson CC, "Correction for 3 0 PET," *New, faster, image-based scatter correction for 3D PET*, vol. 47, no. 4, pp. 1587–1594, 2000.

[87] G. El Fakhri, P. A. Santos, R. D. Badawi, C. H. Holdsworth, A. D. Van Den Abbeele, and M. F. Kijewski, "Impact of acquisition geometry, image processing, and patient size on lesion detection in whole-body 18F-FDG PET," *Journal of nuclear medicine : official publication, Society of Nuclear Medicine*, vol. 48, no. 12, pp. 1951–60, dec 2007. [Online]. Available: http://www.ncbi.nlm.nih.gov/pubmed/18006613

[88] A. Reilhac, S. Tomeï, I. Buvat, C. Michel, F. Keheren, and N. Costes, "Simulation-based evaluation of OSEM iterative reconstruction methods in dynamic brain PET studies," *NeuroImage*, vol. 39, no. 1, pp. 359–368, 2008. [Online]. Available: http://www.sciencedirect.com/science/article/pii/S1053811907006659

[89] D. R. Haynor, R. L. Harrison, and T. K. Lewellen, "The use of importance sampling techniques to improve the efficiency of photon tracking in emission tomography simulations," *Medical physics*, vol. 18, no. 5, pp. 990–1001, jan 1994. [Online]. Available: http://www.ncbi.nlm.nih.gov/pubmed/1961165

[90] X. Zhu and G. El Fakhri, "Monte Carlo modeling of cascade gamma rays in (86)Y PET imaging: preliminary results," *Physics in medicine & biology*, vol. 54, no. 13, pp. 4181–93, jul 2009.

[91] P. Aguiar, "Reconstruction, quantification and standardization methods in positron emission tomography," dissertation, Universitat de Barcelona, 2008.

[92] K. Thielemans, R. Manjeshwar, C. Tsoumpas, and F. Jansen, "A new algorithm for scaling of PET scatter estimates using all coincidence events," *IEEE Nuclear Science Symposium Conference Record*, pp. 3586–3590, 2007. [Online]. Available: http://ieeexplore.ieee.org/lpdocs/epic03/wrapper.htm?arnumber=4436900

[93] M. E. Daube-Witherspoon and G. Muehllehner, "Treatment of axial data in three-dimensional PET," *Journal of nuclear medicine : official publication, Society of Nuclear Medicine*, vol. 28, no. 11, pp. 1717–1724, 1987. [Online]. Available: http://www.ncbi.nlm.nih.gov/pubmed/3499493

[94] M. W. Groch and W. D. Erwin, "Single-Photon Emission Computed Tomography in the Year 2001: Instrumentation and Quality Control," *J Nucl Med Technol*, vol. 29, no. 1, pp. 12–18, 2001.

[95] "Flanged Jaszczak ECT Phantoms." [Online]. Available: http://www.spect.com/pub/Flanged_Jaszczak_Phantoms.pdf

[96] M. Iatrou, S. G. Ross, R. M. Manjeshwar, and C. W. Stearns, "A fully 3d iterative image reconstruction algorithm incorporating data corrections," in *IEEE Symposium Conference Record Nuclear Science 2004.*, vol. 4, Oct 2004, pp. 2493–2497 Vol. 4.

[97] C. Rorden and M. Brett, "Stereotaxic display of brain lesions," *Behavioural neurology*, vol. 12, no. 4, pp. 191–200, jan 2000. [Online]. Available: http://www.ncbi.nlm.nih.gov/pubmed/11568431

[98] IAEA, "Quantitative Nuclear Medicine Imaging: Concepts, Requirements and Methods," Tech. Rep., 2014. [Online]. Available: http://www-pub.iaea.org/books/IAEABooks/10380/Quantitative-Nuclear-Medicine-Imaging-Concepts-Requirements-and-Methods

[99] M. G. Stabin, "Health concerns related to radiation exposure of the female nuclear medicine patient," *Environmental Health Perspectives*, vol. 105, no. SUPPL. 6, pp. 1403–1409, 1997.

[100] M. A. Avila-Rodriguez, C. Rios, J. Carrasco-Hernandez, J. C. Manrique-Arias, R. Martinez-Hernandez, F. O. García-Pérez, A. R. Jalilian, E. Martinez-Rodriguez, M. E. Romero-Piña, and A. Diaz-Ruiz, "Biodistribution and radiation dosimetry of [64Cu]copper dichloride: first-in-human study in healthy volunteers," *EJNMMI Research*, vol. 7, 2017.

[101] M. Lassmann, C. Chiesa, G. Flux, and M. Bardiès, "EANM Dosimetry Committee guidance document: good practice of clinical dosimetry reporting," *European journal of nuclear medicine and molecular imaging*, vol. 38, no. 1, pp. 192–200, jan 2011. [Online]. Available: http://www.ncbi.nlm.nih.gov/pubmed/20799035

[102] H. Zaidi, "Medical image segmentation: Quo vadis," *Computer Methods and Programs in Biomedicine*, vol. 84, no. 2, pp. 63 – 65, 2006, medical Image Segmentation Special Issue. [Online]. Available: http://www.sciencedirect.com/science/article/pii/S0169260706002380

[103] M. S. Nielsen and J. Carl, "Validating PET segmentation of thoracic lesions—is 4D PET necessary?" *Biomedical Physics & Engineering Express*, vol. 3, no. 1, p. 015028, 2017.

[104] B. Foster, U. Bagci, A. Mansoor, Z. Xu, and D. J. Mollura, "A Review on Segmentation of Positron Emission Tomography Images," *Compt Biol Med*, vol. 50, pp. 76–96, 2014.

[105] A.-S. Dewalle-Vignion, N. Yeni, G. Petyt, L. Verscheure, D. Huglo, A. Béron, S. Adib, G. Lion, and M. Vermandel, "Evaluation of pet volume segmentation methods: comparisons with expert manual delineations," *Nuclear Medicine Communications*, vol. 33, no. 1, 2012.

[106] "Human Biodistribution and Radiation Dosimetry of 18F-Clofarabine, a PET Probe Targeting the Deoxyribonucleoside Salvage Pathway," *The Journal of Nuclear Medicine*, vol. 58, no. 3, pp. 374–378, 2017.

[107] N. Pandit-Taskar, P. B. Zanzonico, K. D. Staton, J. A. Carrasquillo, D. Reidy-Lagunes, S. K. Lyashchenko, E. Burnazi, H. Zhang, J. S. Lewis, R. Blasberg, S. M. Larson, W. A. Weber, and S. Modak, "Biodistribution and dosimetry of 18F-Meta Fluorobenzyl Guanidine (MFBG): A first-in-human PET-CT imaging study of patients with neuroendocrine malignancies,"

Journal of Nuclear Medicine, p. jnumed.117.193169, 2017. [Online]. Available: http://jnm.snmjournals.org/lookup/doi/10.2967/jnumed.117.193169

[108] H. Lizana, L. Johansson, J. Axelsson, A. Larsson, M. Ögren, J. Linder, C. Halldin, A. Varrone, and S. J. Mo, "Whole-body biodistribution and dosimetry of the dopamine transporter radioligand 18f-fe-pe2i in human subjects," *Journal of Nuclear Medicine*, vol. 59, no. 8, pp. 1275–1280, 2018. [Online]. Available: http://jnm.snmjournals.org/content/59/8/1275.abstract

[109] C. C. Watson, D. Newport, and M. E. Casey, *A Single Scatter Simulation Technique for Scatter Correction in 3D PET*. Dordrecht: Springer Netherlands, 1996, pp. 255–268. [Online]. Available: https://doi.org/10.1007/978-94-015-8749-5_18

[110] Y. H. Na, B. Zhang, J. Zhang, P. F. Caracappa, and X. G. Xu, "Deformable adult human phantoms for radiation protection dosimetry: anthropometric data representing size distributions of adult worker populations and software algorithms," *Physics in medicine & biology*, vol. 55, no. 13, pp. 3789–811, jul 2010.

[111] L. D. Clark, M. G. Stabin, M. J. Fernald, and A. B. Brill, "Changes in radiation dose with variations in human anatomy: moderately and severely obese adults," *Journal of nuclear medicine : official publication, Society of Nuclear Medicine*, vol. 51, no. 6, pp. 929–32, jun 2010.

[112] A. R. Prideaux, H. Song, R. F. Hobbs, B. He, E. C. Frey, P. W. Ladenson, R. L. Wahl, and G. Sgouros, "Three-dimensional radiobiologic dosimetry: Application of radiobiologic modeling to patient-specific 3-dimensional imaging-based internal dosimetry," *Journal of Nuclear Medicine*, vol. 48, no. 6, pp. 1008–1016, 2007. [Online]. Available: http://jnm.snmjournals.org/cgi/doi/10.2967/jnumed.106.038000

[113] S. Chiavassa, M. Bardiès, F. Guiraud-Vitaux, D. Bruel, J.-R. Jourdain, D. Franck, and I. Aubineau-Lanièce, "Oedipe: A personalized dosimetric tool associating voxel-based models with mcnpx," *Cancer Biotherapy and Radiopharmaceuticals*, vol. 20, no. 3, pp. 325–332, 2005, pMID: 15989479. [Online]. Available: https://doi.org/10.1089/cbr.2005.20.325

[114] H. Yoriyaz, M. G. Stabin, and A. dos Santos, "Monte Carlo MCNP-4B-based absorbed dose distribution estimates for patient-specific dosimetry," *Journal of nuclear medicine : official publication, Society of Nuclear Medicine*, vol. 42, no. 4, pp. 662–9, apr 2001. [Online]. Available: http://www.ncbi.nlm.nih.gov/pubmed/11337557

[115] S. Wilderman and Y. K. Dewaraja, "NIH Public Access," *IEEE Transactions on Nuclear Science*, vol. 54, no. 1, pp. 146–151, 2007.

[116] S. D. Kost, Y. K. Dewaraja, R. G. Abramson, and M. G. Stabin, "VIDA: A Voxel-Based Dosimetry Method for Targeted Radionuclide Therapy Using Geant4," *Cancer Biotherapy & Radiopharmaceuticals*, vol. 30, no. 1, pp. 16–26, 2015. [Online]. Available: http://online.liebertpub.com/doi/abs/10.1089/cbr.2014.1713

[117] A. V. Gil, M. A. C. Pérez, and L. A. T. Aroche, "MCID : Herramienta Dosimétrica personalizada para simular estudios voxelizados con MCNP5," 2013.

[118] F. Botta, A. Mairani, R. F. Hobbs, A. V. Gil, M. Pacilio, K. Parodi, M. Cremonesi, M. A. C. Pérez, A. D. Dia, M. Ferrari, F. Guerriero, G. Battistoni, G. Pedroli, G. Paganelli, L. A. T. Aroche, and G. Sgouros, "Use of the fluka monte carlo code for 3d patient-specific dosimetry on pet-ct and spect-ct images," *Physics in Medicine & Biology*, vol. 58, no. 22, p. 8099, 2013.

[119] L. T. Dillman, "EDISTR—A Computer Program to Obtain a Nuclear Decay Data Base for Radiation Dosimetry," 1980.

[120] E. Fermi, "Tentativo di una teoria dei raggi β," *Il Nuovo Cimento (1924-1942)*, vol. 11, no. 1, p. 1, Sep 2008. [Online]. Available: https://doi.org/10.1007/BF02959820

[121] M. Abramowitz, I. A. Stegun, and D. Miller, *Handbook of Mathematical Functions With Formulas, Graphs and Mathematical Tables (National Bureau of Standards Applied Mathematics Series No. 55)*, 1965, vol. 32, no. 1. [Online]. Available: http://appliedmechanics.asmedigitalcollection.asme.org/article.aspx?articleid=1396937

[122] M. Momennezhad, S. Nasseri, S. Zakavi, A. Parach, M. Ghorbani, and R. Asl, "A 3D Monte Carlo method for estimation of patient-specific internal organs absorbed dose for 99m-Tc-hynic-Tyr-3 -octreotide imaging," *World Journal of Nuclear Medicine*, vol. 15, no. 2, p. 114, 2016.

[123] J. Grimes and A. Celler, "Comparison of internal dose estimates obtained using organ-level, voxel S value, and Monte Carlo techniques," *Medical Physics*, vol. 41, no. 9, 2014.

[124] A. Yordanova, E. Eppard, S. Kürpig, R. A. Bundschuh, S. Schönberger, M. Gonzalez-Carmona, G. Feldmann, H. Ahmadzadehfar, and M. Essler, "Theranostics in nuclear medicine practice," *OncoTargets and Therapy*, vol. 10, pp. 4821–4828, 2017.